

AD-A080 178

AIR FORCE INST OF TECH WRIGHT-PATTERSON AFB OH SCH00--ETC F/G 20/9  
ANALYSIS OF ELECTRON DRIFT VELOCITIES IN MOLECULAR GAS-RARE GAS--ETC(U)

UNCLASSIFIED

DEC 79 R F WITTLER  
AFIT/0EP/PH/79D-13

NL

1 OF 2

AD  
A080178







AFIT/GEP/PH/79D-13

14

6

ANALYSIS OF ELECTRON DRIFT VELOCITIES  
IN MOLECULAR GAS-RARE GAS MIXTURES  
USING A FLOWING AFTERGLOW PLASMA.

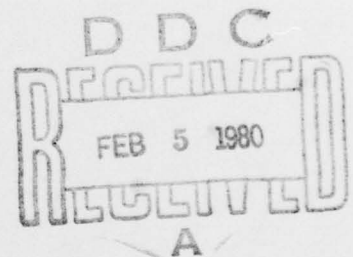
9

Master's THESIS,

AFIT/GEP/PH/79D-13

10

Richard F. Wittler  
Capt USAF



11 Dec 79

12 118

Approved for Public Release; Distribution Unlimited.

012 225

mt

ANALYSIS OF ELECTRON DRIFT VELOCITIES  
IN MOLECULAR GAS-RARE GAS MIXTURES  
USING A FLOWING AFTERGLOW PLASMA

THESIS

Presented to the Faculty of the School of Engineering ✓  
of the Air Force Institute of Technology  
Air Training Command  
in Partial Fulfillment of the  
Requirements for the Degree of  
Master of Science

by

Richard F. Wittler, B.A.  
Capt USAF  
Graduate Engineering Physics  
December 1979

|                    |  |
|--------------------|--|
| Accession For      |  |
| NTIS GRA&I         | <input checked="checked" type="checkbox"/> |
| DDC TAB            | <input type="checkbox"/>                   |
| Unannounced        | <input type="checkbox"/>                   |
| Justification      |  |
| By                 |  |
| Date               |  |
| Availability Codes |  |
| Dist               | Avail and/or<br>Special                    |
| A                  |  |

## Preface

The molecular gas-rare gas mixture is of particular interest, not only because this mixture is used extensively as a gas discharge lasing medium, but also because it displays an interesting phenomenon known as differential negative conductivity.

A theoretical development of the drift velocity in this type of mixture has been previously proposed by a numerical solution to the Boltzmann transport equation by Long, Bailey and Garscadden (Ref 1). This thesis provides the experimental data to confirm the theory in a flowing afterglow. Although drift velocity measurements in a flowing afterglow are much more difficult to analyze than they would be if a drift tube of more recent design had been used (for example, Crompton (Ref 2)), this gave a better insight into the physics and diagnostics of plasmas. In addition, a time-of-flight drift tube has been designed and presented.

A special note of thanks is in order for the staff of the Wright Aeronautical Laboratory, Plasma Physics Branch, where this thesis was completed. In particular, I want to thank Mr. Cliff VanSickle for his assistance in designing the drift tube, Mr. Jimmy Ray for repairing and modifying the flow tube as fast as I could break it, and Dr. Vivian Merchant for help and guidance in setting up the experimental

apparatus. A special note of thanks and gratitude is owed to Dr. Merrill Andrews of Wright State University, Dr. Alan Garscadden, my on-site laboratory advisor, of the Wright Aeronautical Laboratory, and Major Michael Stamm, my thesis advisor. Without the cooperation, guidance, and understanding of these three outstanding physicists, this thesis would surely be lacking in many ways. Finally, I want to thank Ms. Sharon Gabriel for doing an outstanding job of typing both the grading copy and final copy of this thesis.

Richard F. Wittler



### Dedication

This thesis is dedicated to my mother and father,  
who have taught me that nothing of value is ever achieved  
without hard work and perseverance.

## Contents

|  | Page |
|--|------|
| Preface.....   | ii   |
| Dedication.....  | iv   |
| List of Figures.....   | vii  |
| Abstract.....  | x    |
| I. Introduction.....   | 1    |
| II. Theory.....  | 6    |
| Drift Velocity and Elastic and Inelastic<br>Collisions.....                    | 8    |
| The Boltzmann Equation.....  | 13   |
| Drift Velocity vs Electric Field in the<br>Rare Gas-Molecular Gas Mixture..... | 15   |
| Concluding Remarks for Chapter II.....   | 29   |
| III. The Experiment.....   | 30   |
| Equipment Setup.....   | 30   |
| Experimental Parameters.....   | 35   |
| Electron Density.....  | 35   |
| Pressure.....  | 37   |
| Flow Rate.....   | 39   |
| Filament Current.....  | 39   |
| Vacuum System.....   | 39   |
| Procedure.....   | 40   |
| IV. Electron Density Measurement.....  | 41   |
| Electron Loss Curves.....  | 41   |
| Alternate Method.....  | 44   |
| Experimental Technique.....  | 45   |
| V. Results and Recommendations.....  | 47   |
| Results.....   | 47   |
| General.....   | 47   |
| Argon-Nitrogen Mixtures.....   | 49   |
| Argon-Carbon Monoxide Mixtures.....  | 58   |
| Helium-Nitrogen Mixtures.....  | 65   |
| Recommendations.....   | 74   |

## Contents (Cont'd)

|                              | Page |
|------------------------------|------|
| VI. Drift Tube Design.....   | 76   |
| Introduction.....            | 76   |
| Drift Tube Concept.....      | 77   |
| Drift Tube Design.....       | 80   |
| Drift Region.....            | 80   |
| Detection System.....        | 83   |
| Vacuum System.....           | 84   |
| Alignment of Electrodes..... | 84   |
| Recommendations.....         | 85   |
| Bibliography.....            | 87   |
| Appendix A.....              | 89   |
| Appendix B.....              | 94   |
| Appendix C.....              | 96   |
| Appendix D.....              | 97   |
| Appendix E.....              | 99   |
| Appendix F.....              | 101  |
| Vita.....                    | 104  |

## List of Figures

| <u>Figure</u> |  | <u>Page</u> |
|---------------|--|-------------|
| 1             | Increase in Drift Velocity and Appearance of Local Maximum in Various Ar-Co Mixtures.....  | 2           |
| 2             | Mixtures of N <sub>2</sub> in Ar Showing an Increase in Drift Velocity and the Region of Differential Negative Conductivity..... | 7           |
| 3             | Elastic Scattering of Electrons by an Argon Atom.....  | 10          |
| 4             | Drift Velocity and Energy vs Time for Elastic and Inelastic Collisions.....  | 11          |
| 5             | Momentum Transfer Cross Sections for Ar and N <sub>2</sub> , and Inelastic Cross Sections for N <sub>2</sub> .....               | 16          |
| 6             | The Effect of the Two Collision Frequencies on Drift Velocity.....   | 18          |
| 7             | Effect of Increasing the Percent of N <sub>2</sub> in an Ar Diluent.....   | 20          |
| 8             | The Effect of Cross Section Profiles on Differential Negative Conductivity in Electron Drift Velocity Curves.....                | 23          |
| 9             | W vs E/N for Mixtures of N <sub>2</sub> in Ar.....   | 24          |
| 10            | W vs E/N for Mixtures of Co in Ar.....   | 25          |
| 11            | W vs E/N for Mixtures of N <sub>2</sub> in He.....   | 26          |
| 12            | Cross Sections for Momentum Transfer Between Electrons on Neutral Atoms.....   | 27          |
| 12a           | Inelastic Cross Sections for Carbon Monoxide..   | 28          |
| 13            | Experimental Setup.....  | 32          |
| 14            | Diagnostics for Current-Voltage Readings.....  | 35          |
| 15            | Electron and Ion Densities Within the Plasma Sheath.....   | 36          |
| 16            | Experimental Procedure for Obtaining Current vs Distance Curves.....   | 43          |



# List of Figures (Cont'd)

| <u>Figure</u> |  | <u>Page</u> |
|---------------|--|-------------|
| 17            | Experimental Results for Electron Drift Velocities in Ar with 0%, 1%, 5%, 10% and 20% Added N <sub>2</sub> ..... | 51          |
| 18            | Electron Drift Velocity in Ar with 0% N <sub>2</sub> Added. Comparison of Theory with Experiment.                | 52          |
| 19            | Electron Drift Velocity in Ar with 1% N <sub>2</sub> Added. Comparison of Theory with Experiment.                | 53          |
| 20            | Electron Drift Velocity in Ar with 5% N <sub>2</sub> Added. Comparison of Theory with Experiment.                | 54          |
| 21            | Electron drift Velocity in Ar with 10% N <sub>2</sub> Added. Comparison of Theory with Experiment.               | 55          |
| 22            | Electron Drift Velocity in Ar with 20% N <sub>2</sub> Added. Comparison of Theory with Experiment.               | 56          |
| 23            | Comparison of Experimental 0% Added N <sub>2</sub> in Ar with Theoretical 1% Added N <sub>2</sub> in Ar.....     | 57          |
| 24            | Experimental Results for Electron Drift Velocities in Ar with 0%, 1%, 5%, 10% and 20% Added CO.....              | 59          |
| 25            | Electron Drift Velocities in Ar with 0% CO Added. Comparison of Theory with Experiment.                          | 60          |
| 26            | Electron Drift Velocities in Ar with 1% CO Added. Comparison of Theory with Experiment.                          | 61          |
| 27            | Electron Drift Velocities in Ar with 5% CO Added. Comparison of Theory with Experiment.                          | 62          |
| 28            | Electron Drift Velocities in Ar with 10% CO Added. Comparison of Theory with Experiment.                         | 63          |
| 29            | Electron Drift Velocities in Ar with 20% CO Added. Comparison of Theory with Experiment.                         | 64          |
| 30            | Experimental Results for Electron Drift Velocities in He with 0%, 1%, 5%, 10% and 20% N <sub>2</sub> Added.....  | 66          |
| 31            | Electron Drift Velocities in He with 0% N <sub>2</sub> Added. Comparison of Theory with Experiment.              | 67          |

List of Figures (Cont'd)

| <u>Figure</u> |  | <u>Page</u> |
|---------------|--|-------------|
| 32            | Electron Drift Velocities in He with 1% N <sub>2</sub> Added. Comparison of Theory with Experiment.  | 68          |
| 33            | Electron Drift Velocities in He with 5% N <sub>2</sub> Added. Comparison of Theory with Experiment.  | 69          |
| 34            | Electron Drift Velocities in He with 10% N <sub>2</sub> Added. Comparison of Theory with Experiment. | 70          |
| 35            | Electron Drift Velocities in He with 20% N <sub>2</sub> Added. Comparison of Theory with Experiment. | 71          |
| 36            | Current-Voltage Curves for He-N <sub>2</sub> Mixtures Where Helium Was the Gas Excited.....          | 72          |
| 37            | Light from a UV Laser Produces an Electron Swarm at a Photocathode.....                              | 78          |
| 38            | Drift Tube Diagnostics.....  | 79          |
| 39            | Conceptual Sketch of Drift Tube.....   | 81          |
| 40            | Alignment of Laser Over Center of End Flange.  | 85          |
| 41            | Alignment of Anode and Cathode.....  | 86          |
| A-1           | Microwave Resonant Cavity.....   | 90          |
| A-2           | Resonant Cavity Diagnostics.....   | 90          |
| B-1           | Flow Tube Dimensions.....  | 95          |
| C-1           | Drift Tube Design.....   | 96          |
| D-1           | Guard Ring Geometry for Drift Region.....  | 97          |
| F-1           | Electron Loss Curves for Argon.....  | 102         |

Abstract

Electron drift velocities are obtained in mixtures of Ar-N<sub>2</sub>, Ar-CO, and He-N<sub>2</sub> using a flowing afterglow. Theoretical development of drift velocities in the molecular gas-rare gas mixture is discussed. Two factors are discussed which determine the electron collision frequency: 1. The shape and magnitude of the electron elastic cross section of the buffer gas; and 2. The threshold energy and magnitude of the inelastic processes. Drift velocity enhancement and differential negative conductivity caused by the presence of small amounts of molecular gas are discussed. Experimental drift velocity curves show good agreement with theoretical curves obtained by a numerical solution to the Boltzmann equation. Minor deviations indicate that metastable ionization should be included in the computer analog to better model electron density in the flowing afterglow. A drift tube design using up-to-date electronics is proposed.

Analysis of Electron Drift Velocities  
in Molecular Gas-Rare Gas Mixtures  
Using a Flowing Afterglow Plasma

I. Introduction

The drift velocity of electrons in gases has been studied extensively over the past fifty years by Nielson and Bradbury (Ref 2), and more recently by Crompton (Refs 2, 3, 4) and Nagy (Refs 5, 6), using the time-of-flight technique. Drift velocity is a relatively easy parameter to measure experimentally and is useful in determining other transport parameters such as mobility, diffusion coefficients, cross sections, and a host of others (Refs 7, 8, 9, 10).

In particular, molecular gas-rare gas mixtures have become of prime interest because of their extensive use in high power gas discharge lasers. Since these lasing mixtures are "pumped" to their excited state, a knowledge of the energy characteristics of the gas mixture is desirable as well as for practical considerations such as discharge stability.

An interesting phenomenon occurs in the drift velocity when small amounts of a molecular gas are added to a rare gas. The electron drift velocity increases dramatically and there appears a local maximum when Argon, Krypton, or Xenon are used as the diluent (see Fig. 1).



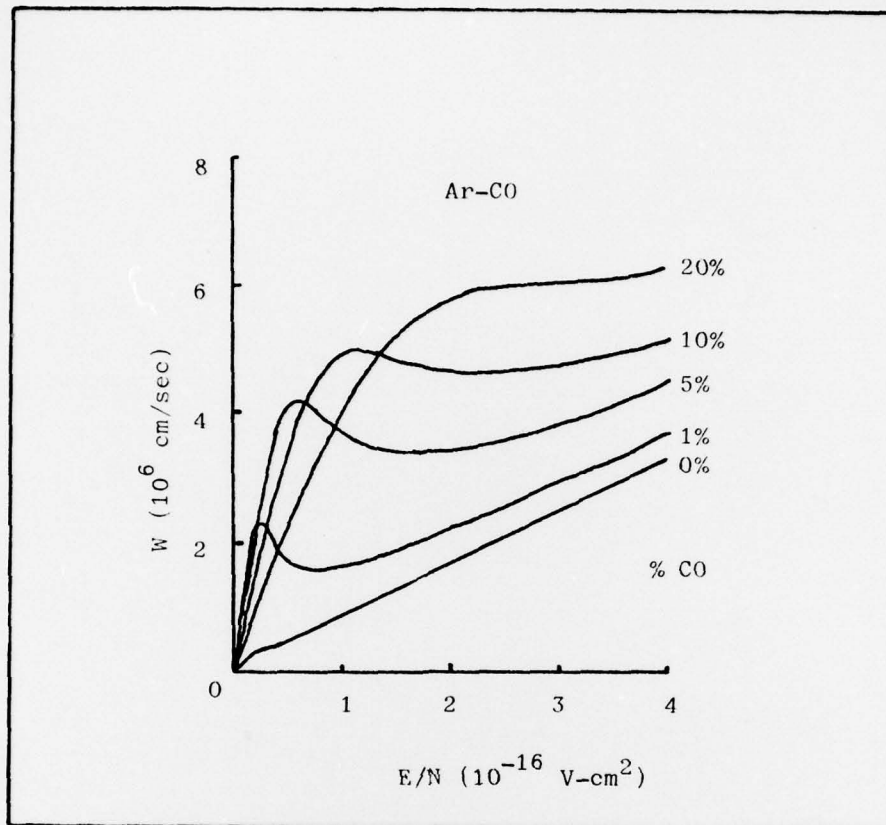


Figure 1. Increase in Drift Velocity and Appearance of Local Maximum in Various Ar-CO Mixtures. (Ref 1)

This local maximum presents a region of differential negative conductivity; that is, an increase in E/N (ratio of electric field to neutral number density) causes a decrease in current output.

A numerical solution to the Boltzmann transport equation has been published by Long, Bailey, and Garscadden (Ref 1) which predicts the existence of differential

negative conductivity for mixtures in which argon is the diluent. However, experimental data to support the theory are lacking for the flowing afterglow. This paper attempts to tie together the theory with experimental results in a flowing afterglow.

In this experiment an axial flow discharge tube was used and drift velocity measured by two planar probe electrodes in the flow stream by applying a voltage across the electrodes and measuring the resultant current. The current is then converted to drift velocity by the equation

$$i = e n_e A W , \quad (1)$$

where

- $i$  = measured current (amperes)
- $e$  = elementary charge (Coulombs)
- $n_e$  = electron number density ( $\text{cm}^{-3}$ )
- $A$  = area of the electrode ( $\text{cm}^2$ )
- $W$  = drift velocity (cm/sec)

To measure the absolute drift velocity, a procedure for determining the electron loss as a function of distance from the electrodes was developed. Current-voltage characteristics were recorded, then converted to  $W$  vs  $E/N$  plots similar to that of Fig. 1. These curves were then compared to theoretical drift velocity curves given

in Reference 1.

The decision to include material which at first seemed excessive was made with the idea in mind that a student of physics with only a casual knowledge of the subject material could become familiar with the theory, techniques, and problems of a flowing afterglow experiment without having to consult numerous other published articles.

In Chapter II, the basic theory of drift velocity in the molecular gas-rare gas mixture is discussed. The Boltzmann transport equation is presented and calculated results given. Results from an analytical computer code, previously developed by the Plasma Physics Group of the Air Force Wright Aeronautical Laboratory, were used by permission of Dr. A. Garscadden.

The experimental portion of this paper is presented in Chapter III. The equipment setup is discussed and applicable parameters given.

The electron number density is of importance in any afterglow measurement; therefore, an entire section is devoted to this subject. Chapter IV develops an experimental technique to determine the electron number density without the need for electron loss equations or complex computer codes.

The results of the experiment and its comparison to theoretical data is discussed in Chapter V.

Chapter VI concludes the text by presenting a drift tube design that can be used for future drift velocity experiments.

There is an adherence to CGS units throughout this paper.



## II. Theory

### Introduction

Drift velocities in rare gas-molecular gas mixtures have been investigated since 1913. Many authors (Refs 1, 5, 6, 13, 14) have studied these gas mixtures; in particular, Ar with  $N_2$ ,  $CO_2$ , and  $H_2$ ). They have found that a small amount of a molecular gas, when added to the rare gas, produces a substantial increase in the electron drift velocity at low  $E/N$  (less than approximately  $10^{-16}$  V cm<sup>2</sup>). In gas mixtures where argon, xenon, and krypton are used as the rare gas diluent, a region of differential negative conductivity is observed (see Fig. 2). These phenomena can be explained by the addition of the inelastic cross sections of the molecular gas when added to the elastic (momentum transfer) cross section of the rare gas.

The Boltzmann transport equation has been solved numerically by Long, Bailey, and Garscadden (Ref 1) for the electron energy distribution function from which the electron drift velocity has been obtained. An analytical expression for the drift velocity was also developed by Long, et al. and showed excellent agreement with the numerical solution.

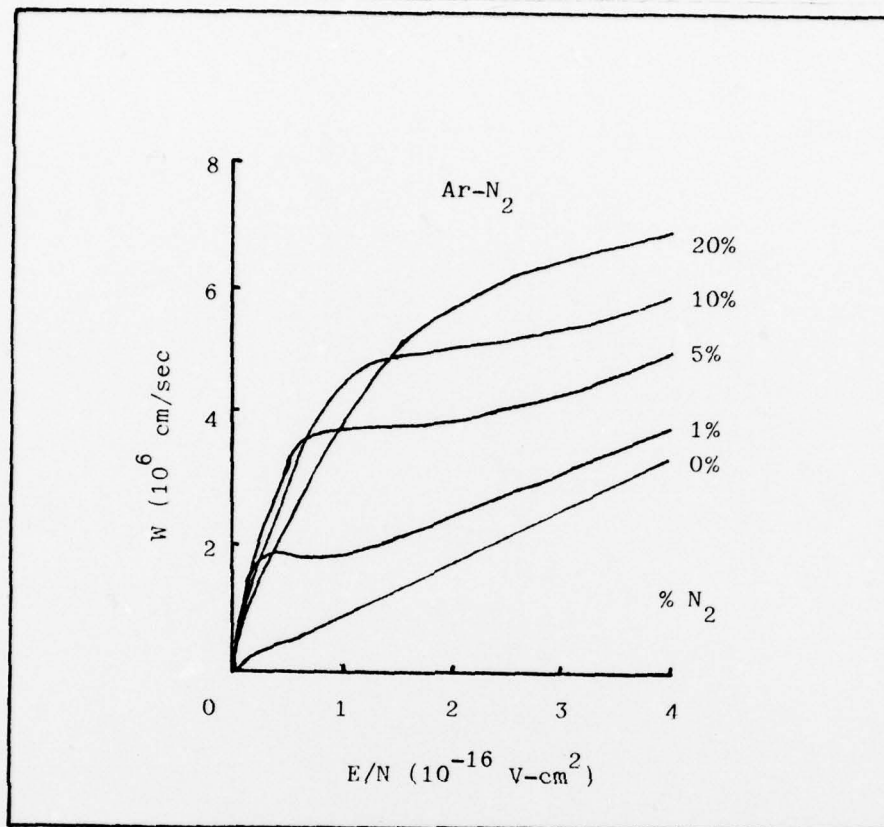


Figure 2. Mixtures of  $N_2$  in Ar Showing An Increase in Drift Velocity and the Region of Differential Negative Conductivity. (Ref 1)

A full derivation of the solution of the Boltzmann equation is beyond the purpose of this paper. The solution is presented to provide completeness and mathematical insight to the controlling processes that govern the drift velocity of electrons in the rare gas-molecular gas mixtures.

This section begins with a discussion of elastic and inelastic collisional processes and their effect on the electron drift velocity using a model that was developed by Stamm et al. (Ref 11). The solution to the Boltzmann transport equation is then presented, along with predicted results for the electron drift velocity. Finally, the controlling processes for the observed phenomena are discussed.

#### Drift Velocity and Elastic and Inelastic Collisions

There are two assumptions that are made in this analytical analysis of collisional processes: (1) elastic collisions completely randomize the electrons' direction; that is, they are scattered isotropically, and (2) an electron loses all of its energy in an inelastic collision.

To illustrate the effect of elastic and inelastic collisions on electron drift velocity, it is helpful to follow a "typical" packet of electrons as they move through a molecular gas-rare gas mixture; for example, argon and diatomic nitrogen. There is a uniform electric field in the x direction. Assume, for example, that the electrons make five elastic collisions before making an inelastic collision, and that the inelastic cross section of  $N_2$  is large.

Three terms are defined for clarity: (1) the velocity,  $v$ , is the vector velocity of an individual particle,

(2) the drift velocity,  $W$ , is the average of all of the particles' velocities, and (3) the speed,  $s$ , is the magnitude of the velocity  $v$ .

The electron packet is accelerated by the electric field and attains a drift velocity just before collision of

$$W = a t, \quad (2)$$

where  $a$  is the acceleration and  $t$  is the time between collisions, (point 1 on Fig. 4). The acceleration can be obtained from

$$F = ma = eE, \quad (3)$$

or

$$a = \frac{eE}{m}, \quad (4)$$

where  $E$  is the applied electric field. The time between collisions is the inverse of the collision frequency  $\nu$ ;

$$t = \frac{1}{\nu} = \frac{1}{n_a \sigma_{mt} s}, \quad (5)$$

where  $n_a$  is the neutral gas number density, and  $\sigma_{mt}$  is the electron impact cross section for momentum transfer.



Substitution of Equations (4) and (5) into Equation (2) gives

$$W = \frac{eE}{m} \left( \frac{1}{n_a \sigma_{mt} S} \right) \quad (6)$$

After the elastic collision, the electron packet is completely randomized and its drift velocity becomes zero since the scattering is assumed isotropic (see Fig. 3).

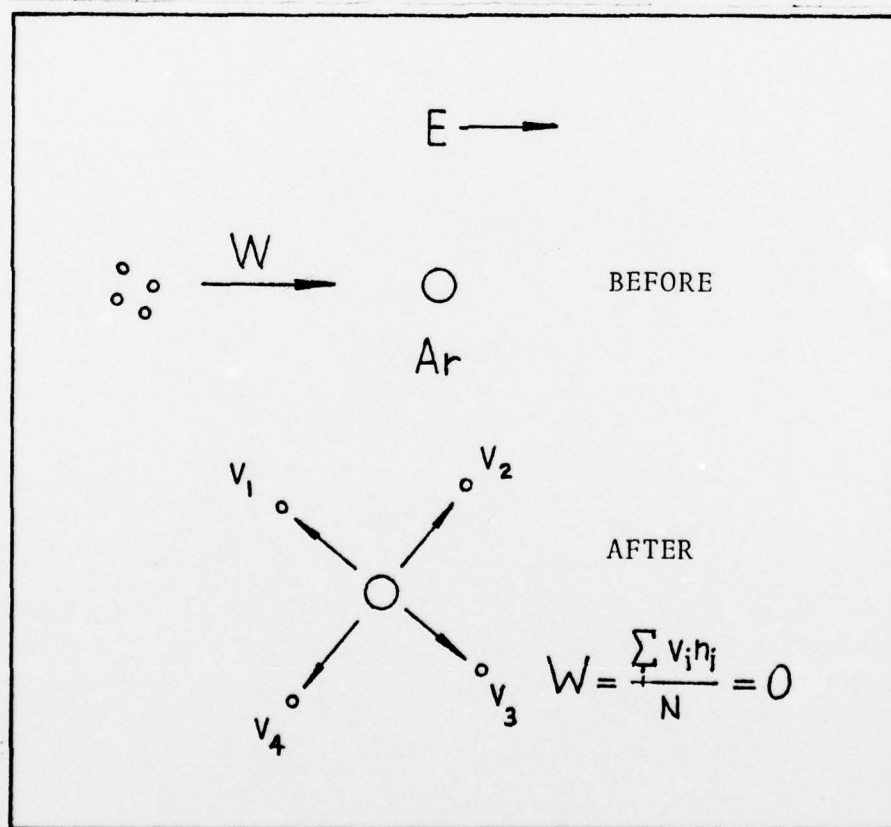


Figure 3. Elastic Scattering of Electrons by an Argon Atom.

The average speed of each electron continues to increase, however, as the electric field continues to accelerate the electrons (bottom graph of Fig. 4). The increase in average speed has the effect of decreasing the time between collisions (see Equation (5)), and hence the drift velocity between collisions (see Equation (6) and point 2 on Fig. 4).

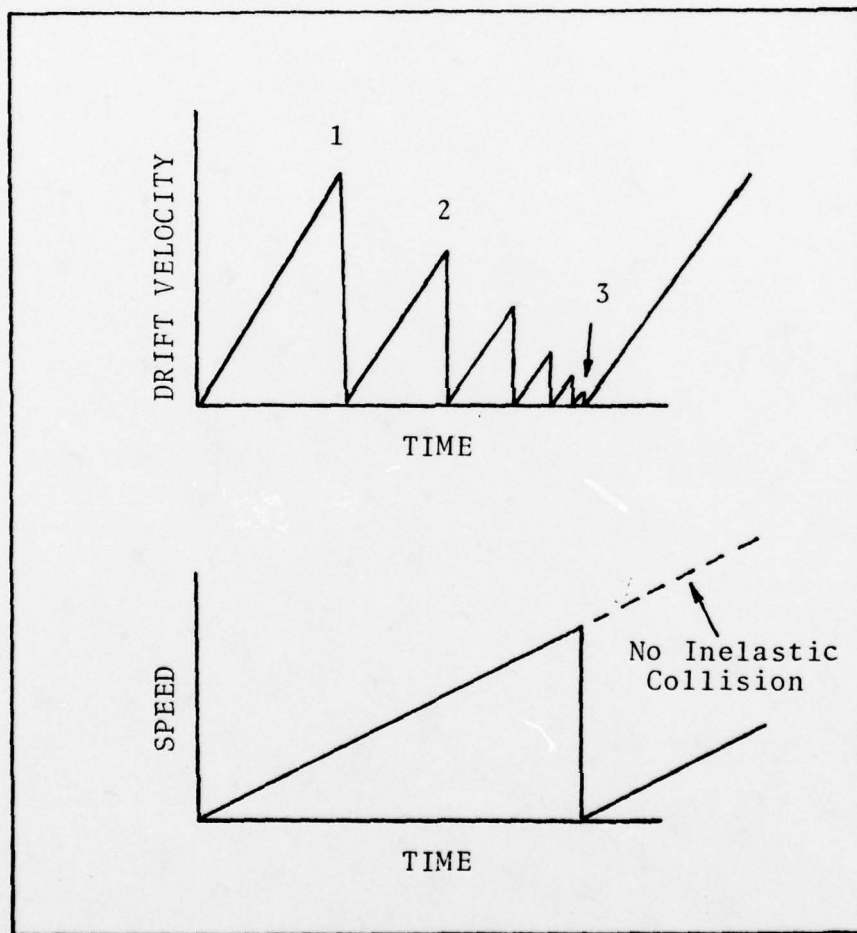


Figure 4. Drift Velocity and Energy vs Time  
For Elastic and Inelastic Collisions.  
(Ref 11)

This process continues until the packet encounters the inelastic cross section of nitrogen, after which the electrons have zero energy and zero velocity (point 3 on Fig. 4). This has the effect of starting the collision process all over again as illustrated in Fig. 4.

When this collision process is averaged over time, the electrons will establish an average collision frequency,  $\langle \nu \rangle$ , determined by the average speed,  $\bar{s}$ , attained between inelastic collisions. If the inelastic cross section was not present (dotted line in Fig. 4), the packet would attain a higher average speed and a lower drift velocity.

To make the expression for the drift velocity more general, note that the momentum transfer cross section is a function of electron energy, that is,  $\sigma_{mt} = \sigma_{mt}(\epsilon)$  and that there may be more than one elastic cross section:

$$W = \frac{eE}{m} \left( \frac{1}{\bar{s} \sum_a \sigma_{mt}(\epsilon)} \right) . \quad (7)$$

Equation (7) is by no means an exact expression for the electron drift velocity in a uniform electric field. It does, however, show in a simplified manner how the drift velocity depends on the electron impact cross sections, gas density, electron energy, and the applied electric field. To obtain the exact solution, one must solve the Boltzmann transport equation numerically.

### The Boltzmann Equation

This section presents the equation for the electron drift velocity derived from the solution to the Boltzmann transport equation. The equations presented here are those of Long et al. (Ref 1). The full derivation and solution can be found in Ref. 1. The solution is valid for electrons that undergo elastic and inelastic collisions with a cold gas.

To account for the angular distribution of electron velocities,  $f(v, \theta) = f_0(v) + f_1(v)\cos\theta$  was used as the electron velocity distribution function. The Boltzmann equation is then:

$$\begin{aligned} \frac{E/N}{3u} \frac{\partial}{\partial u} (uf_1) + \sum_h Q_h f_0 &= \frac{2}{u} \frac{m}{M} \frac{\partial}{\partial u} (u^2 Q_m f_0) \\ &+ \sum_h Q_h(u') f_0(u') \left(\frac{u'}{u}\right) \quad , \end{aligned} \quad (8)$$

where  $u' = u + \Delta u_h$  and  $\Delta u_h$  is the energy lost to the inelastic collision of cross section  $Q_h$ .  $Q_m$  is the sum of the momentum transfer cross sections (elastic cross sections).  $M$  is the proton mass and  $m$  is the electron mass. Also,



$$\frac{E}{N} \frac{\partial f_0}{\partial u} + (Q_r + \sum_h Q_h) f_1 = 0, \quad (9)$$

where  $Q_r$  is the sum of momentum transfer cross sections weighted by mole fraction. Integration of Equation (8) with respect to energy, substitution of Equation (9) into Equation (8) and further integration yields the expression for  $f_0(u)$ ;

$$f_0(u) = \exp \left[ \frac{-3}{(E/N)^2} \left( \frac{2m}{M} \int u Q_m Q_r du + \frac{Q_t}{u f_0} \int_u^{u'} Q_h f_0 u du^2 \right) \right], \quad (10)$$

where  $Q_t = Q_r + \sum Q_h$ . The value of  $f_0(u)$  is then obtained by numerical integration and  $f_1(u)$  by substitution of  $f_0(u)$  into Equation (9). The drift velocity is calculated using the expression

$$W = \frac{1}{3} \left( \frac{2e}{m} \right)^{1/2} \frac{\int_0^\infty f_1(u) du}{\int_0^\infty f_0(u) u^{1/2} du}. \quad (11)$$

An analytical expression for the drift velocity in gas mixtures has also been derived by Long et al. (Ref. 1),

$$W = \frac{eE}{m\langle v \rangle} , \quad (12)$$

where

$$\langle v \rangle = \left( \frac{2e}{m} \right)^{1/2} \sum_h F_h \left( \frac{E}{N} \right) \frac{N_a}{\Delta u_K} \int_{u_K - \Delta u_K}^{u_K} u^{1/2} Q_t du , \quad (13)$$

and  $F_h$  is the fraction of electrical power deposited in the  $h^{\text{th}}$  inelastic collision. This is the same form for  $W$  obtained previously in Equation (7). Although the more succinct form for  $\langle v \rangle$  is given by Equation (13), Equation (12) will suffice for the discussion of the controlling collisional processes.

#### Drift Velocity vs Electric Field in the Rare Gas-Molecular Gas Mixture

For ranges of  $E/N$  such that the average electron energy is less than or equal to the threshold energy for the inelastic cross section of the molecular gas, large changes in  $E/N$  make only small changes in the electron energy distribution function,  $f(\epsilon)$ . Thus, over those ranges  $f(\epsilon)$ , and hence  $\langle v \rangle$ , are only weak functions of  $E/N$ , so it is then proper to assume that  $\langle v \rangle$  is nearly constant over that range. If  $W = \left[ \frac{e}{m\langle v \rangle} \right] E$  is plotted as a function of  $E$ ,

a nearly straight line is obtained having a slope of  $\frac{e}{m\langle v \rangle}$ . Thus, the collision frequency determines the slope of the line. An example using an arbitrary mixture of argon and nitrogen will serve best here to explain drift velocities in the gas mixtures. Figure 5 shows the various cross sections of argon and diatomic nitrogen.

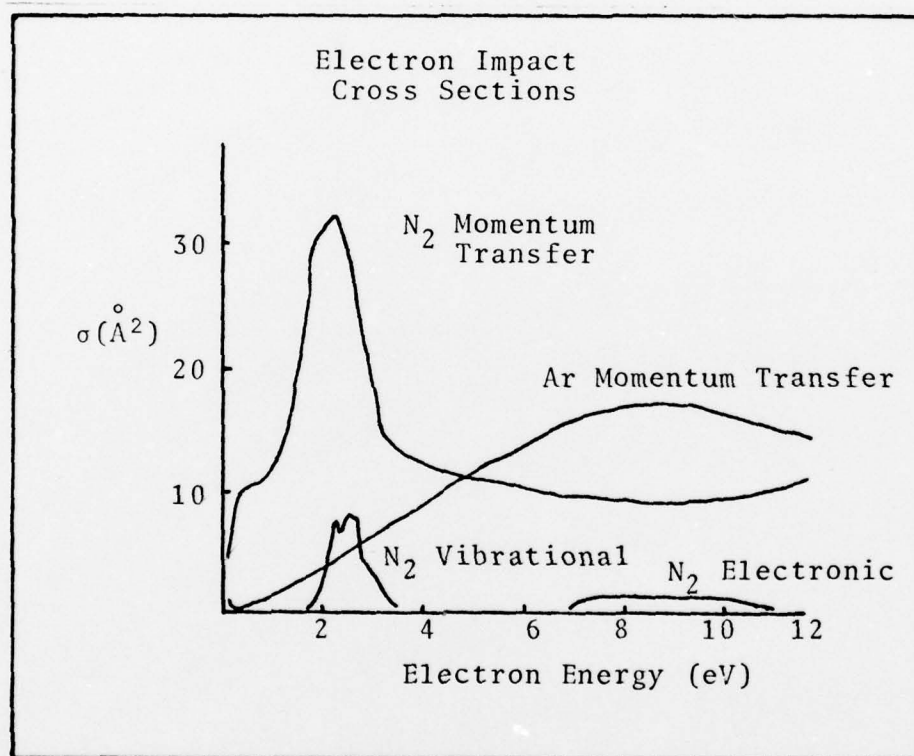


Figure 5. Momentum Transfer Cross Sections for Ar and N<sub>2</sub>, and Inelastic Cross Sections for N<sub>2</sub>. (Ref 15)

For the purpose of this illustration, an electron packet will be considered starting in an electric field of zero. At low  $E/N$ , the electron gains energy from the applied field and is considered not to lose energy due to elastic collisions with argon and nitrogen. As it reaches an energy of approximately 2 eV, some electrons begin to undergo inelastic collisions with  $N_2$ , causing vibrational excitation. Since the assumption is that the electron loses all of its energy in inelastic collisions, the electron energy is zero eV and begins the collisional process over again. An "average" collision frequency is established based on the few elastic collisions it makes prior to reaching the 2 eV vibrational inelastic collisional cross section. At high  $E/N$ , the electron gains energy at a faster rate and eventually reaches an energy greater than 3 eV prior to colliding with an  $N_2$  molecule. The vibrational cross section is zero past 4 eV, so the electron does not "see" this cross section and continues to gain energy until it reaches approximately 7 eV corresponding to the  $N_2$  electronic inelastic cross section. The electron loses all of its energy and must start the process over again, this time establishing a higher average collision frequency because it suffers many more elastic collisions on its way to reaching the 7 eV inelastic threshold.

The two collision frequencies established by the two inelastic cross sections correspond to the two slopes;



$$N_2 \text{ vibrational} = \frac{e}{m\langle v \rangle_v} ,$$

and

$$N_2 \text{ electronic} = \frac{e}{m\langle v \rangle_e} ,$$

where

$$\frac{e}{m\langle v \rangle_v} > \frac{e}{m\langle v \rangle_e} .$$

This is represented graphically in Fig. 6. The curved line connecting the two straight lines represents a transition from the lower to the higher energy inelastic collision frequency.

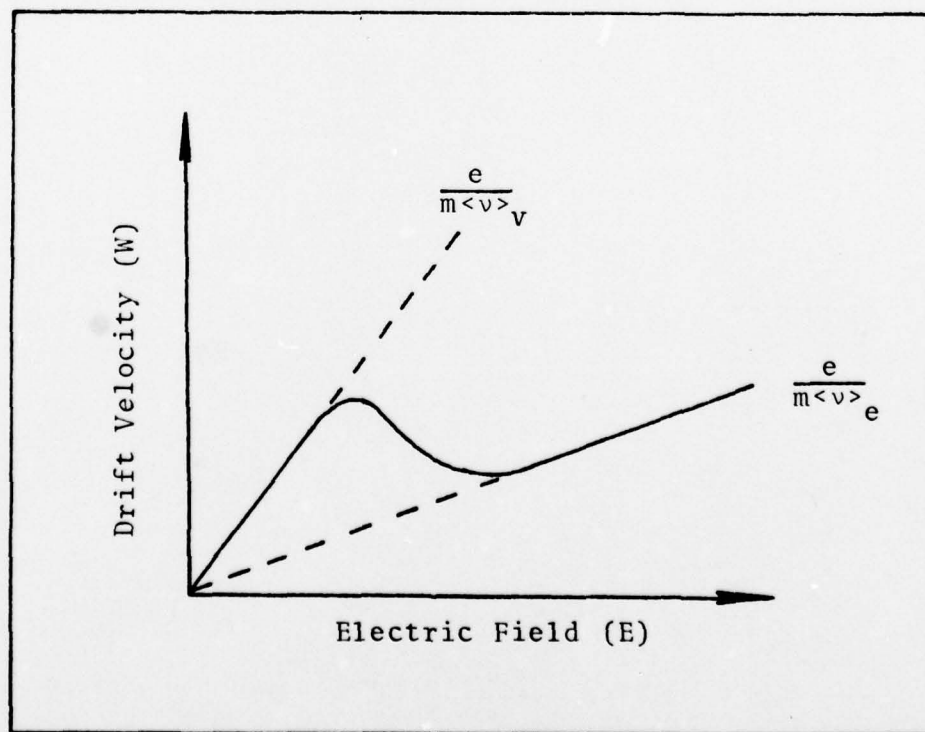


Figure 6. The Effect of the Two Collision Frequencies on Drift Velocity.



Note, now, that the transition between the two inelastic cross sections results in a decrease in the drift velocity. This is due to a significant increase in momentum transfer cross section of argon between the two inelastic cross sections. This establishes an increasing collision frequency as the electron energy is raised from 2 eV to 7 eV. This local maximum establishes an area of differential negative conductivity. That is, the greater the electric field, the fewer electrons that can be obtained per unit time (current). This essentially acts as an area of greater resistance, or negative conductance; hence the name, differential negative conductivity.

As the percent of nitrogen in the mixture is increased, the slopes of the two drift velocity lines change. The large momentum transfer cross section of  $N_2$  begins to dominate over the smaller momentum transfer cross section of argon. The effect is to increase the collision frequency at low electron energies and maintain a near constant collision frequency between 2 eV and 7 eV. This effect is graphically shown in Fig. 7.

There are two factors that determine the presence and prominence of differential negative conductivity: (1) the definition (sharpness) of the inelastic cross sections, and (2) the profile of the total momentum transfer cross section. Although both of these mechanisms

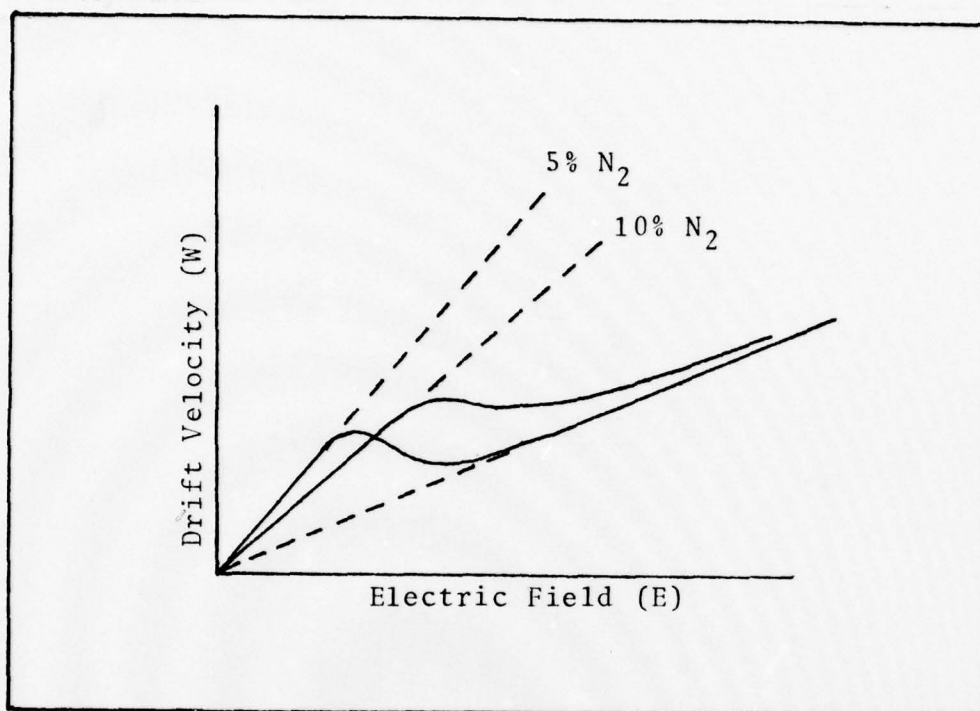


Figure 7. Effect of Increasing the Percent of N<sub>2</sub> in an Ar Diluent.

affect differential negative conductivity in different ways, they both have the effect of modifying the collision frequency of the electrons. When the inelastic cross sections are sharp, well-defined high peaks, as in the Ar-CO mixture (see top graph in Fig. 8), the collision frequency will change abruptly when the electrons are accelerated beyond the first inelastic threshold. When the cross sections are broad and ill-defined, the transition is more gradual as in the Ar-N<sub>2</sub> mixture (middle graph in

Fig. 8). The total momentum transfer cross section profile is the primary cross section that establishes the collision frequencies. When it increases rapidly with electron energy, the slopes of the two lines corresponding to the two collision frequencies are well separated.

As a limiting case, when the momentum transfer cross section decreases as  $\epsilon^{-1/2}$ , then there will be no line separation. That is,  $\sigma_{mt} = \sigma_{mt_0} \epsilon^{-1/2}$ , and  $\bar{s} = \sqrt{\frac{2}{m}} \epsilon^{1/2}$  so Equation (7) can be written as

$$W = \frac{eE}{m} \left[ \frac{1}{\sqrt{\frac{2}{m}} \sigma_{mt_0}} \right], \quad (14)$$

or

$$W = \left[ \frac{e}{\sqrt{2m} \sigma_{mt_0}} \right] E, \quad (15)$$

and one straight line will be obtained as in the bottom graph in Fig. 8.

The magnitude of the two effects will determine if the collision frequency will increase or decrease between the two inelastic cross sections and, hence, will determine if differential negative conductivity will be displayed. Figure 8 illustrates the extremes of these two effects.

The foregoing discussion is somewhat simplified, but it does illustrate the controlling processes in the gas mixture. The theoretical drift velocity curves for Ar-N<sub>2</sub>, Ar-CO, and He-N<sub>2</sub> mixtures (Ref 1), are presented in Figs. 9 through 11.

Observe in the He-N<sub>2</sub> mixture (Fig. 11) that it does not display differential negative conductivity. This is due to the nearly constant (actually slightly decreasing) momentum transfer cross section of He between the two inelastic cross sections of N<sub>2</sub>. This causes a slight decrease in collision frequency and the drift velocity continues to increase between the two inelastic collisional energies. In general, then, differential negative conductivity can be expected when there is an increase in total momentum transfer cross section between two separate inelastic cross sections. Figure 12 shows the momentum transfer cross sections of the rare gases, along with the cross sections of nitrogen and carbon monoxide. Figure 12a shows the inelastic cross sections for carbon monoxide. From this discussion, it is reasonable to expect that argon, krypton, and xenon will display differential negative conductivity with N<sub>2</sub> or CO, whereas helium and neon will not.



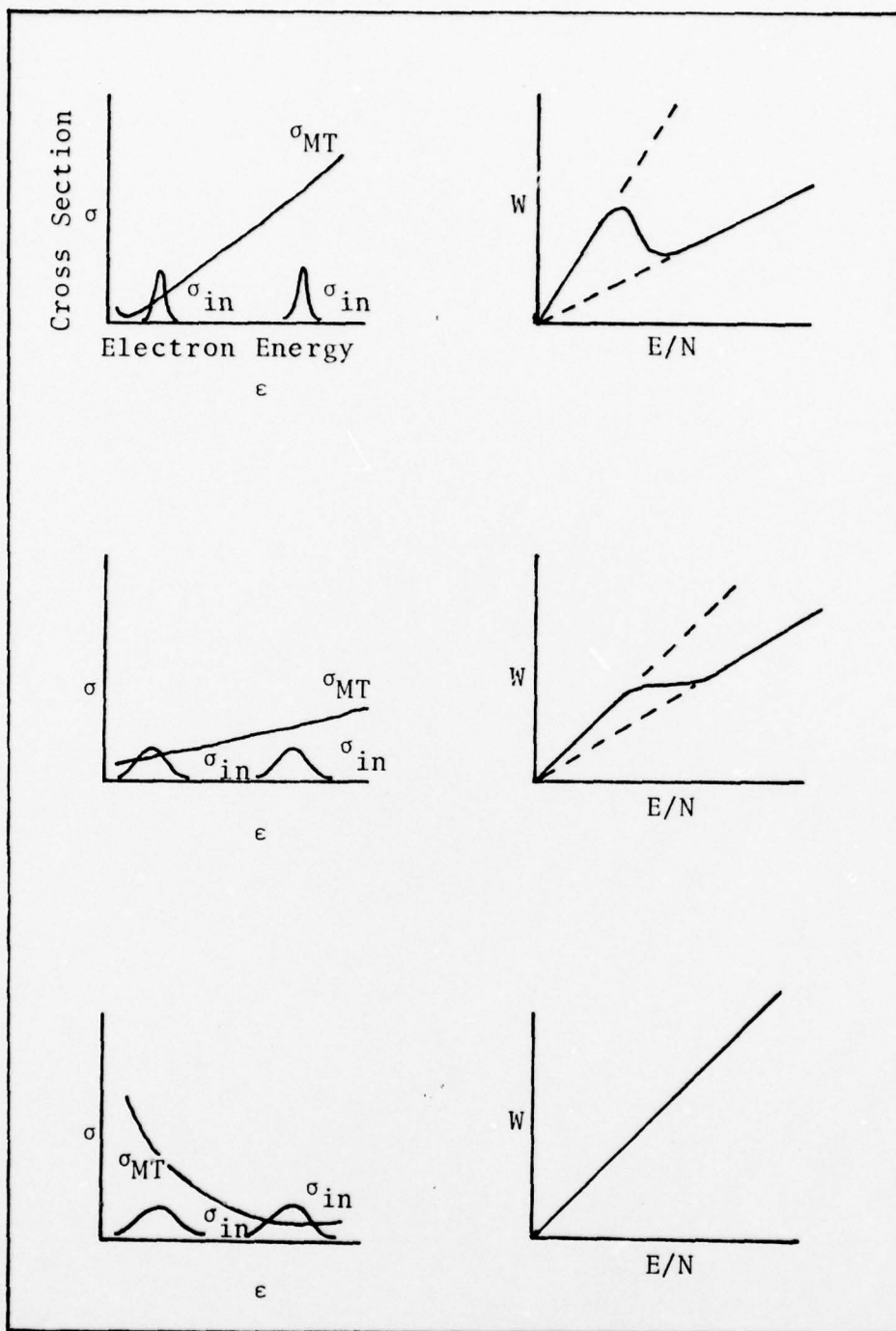


Figure 8. The Effect of Cross Section Profiles on Differential Negative Conductivity in Electron Drift Velocity Curves.

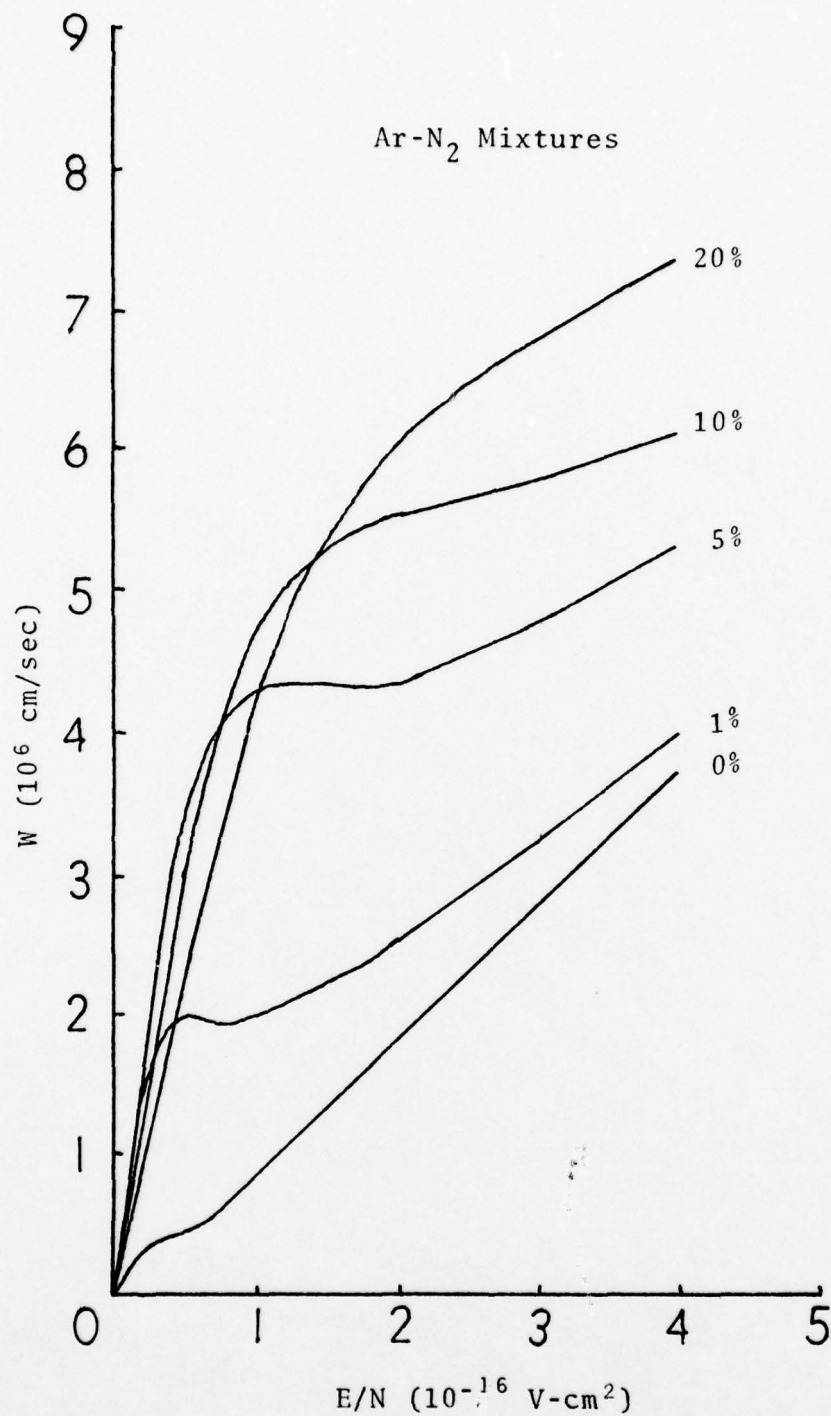


Figure 9. W vs E/N for Mixtures of 0%, 1%, 5%, 10%, and 20% N<sub>2</sub> in Ar, Derived From the Numerical Solution to the Boltzmann Equation (Ref 1).

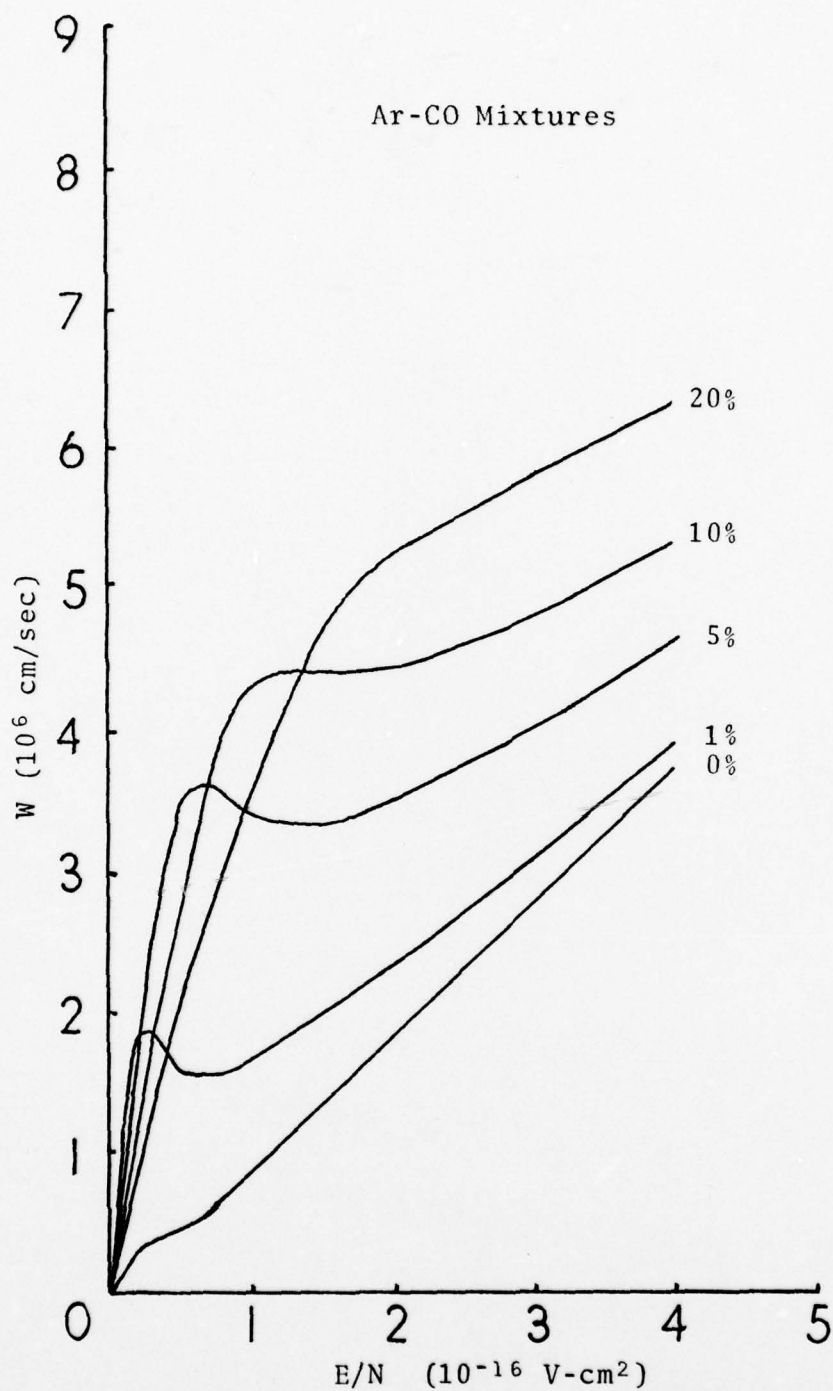


Figure 10.  $W$  vs  $E/N$  for Mixtures of 0%, 1%, 5%, 10%, and 20% CO in Ar, Obtained From the Numerical Solution to the Boltzmann Equation (Ref 1).

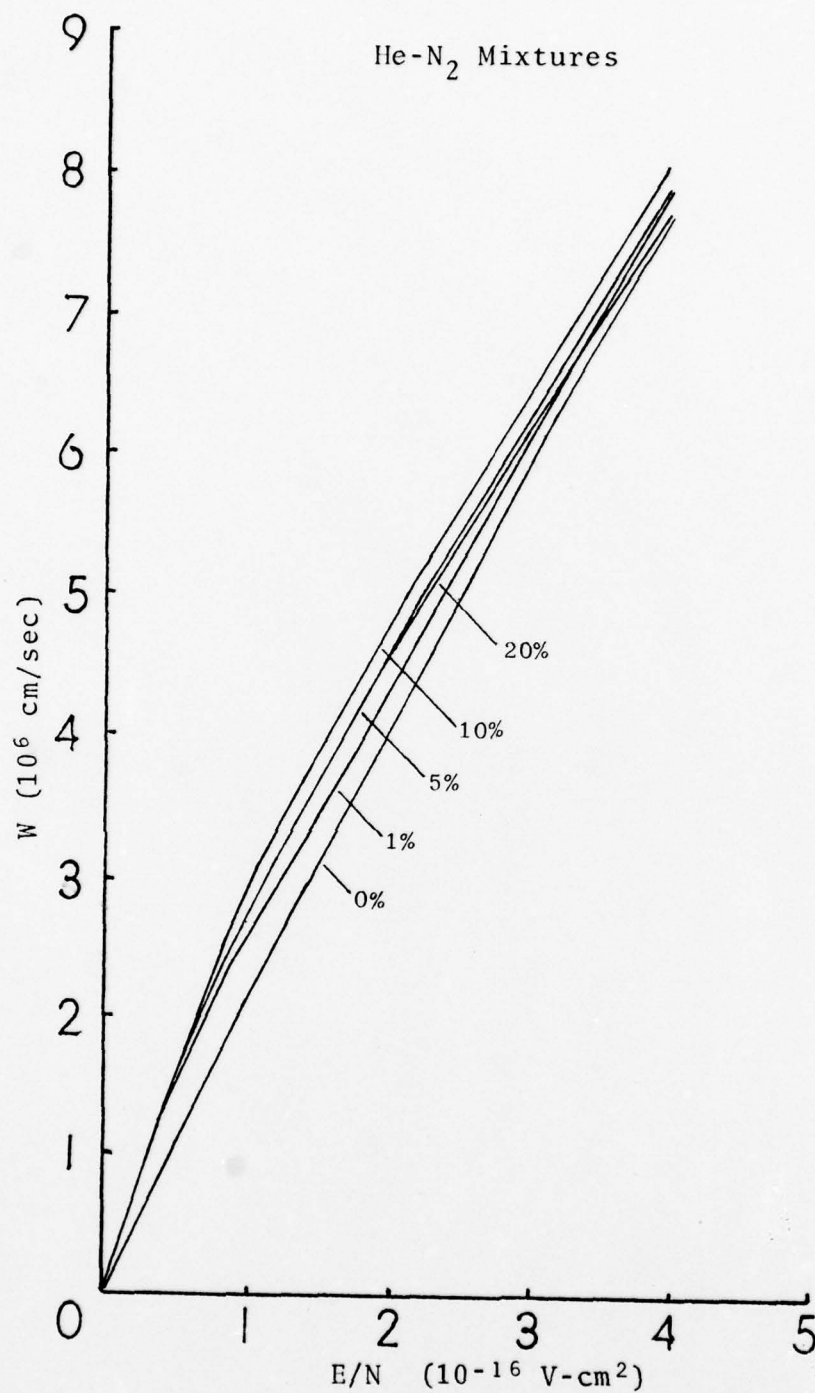


Figure 11. W vs E/N for Mixtures of 0%, 1%, 5%, 10%, and 20% N<sub>2</sub> in He Obtained From the Numerical Solution to the Boltzmann Equation (Ref 16).



MOMENTUM TRANSFER  
CROSS SECTIONS

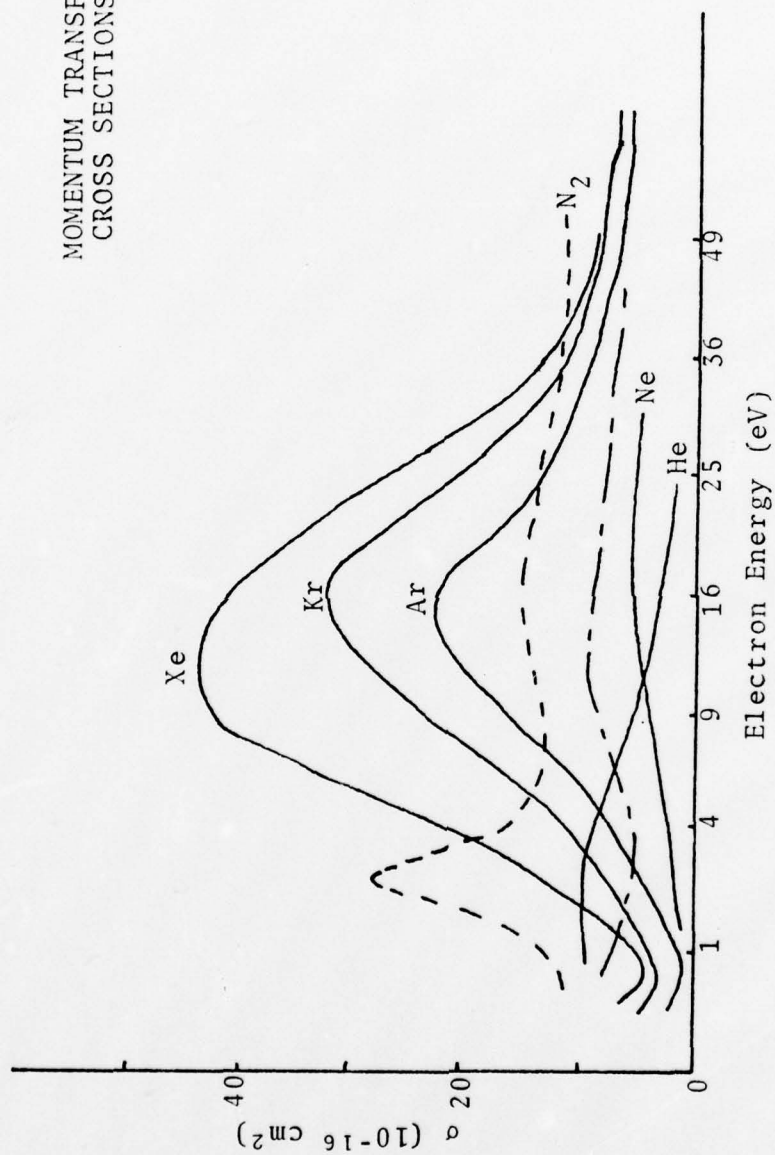


Figure 12. Cross Sections for Momentum Transfer  
Between Electrons and Neutral Atoms  
(Ref 17)

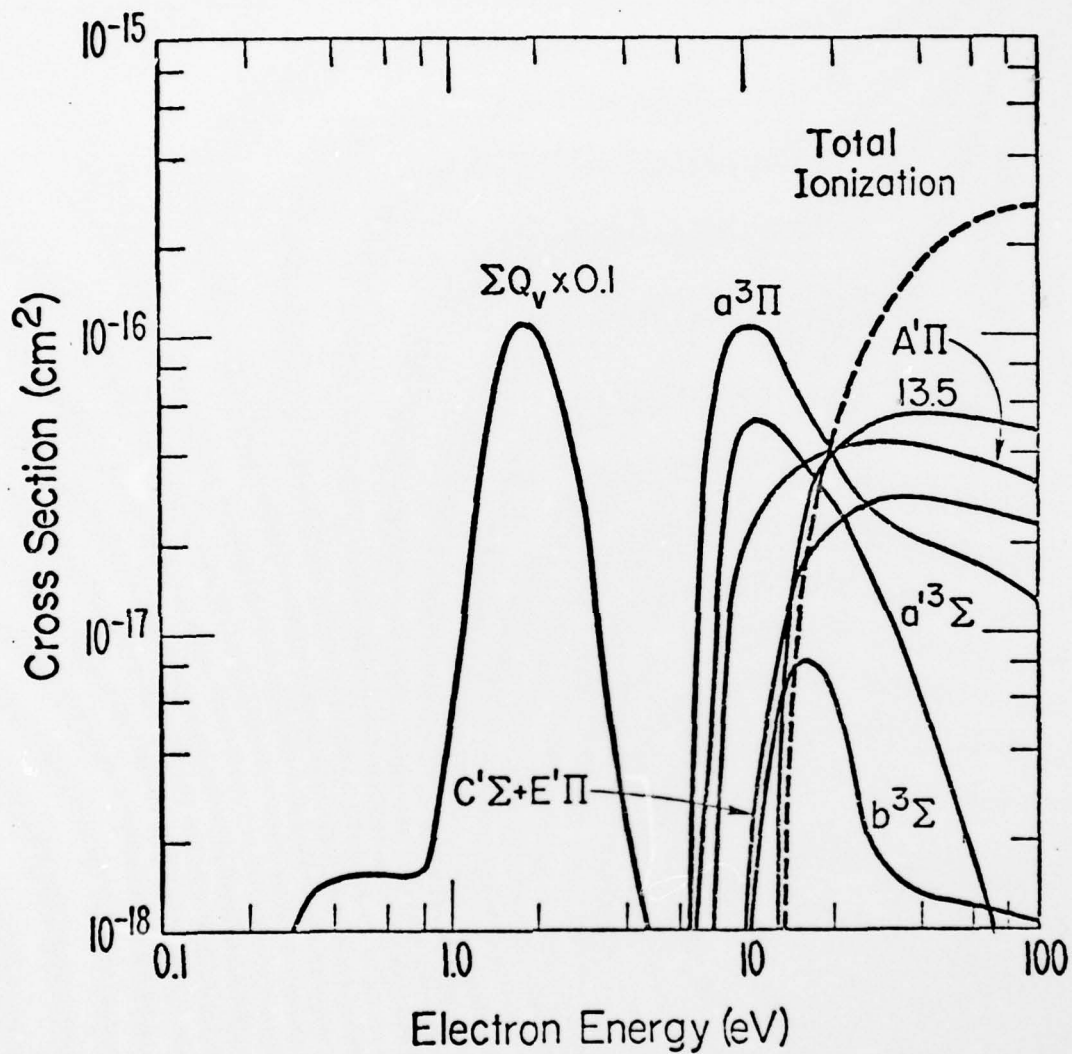


Figure 12a. Inelastic Cross Sections  
for Carbon Monoxide.  
(Ref 31)

## Concluding Remarks for Chapter II

This chapter in no way intended to present mathematical rigor for drift velocity prediction curves. Its main purpose was to give insight into the processes that give rise to the observed phenomena in these types of gas mixtures so that experimental data can be understood. The reader is referred to Refs 18 and 19 for a more extensive mathematical derivation to the solution of the Boltzmann equation.

### III. The Experiment

Drift velocity measurements in the past have been done by many authors using the time-of-flight technique (Refs 2, 4, 5, 6, 14, and 20). Only a few authors could be found who used a flowing afterglow to determine transport data (Refs 12 and 21). This is probably due to complicated probe effects that must be considered with an active plasma. Since most high power lasers use a flowing gas discharge as a lasing medium, the flowing afterglow provides an excellent simulation of transport phenomena within the larger gas dynamic lasers.

To measure the drift velocity in this way, the gas is ionized by microwaves. Two electrodes downstream are used to measure a current when a potential is applied to them. This current can be directly converted to drift velocity by

$$i = e n_e A W \quad , \quad (16)$$

where the terms have been previously defined. This assumes that the electron current is measured in a uniform electric field.

#### Equipment Setup

The flow tube system is conceptually illustrated in



Fig. 13. The rare gas is fed into the end of the quartz flow tube through a micrometer valve and flow meters to control and monitor the flow rate. Two flow meters were used in series (0-100 SCCM and 0-500 SCCM) to add accuracy and flexibility to the flow rates. An Evenston-type microwave cavity coupled with a 2.45 GHz microwave generator creates the electron density inside the flow tube by ionizing the rare gas. The microwave resonant cavity is used to measure the initial electron density. The plasma flows past two plane parallel plate electrode probes by which the diagnostic measurements are made. The vacuum in the tube is maintained by a Leybold forepump and pressure is controlled by the pressure control valve located between the end of the flow tube and the vacuum pump. The pressure is monitored by a Wallace-Tiernan, absolute pressure, aneroid pressure gauge (.1 to 20 Torr), and a thermocouple (atmospheric to 1 micron).

The molecular gas is controlled and monitored in the same manner as the rare gas, but is fed into the plasma by a hollow pyrex probe 10 cm before the electrodes. This accomplishes two things. First, it gives a constant excitation and allows the use of one electron decay profile for all of the gas mixture ratios (see Chapter IV for electron decay), since addition of a molecular gas to a rare gas alters the electron loss rates (Refs 1, 2). Second, it prevents the buildup of carbon

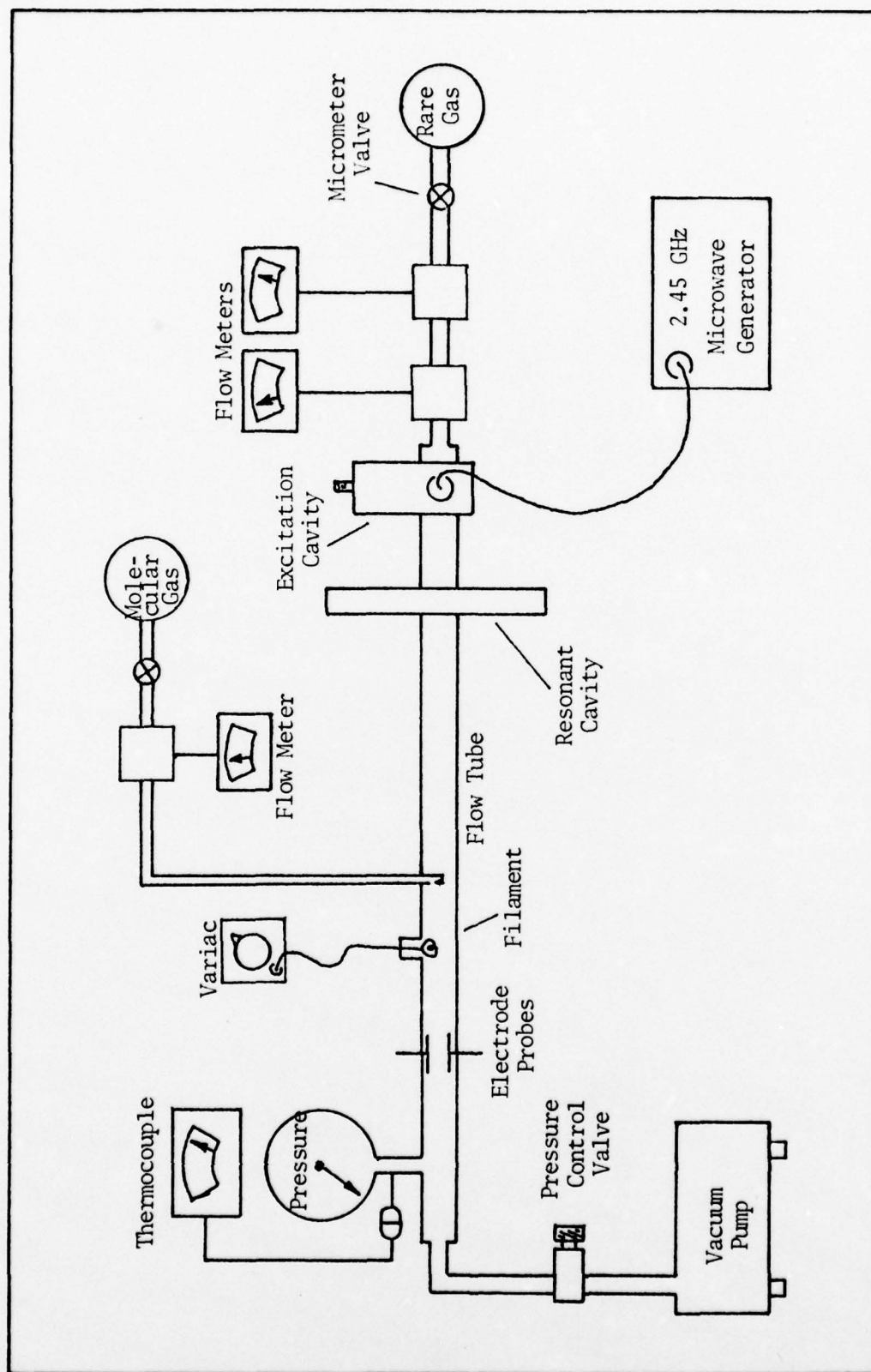


Figure 13. Experimental Setup

due to breakdown if the molecular gas were dissociated by the excitation cavity (CO and CH<sub>4</sub> were planned to be used as the molecular gas additives).

A tungsten filament is located 5 cm upstream from the electrodes to provide a thermal source of electrons to the drift field to prevent current saturation due to the gas flow being much less than the electron drift velocity. Current saturation will occur if all of the electrons in the plasma are collected by the electrodes. That is, if

$$\frac{x}{W} < \frac{z}{V_f}, \quad (17)$$

where

- $x$  = electrode separation
- $z$  = electrode length
- $V_f$  = plasma flow velocity.

It is obvious that the condition  $W > V_f$  will hold under all practical flow conditions since  $W \sim 10^6$  cm/sec and  $V_f \sim 60$  cm/sec (see "Parameters," this Chapter). The current will reach saturation at approximately .5 volts for the tube used. The electrons cannot flow faster with increasing potential and still remain a neutral plasma since the positive ions will lag;  $W(\text{ion}) \ll W(\text{electron})$ .

The electric field between the electrodes establishes a very slight charge imbalance as a result. Since the "plasma" will always attempt to remain charge neutral (Ref 17), electrons will be drawn from the filament into the drift region to maintain neutrality. A side benefit of this is that the plasma will only draw as many electrons as necessary to keep neutral, thereby maintaining a constant electron density in the drift region. The current will then be able to increase as  $E/N$  increases, provided there are sufficient electrons created at the filament to maintain charge neutrality.

The filament is controlled by a Variac voltage supply and maintained at the same potential as the electrodes by a single connection from the filament to the ammeter as shown in Fig. 14.

The diagnostics of the flow tube is shown in Fig. 14. A variable DC voltage supply provides the potential to the electrodes and a high impedance voltmeter ( $130\text{ M}\Omega$ ) measures the actual potential between the electrodes. An ammeter capable of  $10^{-12}$  amps was used to measure the current. Current and voltage characteristics were plotted directly on an X-Y recorder.

A detailed drawing of the flow tube, dimensions, and equipment list can be found in Appendix B.



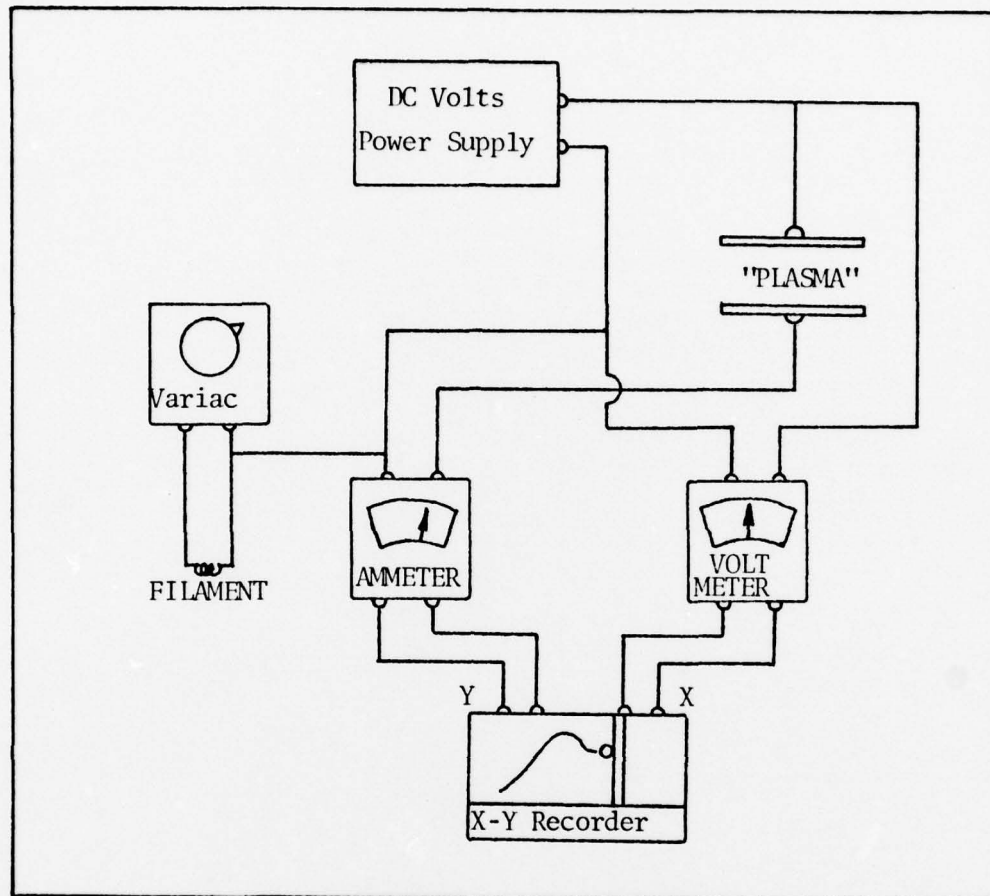


Figure 14. Diagnostics for Current-Voltage Readings.

#### Experimental Parameters

Electron Density. An electrode immersed in a plasma develops a plasma sheath. The electron and ion density within the sheath are shown in Fig. 15, for an insulating probe. In this experiment, potentials will be applied to the two collecting electrodes. This will tend to separate the ions and electrons, thereby establishing a space charge

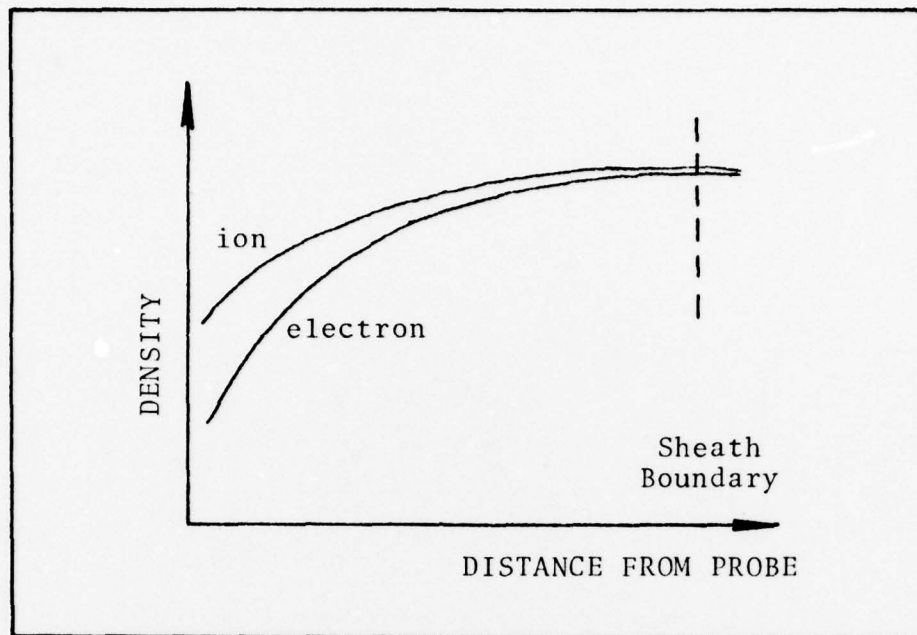


Figure 15. Electron and Ion Densities  
Within the Plasma Sheath (Ref 32)

imbalance which the plasma will attempt to limit (the plasma will always attempt to remain in a neutral space charge condition).

Within the sheath a region of space-charge imbalance (quasi-neutrality) can exist. Ideally, one wishes to operate in this region of quasi-neutrality where charge imbalance can exist so that one is not limited by charge neutrality.

Harp has shown (Ref 22) that the plasma sheath boundary is 6.75 debye lengths for a plane probe, and that the maximum space charge imbalance exists at approximately 1 to 1- $\frac{1}{2}$  debye lengths. For experimental purposes,

then, operation in a region of 2 debye lengths or less is desirable. The debye length is given by Chen (Ref 23) as

$$\lambda_d = 6.9 \left( \frac{T_e}{n_e} \right)^{1/2} \text{ cm} , \quad (18)$$

where  $T_e$  is the electron temperature in °K and  $n_e$  is the electron density in  $\text{cm}^{-3}$ . Solving for  $n_e$  :

$$n_e = \frac{(6.9)^2 T_e}{\lambda_d^2} . \quad (19)$$

The temperature of the electrons is taken to be 300° K and  $\lambda_d$  to be half the electrode separation so that two debye lengths will exist between the electrodes. Substitution of values in Equation (19) sets the parameter for the electron density:

$$n_e \leq 1.16 \times 10^5 \text{ cm}^{-3} .$$

Typical values obtained for  $n_e$  were on the order of  $10^4 \text{ cm}^{-3}$ . The electron density was measured by the method presented in Chapter IV.

Pressure. The drift velocity phenomena to be observed is heavily dependent on collisional processes. It is, therefore, desirable that the electrons have sufficient collisions with neutral atoms prior to reaching the electrodes. More succinctly, the mean free path,  $\lambda_m$  ,

should be less than the dimensions of the electrode. The mean free path is given by

$$\lambda_m = \frac{1}{\sigma_{mt} n_a} \quad , \quad (20)$$

where  $\sigma_{mt}$  is the collisional cross section for mass transfer in  $\text{cm}^2$  and  $n_a$  is the density of neutral atoms in  $\text{cm}^{-3}$ . Then,

$$n_a = \frac{1}{\sigma_{mt} \lambda_m} \text{ cm}^{-3} \quad . \quad (21)$$

But  $n_a$  is a function of pressure and related by the expression

$$n_a = (9.65 \times 10^{18}) \frac{P}{T} \text{ cm}^{-3} \quad , \quad (22)$$

where  $P$  is the pressure in torr and  $T$  is the gas temperature in  $^{\circ}\text{K}$ . Rearranging terms and substituting Equation (22) into Equation (21) gives the criteria for the pressure:

$$P = \frac{T}{\sigma_{mt} \lambda_m (9.65 \times 10^{18})} \text{ torr} \quad . \quad (23)$$

An average value for  $\sigma_{mt}$  is  $2.35 \times 10^{-16} \text{ cm}^2$  (Ref 2), although it is actually a function of electron energy.

It was arbitrarily decided that an electron should undergo ten collisions before reaching the electrodes,



so  $\lambda_m$  should be .05 cm. Substitution of the values in Equation (23) sets the parameter for the minimum pressure:

$$P = 2.6 \text{ torr} .$$

Flow Rate. The flow rate used was based on the electron number density decay from the microwave exciter to the electrodes (see Chapter IV). The electron loss as a function of time was determined, and then the flow rate was adjusted (time parameter), to obtain the desired electron density. A flow rate of 65 cm/sec was used for the measurements taken. This corresponds to a flow rate of 18 SCCM on the mass flow meters.

Filament Current. The voltage source for the filament used for the thermal source of electrons was adjusted while a scan of electrode current and voltage was taken. When the electrode current no longer increased when filament current was increased, a sufficient supply of electrons was available to prevent saturation.

Vacuum System. The importance of a good vacuum system cannot be overstressed since molecular impurities such as nitrogen and oxygen found in air have significant effects on the drift velocity. The base pressure of the system was  $22 \times 10^{-3}$  torr . The drift velocity measurements were taken at 2.6 torr. A leak-check was performed to determine impurity flow rate. A leak rate of .2  $\mu$ /sec

was found, giving an impurity level due to leaks of .005%.

### Procedure

The rare gas flow was set to 18 SCCM and the pressure adjusted to 2.6 torr. The microwave excitation cavity was energized and adjusted to an acceptable (approximately  $4.3 \times 10^7 \text{ cm}^{-3}$ ) initial electron density as measured by the resonant cavity. Power output from the microwave source was kept below 42 Watts. Greater power settings led to excessive microwave surface waves around the excitation cavity. The filament was adjusted to the level previously determined.

The potential applied to the electrodes was swept between  $\pm 50$  Volts to give an  $E/N$  range of  $\pm 8.37 \times 10^{-16} \text{ V-cm}^2$ . Current and voltage characteristics were plotted on the X-Y recorder. Gas mixtures of 0%, 1%, 2%, 5%, 10%, and 20% molecular gas added to the rare gas diluent were examined. Care was taken to ensure constant pressure and flow rate were maintained after adjusting the percentage of gas mixture. The current-voltage plots were then transcribed to plots of drift velocity vs  $E/N$ .

#### IV. Electron Density Measurement

The number of free electrons is the key factor which determines the transport characteristics of any plasma. Since the electron density which is needed for drift velocity calculations is that which exists between the probe electrodes, density measurement by a microwave resonant cavity alone is impossible. This section discusses the experimental technique developed by the author to accurately establish the electron density.

##### Electron Loss Curves

There are four electron loss processes in a discharge: free electron diffusion, attachment, ambipolar diffusion, and recombination. The equations for each of the loss processes, as well as accurate transport coefficients, are available in the literature (for example, Refs 2, 17, 24 and 25). There is, however, difficulty with knowing how much of each is actually taking place. There might also be other experimental conditions that affect electron loss that are not obvious or well known. Even with all loss mechanisms contributing, the decay of electrons is exponential, and this is the basis for the density measurement.

The microwave excitation cavity is positioned at the far end of the flow tube (see Fig. 16(a)). A constant

voltage (5 Volts) was applied to the electrodes. The cavity was then moved toward the electrodes in 1 cm intervals (see Fig. 16 (b & c)), noting the current at each interval. If the voltage is kept constant, the current change is due to the change in electron density. When a plot is made of current vs distance-from-electrodes, an exponential curve is obtained which describes the sum of the electron loss processes.

The procedure now is to obtain a curve fit to the experimental plot of current vs distance. We assume a form of

$$i = i_0 e^{-ax+b}, \quad (24)$$

where  $i_0$  = initial current as determined by the resonant cavity, and  $a$  and  $b$  are determined by the curve fit procedure (Ref 26). The current can be expressed as a function of electron density by

$$i = e n_e A W .$$

Substitution in Equation (24) yields

$$e n_e A W = e n_{e_0} A W_0 e^{-ax+b} . \quad (25)$$

But the drift velocity will remain constant as long as



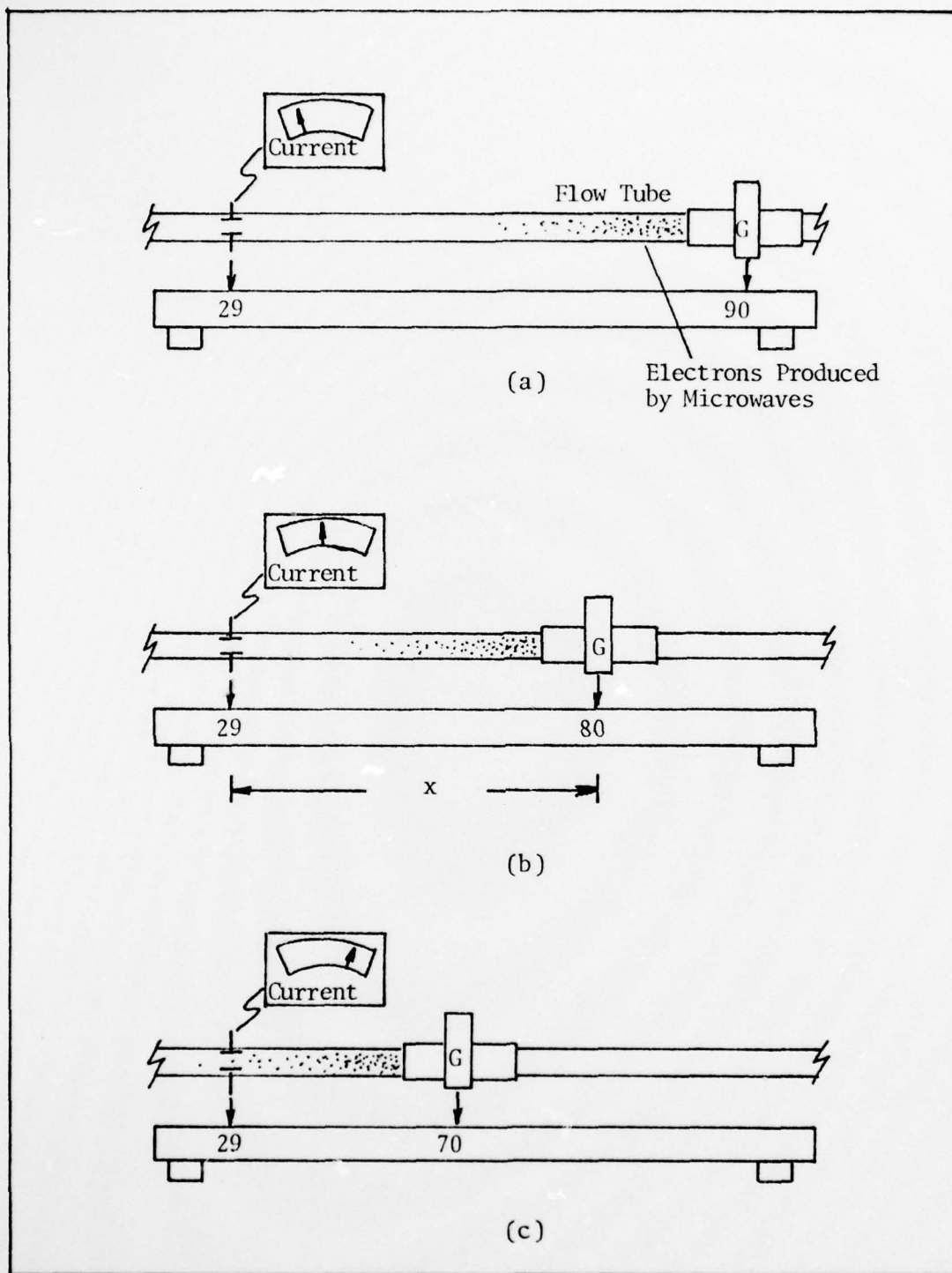


Figure 16. Experimental Procedure for Obtaining Current vs Distance Curves

a constant potential is kept across the electrodes; that is,  $W = W_0$  . The final result is

$$n_e = n_{e_0} e^{-ax+b} . \quad (26)$$

This equation constitutes the electron decay as a function of distance due to all loss processes. It should be noted that the exponent may not be linear in  $x$  , and is in most afterglow experiments of higher order in  $x$  . Plotting current vs distance on semi-logarithmic paper will reveal linearity.

The only unknowns that now remain are the initial number density,  $n_{e_0}$  , and the distance,  $x$  , at which  $n_{e_0}$  is measured. A microwave resonant cavity was used to measure the electron density at a point one inch downstream from the excitation cavity (a full presentation of this procedure and theory can be found in Appendix A). The distance  $x$  was measured from the center of the resonant cavity to the center of the electrodes.

#### Alternate Method

When the same flow rate is to be used in the experiment as in the density curve determination, a particularly simple technique can be used. By knowing the distance from the resonant cavity to the electrodes and the initial and final currents from the density curve, the ratio

$$n_{e_f} = \frac{(n_{e_o})(i_f)}{i_o}, \quad (27)$$

where

$n_{e_o}$  = electron density at the resonant cavity ( $\text{cm}^{-3}$ )

$n_{e_f}$  = electron density between the electrodes ( $\text{cm}^{-3}$ )

$i_o$  = current from the density curve where  $n_{e_o}$   
was measured

$i_f$  = current from the density curve between  
the electrodes (amps)

can be used to find the electron density between the electrodes. A sample calculation using this method can be found in Appendix F.

#### Experimental Technique

An X-Y recorder was first used to obtain the current vs distance curves. Since the microwave exciter had to be moved by hand, the X-axis of the plotter (distance axis) had also to be moved manually. This, coupled with excessive noise in the plotter at low current readings in the nano-amp range, made manual plotting necessary. Several runs were taken with helium, argon, and nitrogen to ensure consistent results for each gas that was excited by the microwaves.

It was found that surface waves on the quartz tube generated by the excitation cavity reacted unfavorably with the resonant cavity when within 1.5 cm of each other. This caused slight perturbations in current readings when the two cavities were in close proximity. The resonant cavity was not of hemispherical split design (see Appendix A), so removal of the cavity was tedious and in some instances not done at all. A cavity of "split" design is recommended for all future measurements involving the procedure outlined in this section.



## V. Results and Recommendations

### Results

General. Results for mixtures of Ar-N<sub>2</sub>, Ar-CO, and He-N<sub>2</sub> are presented in this chapter. Early analysis by many authors (Refs 5, 6, and 13) have shown that drift velocities in argon are extremely sensitive to small amounts of molecular impurities due to the small momentum transfer cross section at low electron energies. This analysis, therefore, includes an interpretation of impurity levels, both from the system and from the tank gas used. The experimental data are compared to theoretical curves of drift velocity vs E/N. Theoretical curves of Long et al. (Ref 1) were used which were determined to be accurate to within 5% of previous experimental results over the E/N range considered where impurity levels were strictly controlled.

In each gas mixture current-voltage measurements were taken at 2.6 torr, 5.2 torr, and 7.8 torr where the pressure was controlled by the pressure control valve (see Fig. 13). No effects due to pressure changes were noted when data were normalized in E/N and electron density; therefore, it was concluded that impurities were due to tank gas impurities.

Complete system pump-down to base pressure to remove molecular impurities was necessary between each set of

current-voltage readings to obtain consistent results. Reproducible results were achieved when an increasing mixture ratio scheme was used (i.e., 0% to 20%, not 20% to 0% molecular gas added). This prevents residual molecular gas from affecting the mixture ratio due to the long pump-down time required for the narrow molecular gas probe. Complete pump-down of the flow system was performed after the 20% mixture current-voltage curve was taken to ensure removal of all molecular impurities. This was not necessary, but was done anyway, when using the He-N<sub>2</sub> mixtures, since small amounts of impurities had only slight effects (.5% impurities give less than 5% error in drift velocity).

Viscous flow was not considered to have a significant effect on the results obtained. It was assumed that turbulence created by the two ports positioned before the electrodes, as well as the gas probe itself, eliminated effects due to viscosity at the flow rates used.

There are several sources of error in this experiment where gauge readings were taken and current-voltage curves were transposed to drift velocity curves. Several runs were taken for each gas mixture ratio to obtain a statistical average at each data point to minimize errors due to gauge readings. The most significant source of error is in determining the exact electron density between the electrodes. Its effect on drift velocity calculations is linear and affects the magnitude of  $W$  only. Electron

density measurements are considered accurate to within 15%; therefore, drift velocity curves are accurate to within a minimum of 15%.

A basic assumption in drift velocity measurements is that the electrons move in a uniform electric field. The solution of the plasma sheath equation for the sheath potential due to an insulating plane electrode shows that deviations from linearity is negligible when two Debye lengths or less are considered as in this experiment (Ref 22). However, when a potential is applied to the electrodes, the sheath potential profile changes. The solution to the sheath equation for variable potentials applied to two plane probes in a plasma is not trivial. Since there was good agreement of experimental results with theory, errors due to the deviation of the potential profile from linearity were not considered significant.

An error analysis is given in Appendix E.

Argon-Nitrogen Mixture. High purity argon (40 parts per million) was used in this experiment. Figures 17 through 22 show the experimental results for argon with 0%, 1%, 5%, 10%, and 20% added nitrogen. The actual impurity level of the tank argon was indeterminate. However, comparison of the 0% added  $N_2$  experimental curve with the 1% added  $N_2$  theoretical curve (see Fig. 23) shows empirically an approximate impurity level of .77% (primary impurities in tank argon is  $N_2$ ). As a result, the 0%, 1%,

and 5% added  $N_2$  experimental curves are, in reality, .77% 1.77%, and 5.77% added  $N_2$  curves. The dot-dashed line (— · — ·) in the curves for 0%, 1%, and 5% added  $N_2$  are the theoretical curves to account for the .77% impurity level. The other curves of 10% and 20% added  $N_2$  are not significantly affected by the approximate .77% impurity level.

There is a discrepancy in the magnitude of the experimental drift velocity curves. This magnitude is roughly constant over the E/N range of each curve and increases with mixture ratio. A change in the net ambipolar diffusion coefficient as a result of the gas mixture was ruled out as a cause for the discrepancy since the net diffusion coefficient would decrease as a result of the mixture. That is, the coefficients add together as

$$\frac{1}{D_{Ar-N_2}} = \frac{1}{D_{Ar}} + \frac{1}{D_{N_2}} \quad .$$

Since the magnitude of the discrepancy is roughly constant, an error in predicting the electron number density seems likely. Convective flow around the gas probe caused by the spray of nitrogen gas being added may enhance the flow of electrons and ions to the walls of the flow tube, causing a loss of electrons. The magnitude of this effect was not determined due to time constraints.



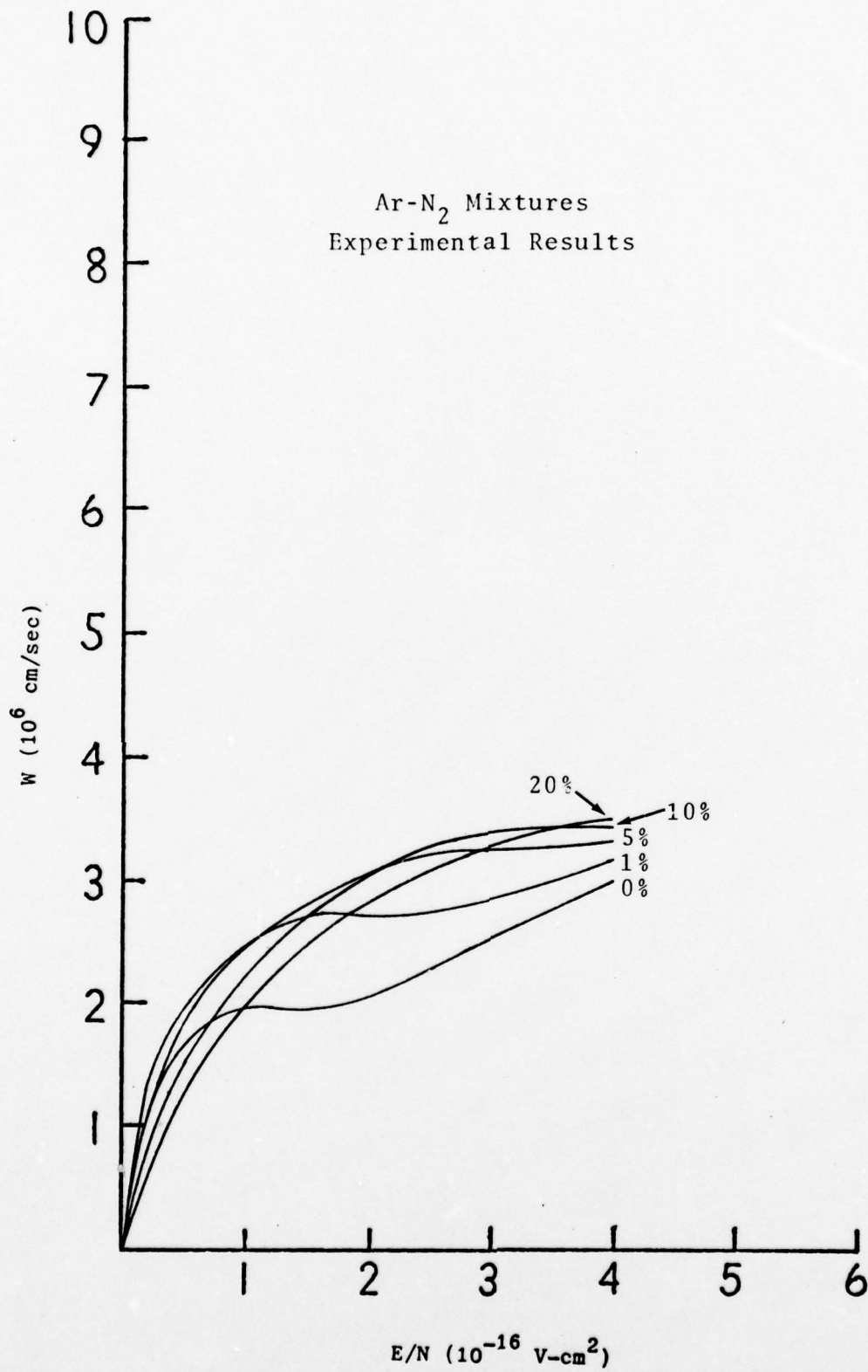


Figure 17. Experimental Results for Electron Drift Velocities in Argon with 0%, 1%, 5%, 10%, and 20% Added N<sub>2</sub>.

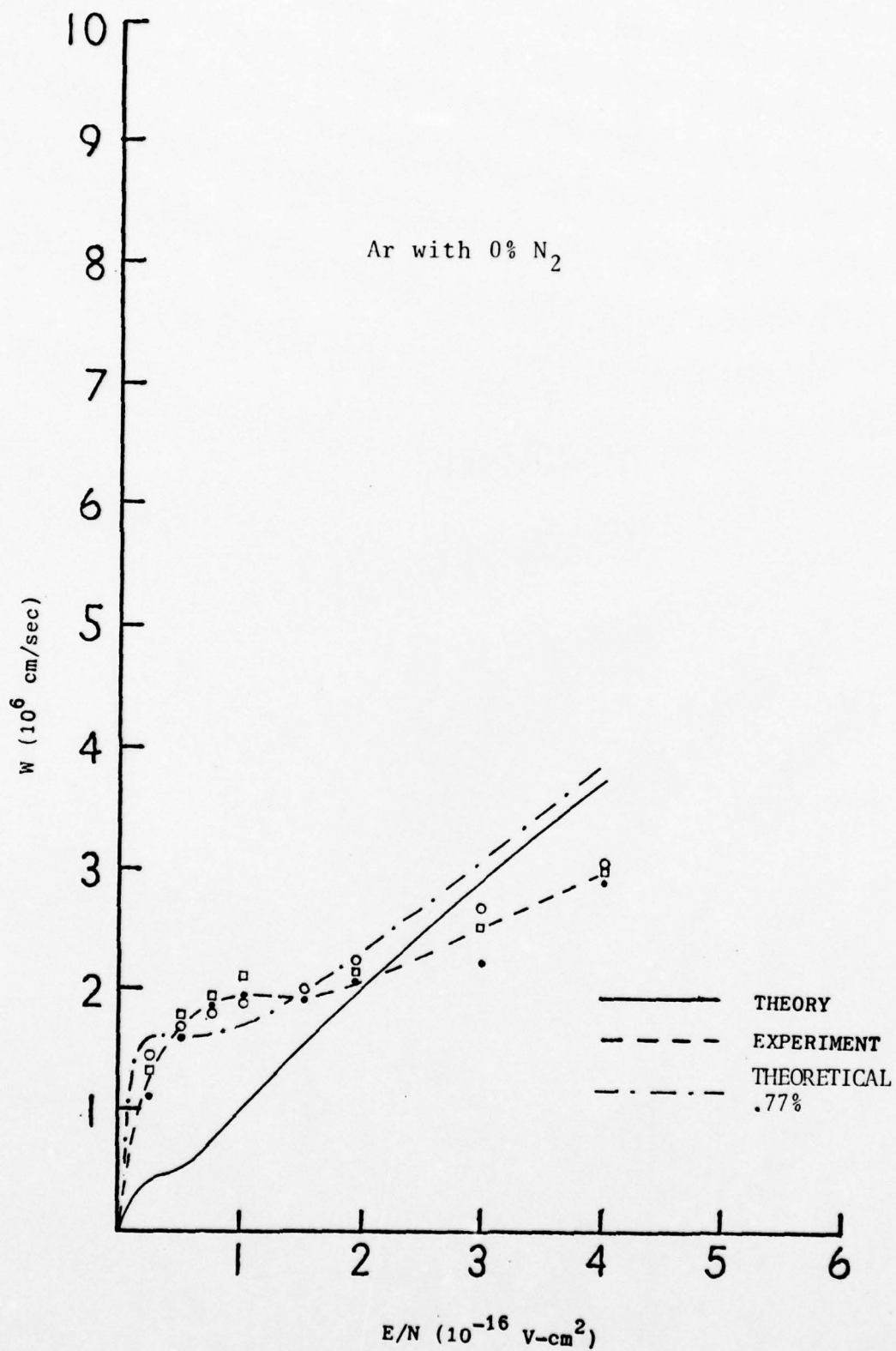


Figure 18. Electron Drift Velocity in Ar with 0% N<sub>2</sub> Added. Comparison of Theory with Experiment.

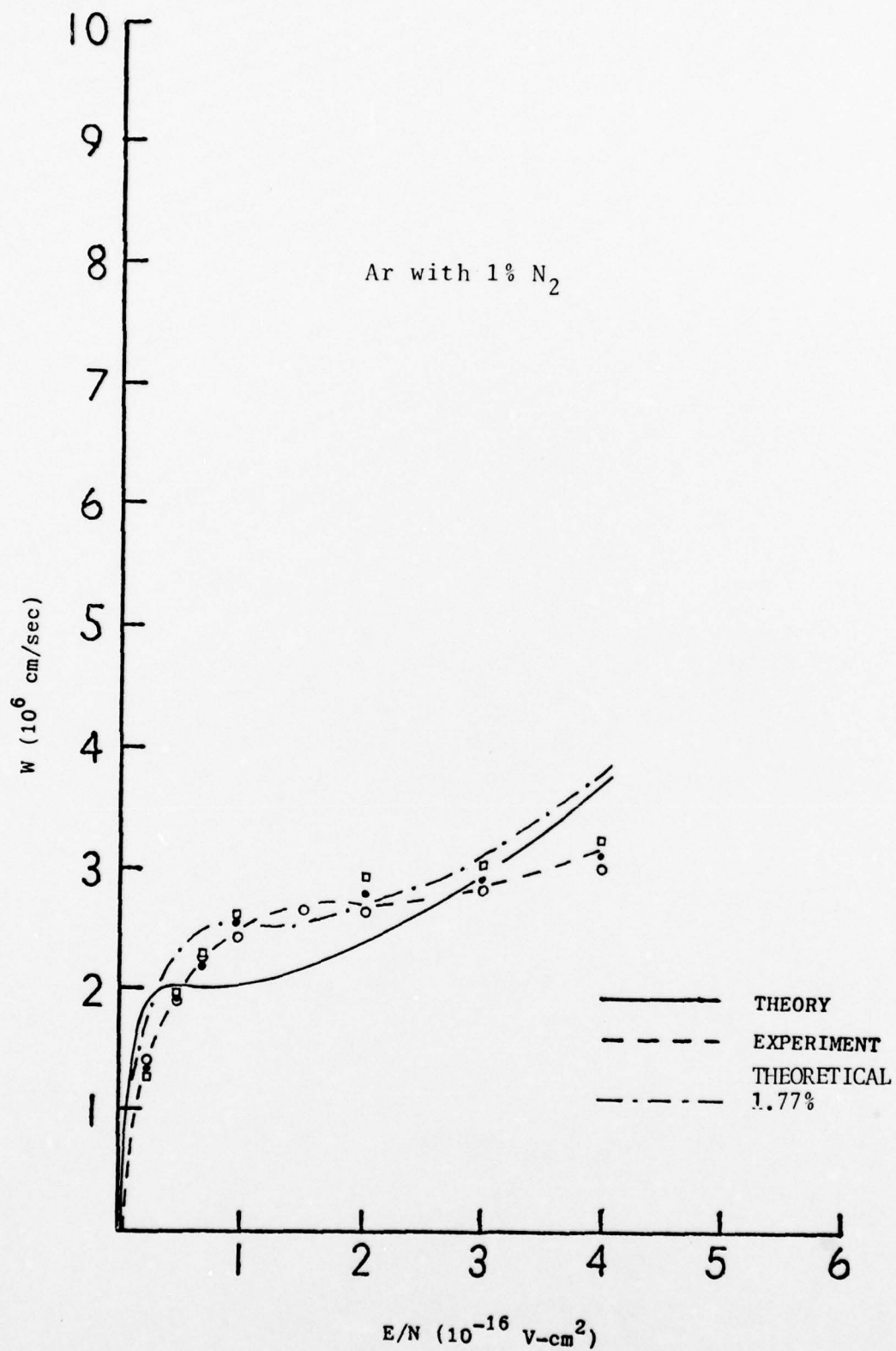


Figure 19. Electron Drift Velocity in Ar with 1% N<sub>2</sub> Added. Comparison of Theory with Experiment.

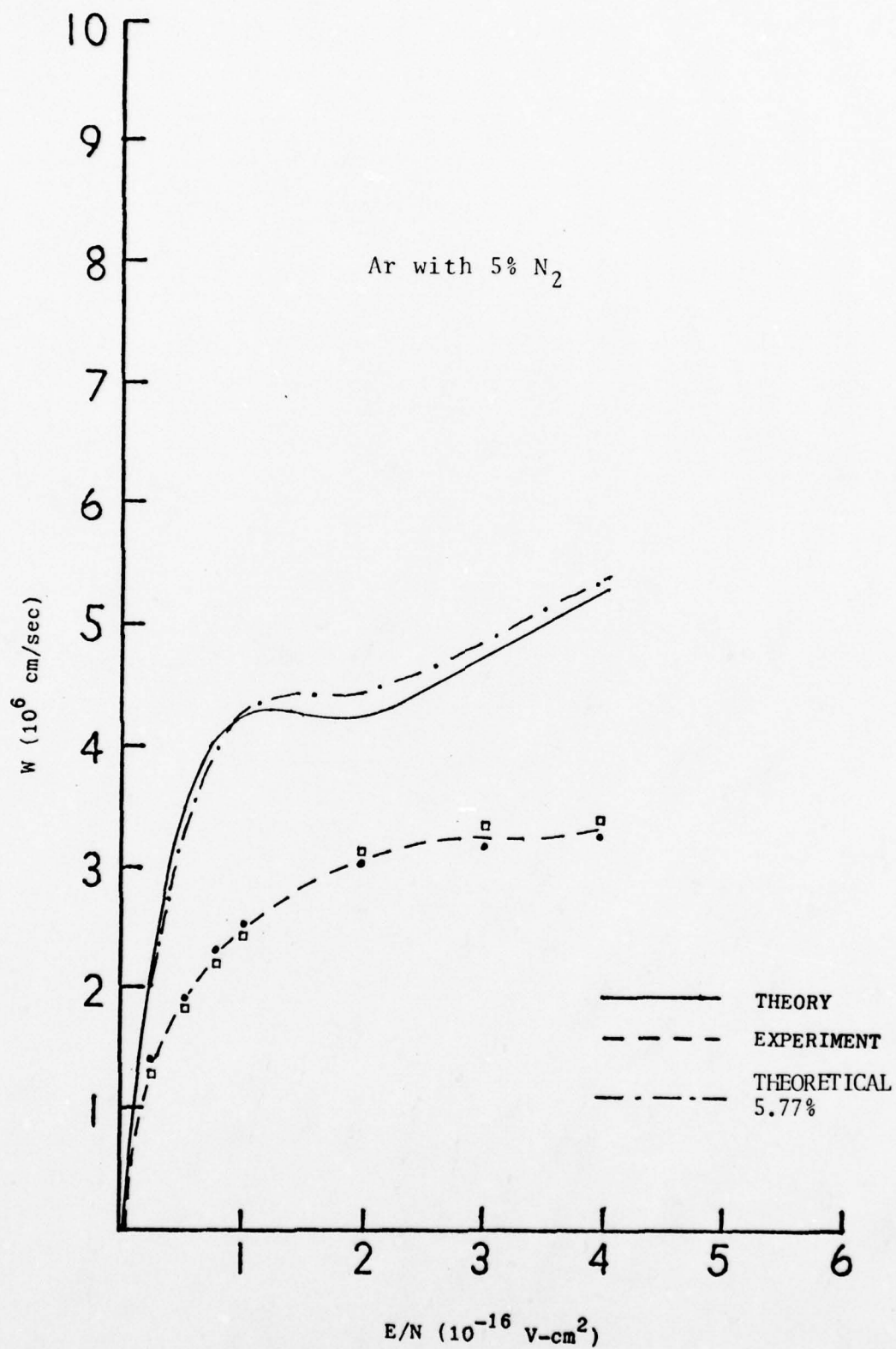


Figure 20. Electron Drift Velocity in Ar with 5% N<sub>2</sub> Added. Comparison of Theory with Experiment.



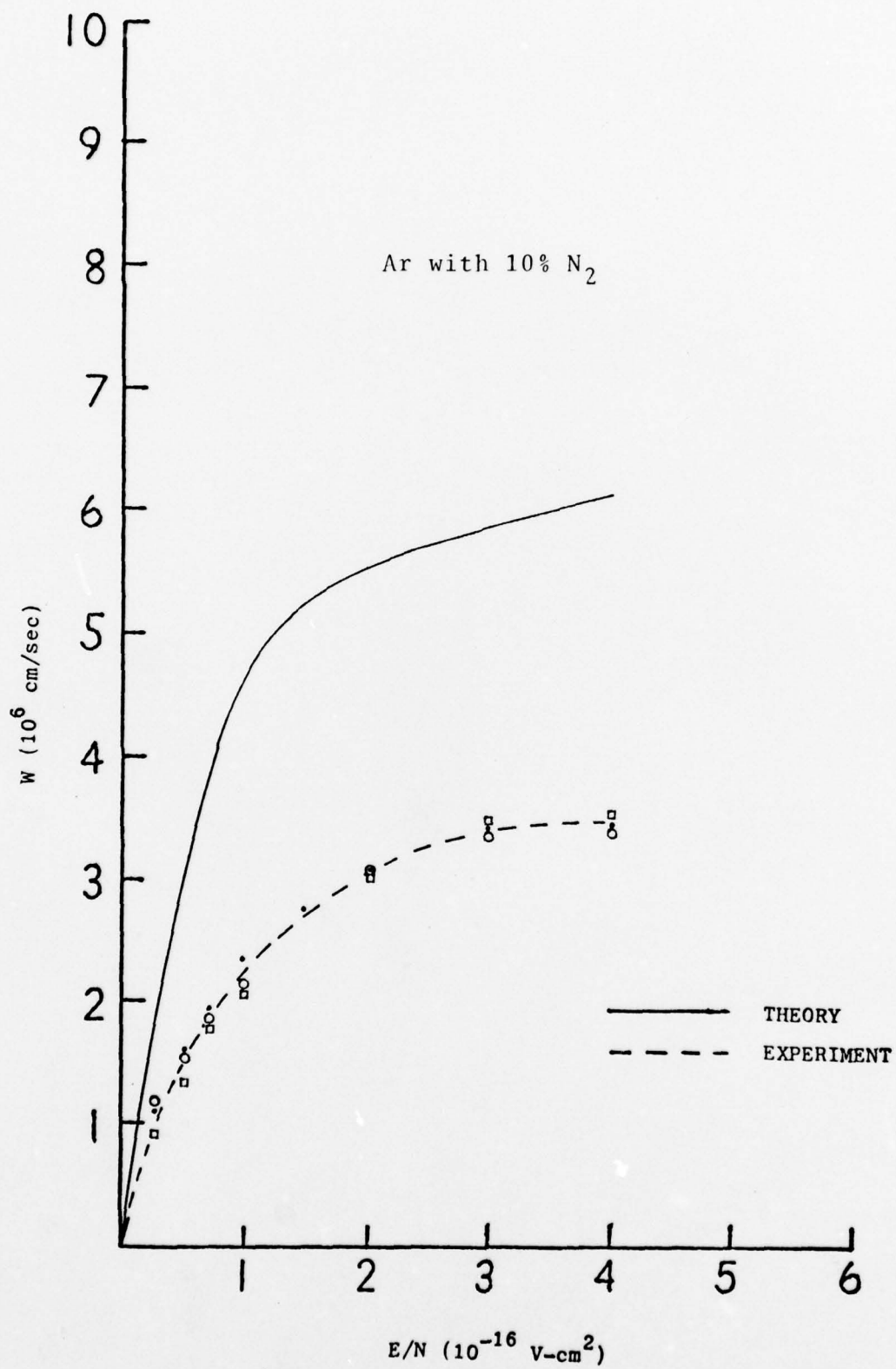


Figure 21. Electron Drift Velocity in Ar with 10% N<sub>2</sub> Added. Comparison of Theory with Experiment.

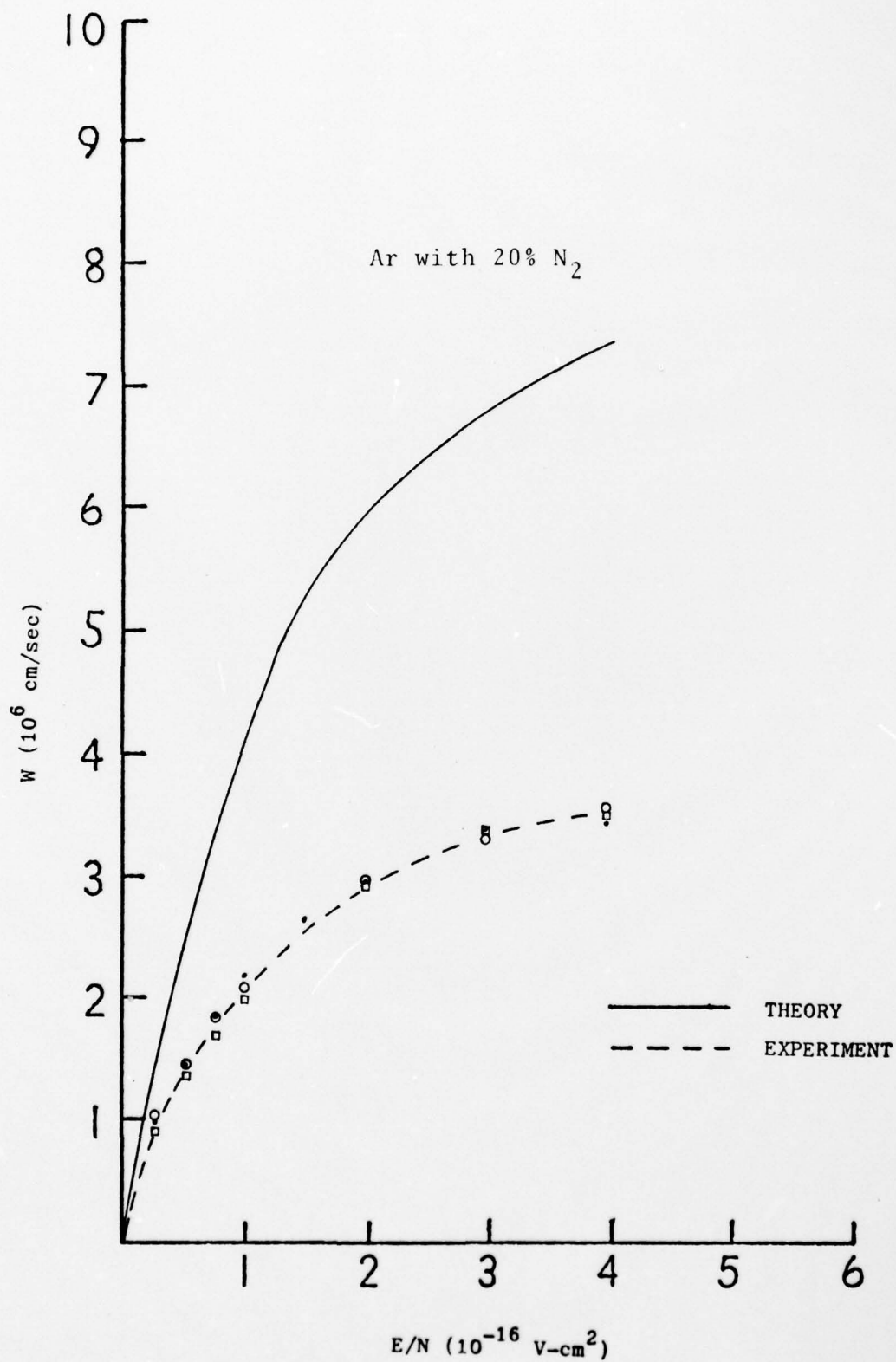


Figure 22. Electron Drift Velocity in Ar with 20% N<sub>2</sub> Added. Comparison of Theory with Experiment.

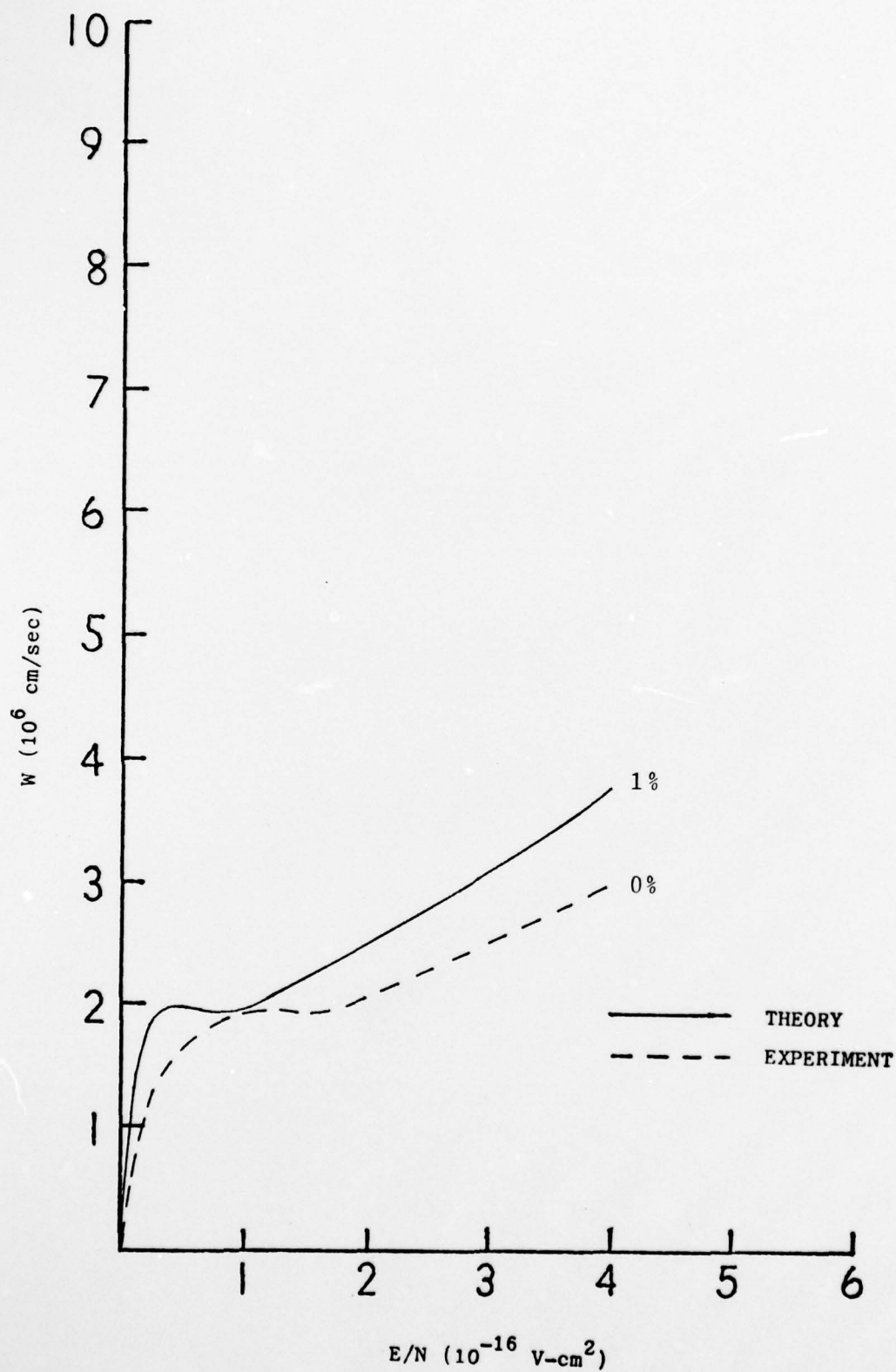


Figure 23. Comparison of Experimental 0% Added  $N_2$  in Ar with Theoretical 1% Added  $N_2$  in Ar.

Argon-Carbon Monoxide Mixtures. The electron drift velocity curves for 0%, 1%, 5%, 10%, and 20% added carbon monoxide to argon are given in Figs. 24 through 29.

The CO used was 99.5% pure with .5% of unknown impurities. The tank impurities of Ar are the same as discussed in the Ar-N<sub>2</sub> mixtures.

Differential negative conductivity is more pronounced in the Ar-CO mixtures than the Ar-N<sub>2</sub> mixtures; however, the prominence of the local maximum predicted by theory for Ar-CO is lacking. Molecular impurities other than CO may mask the effect to some extent; however, it is not likely to be the only mechanism involved.

There is a significant difference between the experimental pure argon curve for the Ar-N<sub>2</sub> mixtures and the experimental pure argon curve for the Ar-CO mixtures. Since the experimental apparatus was left open at atmospheric pressure for one week prior to taking the Ar-CO readings, it was believed that water vapor entered the system and may have caused the deviation. The Ar-CO mixtures were tested last so that this effect was not observed in the Ar-N<sub>2</sub> mixture.

The discrepancy in the magnitude of the other experimental curves as compared to the theoretical curves can be attributed in part to convective flow previously discussed in Ar-N<sub>2</sub> mixtures section.



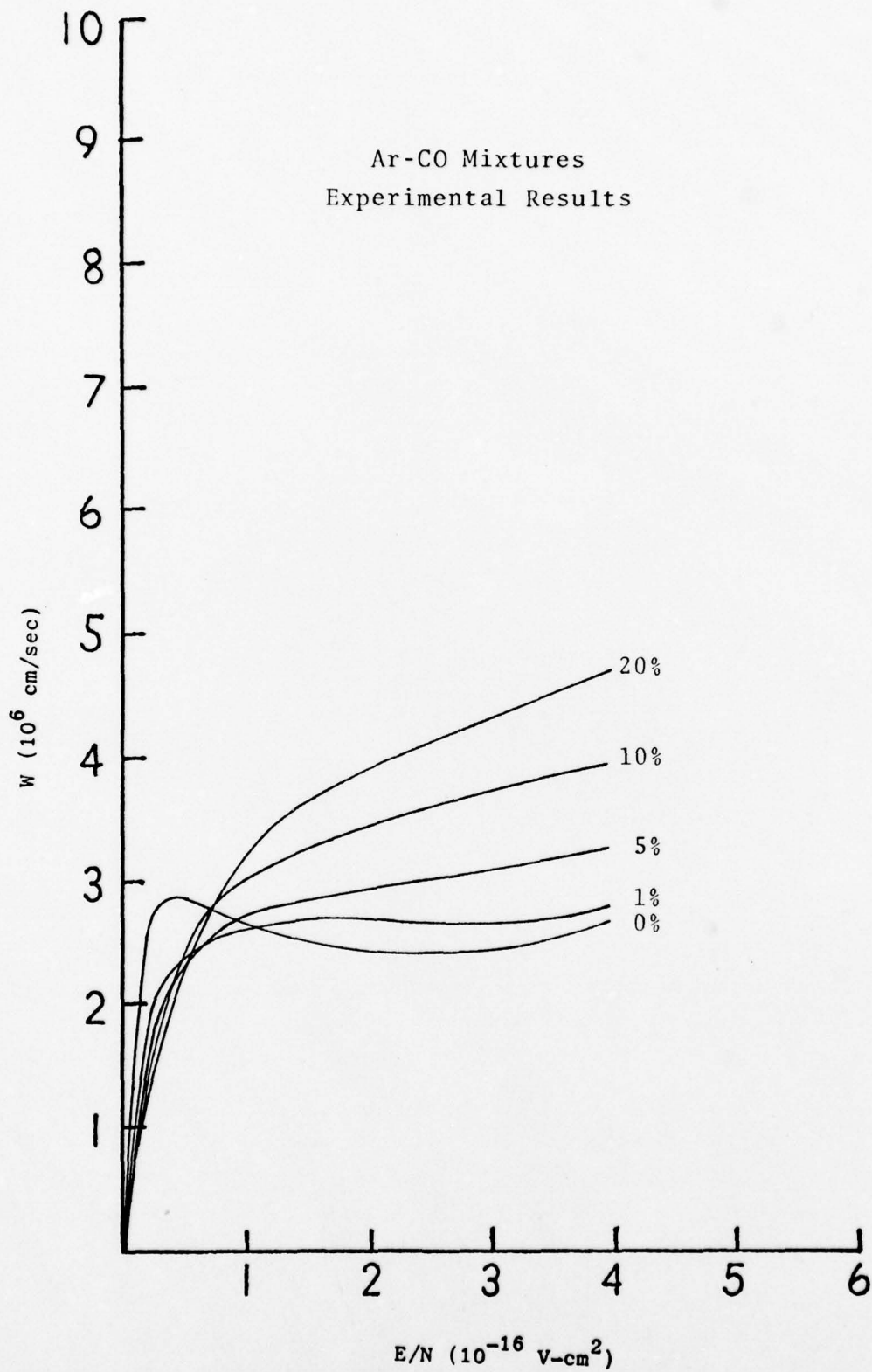


Figure 24. Experimental Results for Electron Drift Velocities in Ar with 0%, 1%, 5%, 10%, and 20% Added CO.

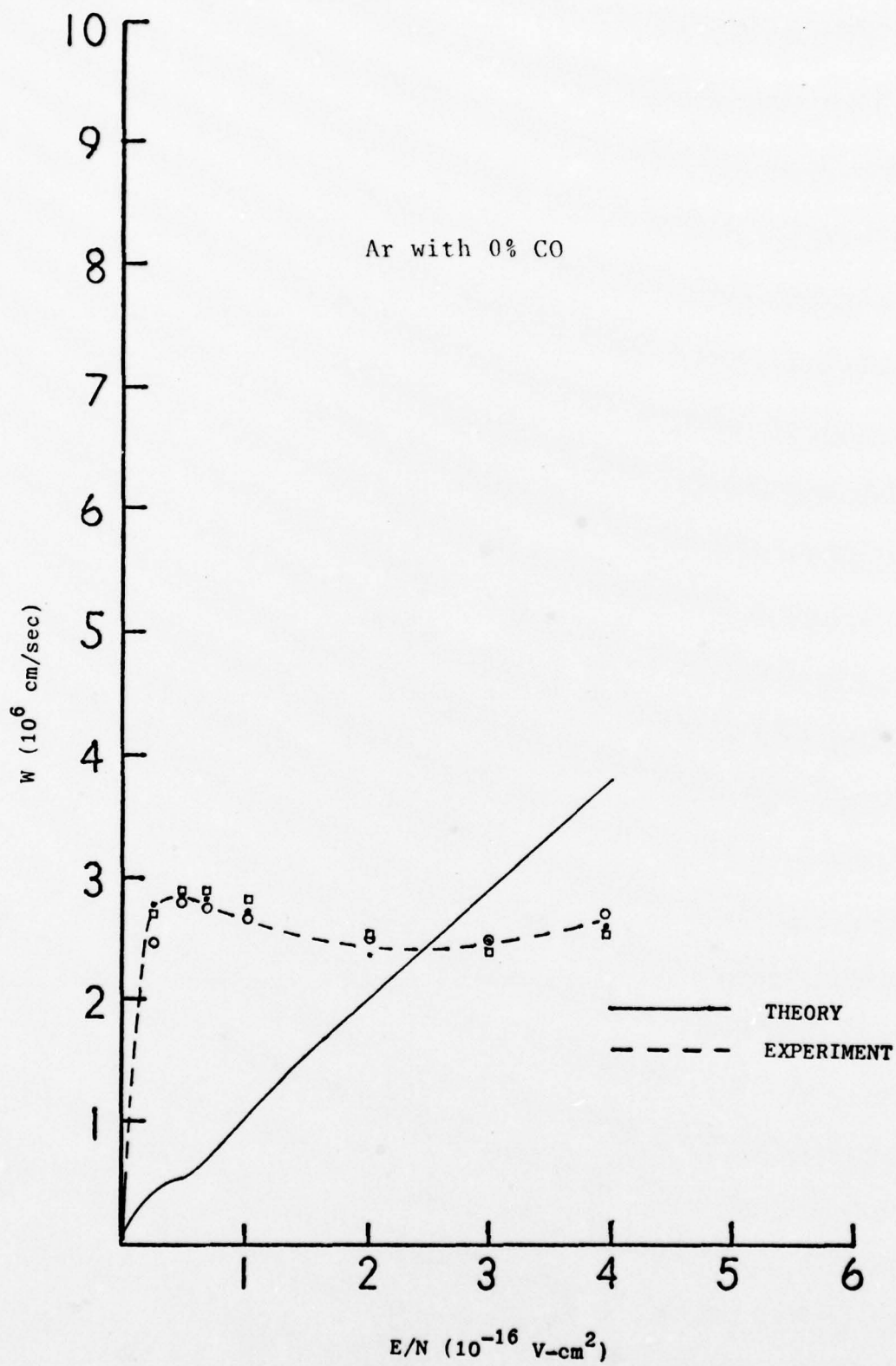


Figure 25. Electron Drift Velocities in Ar with 0% Added CO. Comparison of Theory with Experiment.

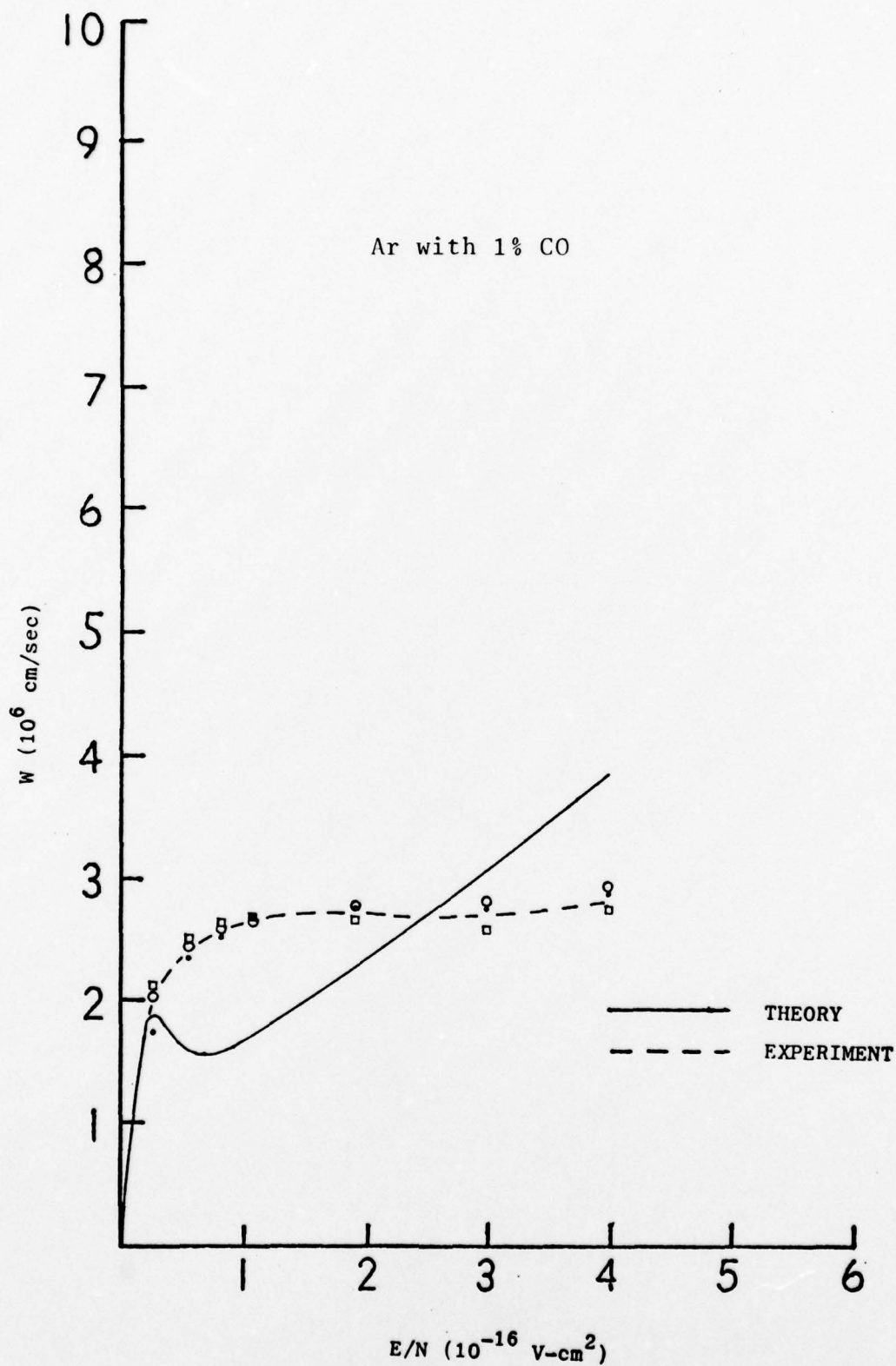


Figure 26. Electron Drift Velocities in Ar with 1% CO Added. Comparison of Theory with Experiment.

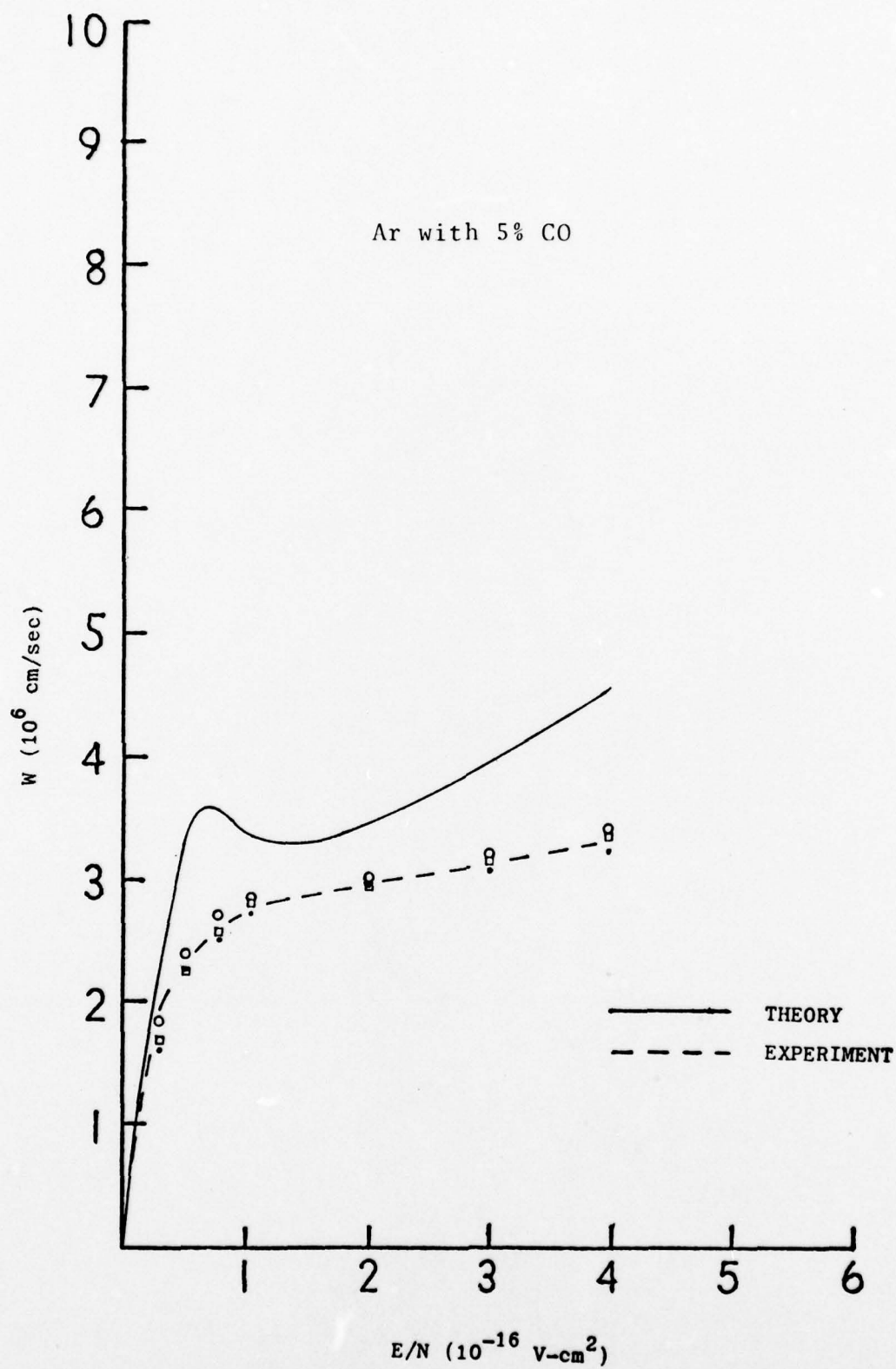


Figure 27. Electron Drift Velocities in Ar with 5% CO Added. Comparison of Theory with Experiment.



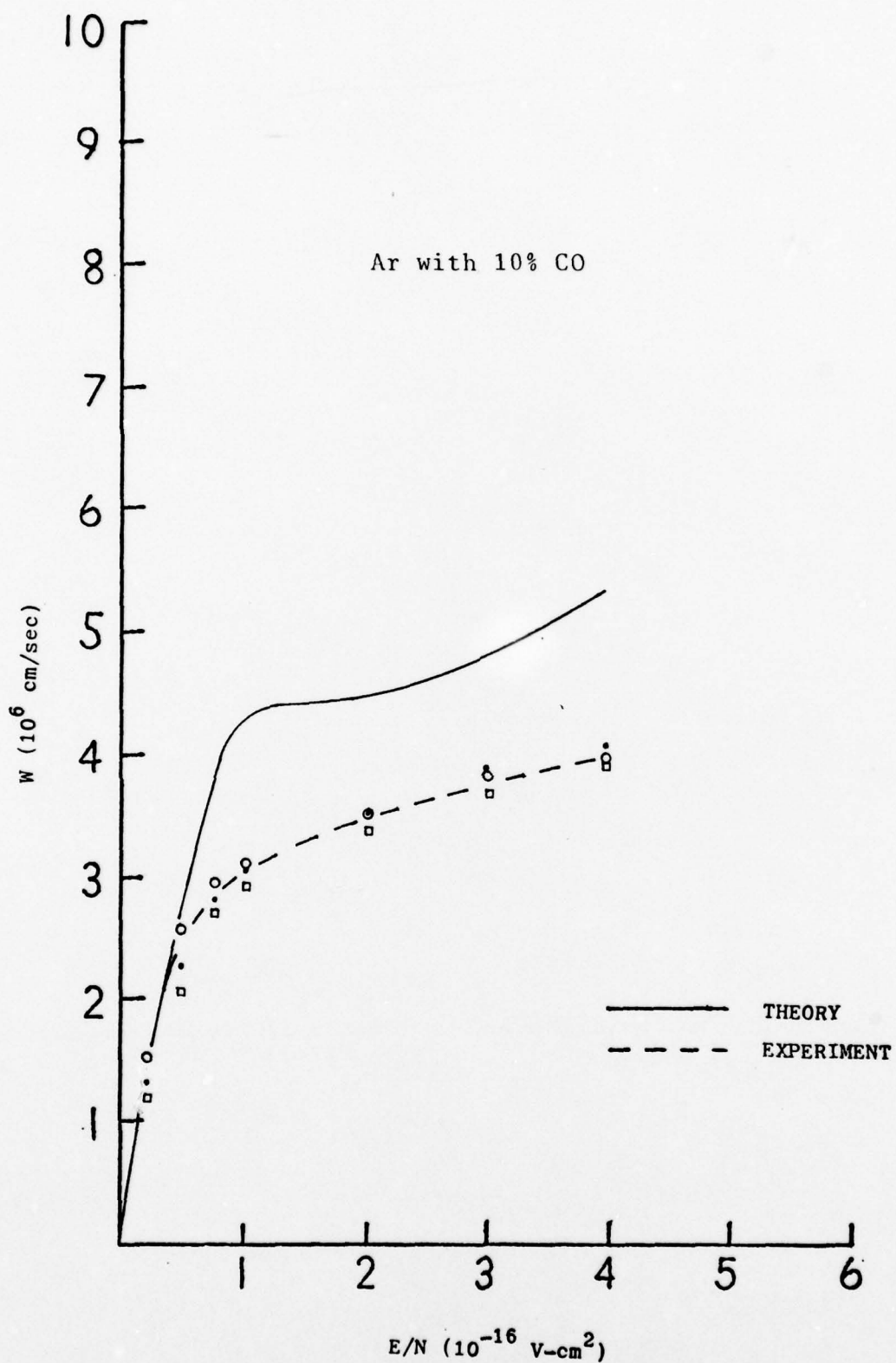


Figure 28. Electron Drift Velocities in Ar with 10% CO Added. Comparison of Theory with Experiment.

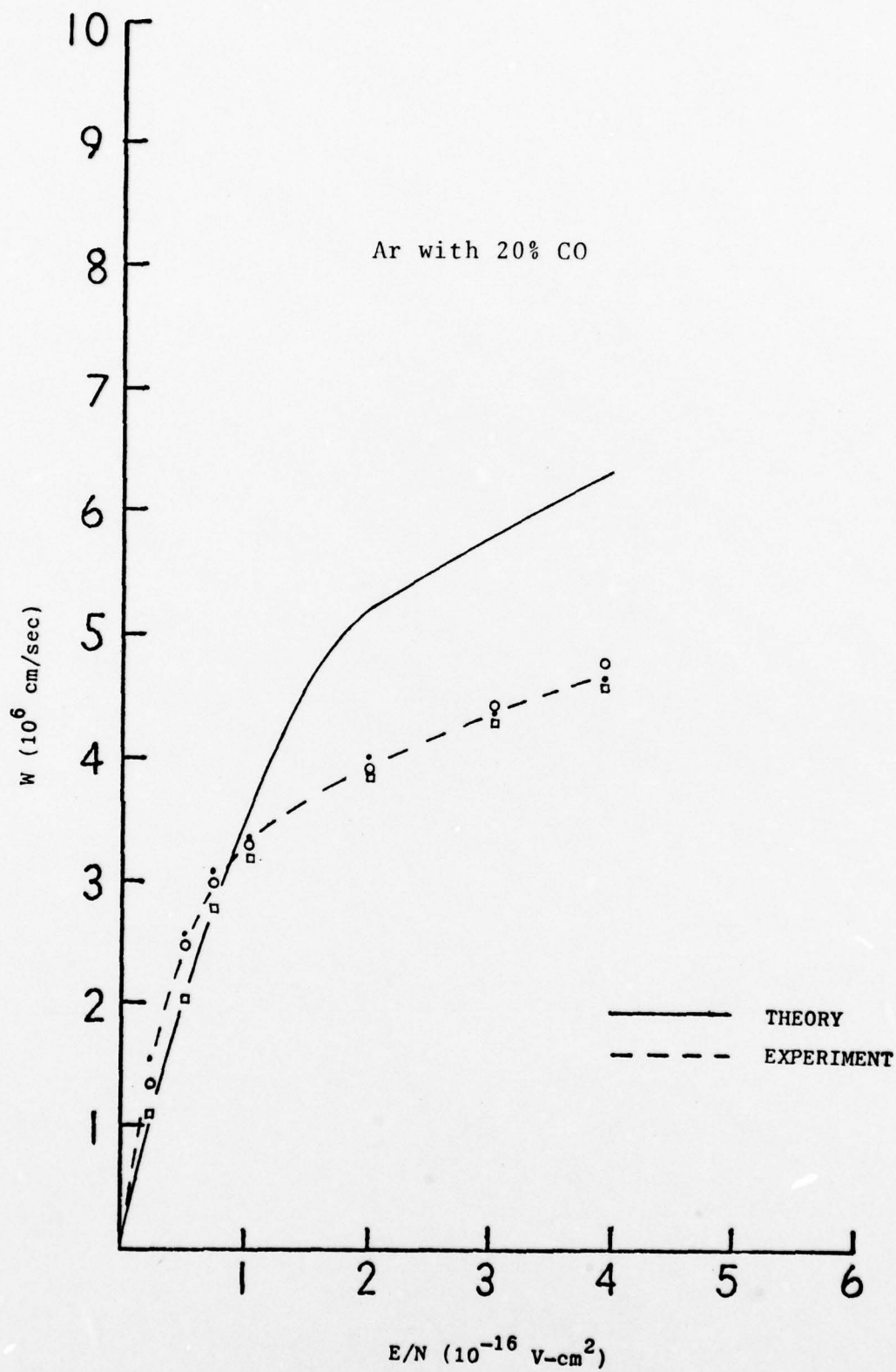


Figure 29. Electron Drift Velocities in Ar with 20% CO Added. Comparison of Theory with Experiment.

Helium-Nitrogen Mixtures. High purity helium (50 ppm) was used in this experiment. Because the momentum transfer cross section of helium is fairly constant and of significant value (not zero) over the range of electron energies of interest, small amounts of impurities, even of 1%, were not anticipated to have a dramatic effect on the drift velocity.

Figures 30 through 35 show the drift velocity results for 0%, 1%, 5%, 10%, and 20% added nitrogen in helium. Experimental results show good agreement with theory throughout the entire range of E/N and mixture ratios considered.

When the He-N<sub>2</sub> mixture was first attempted, helium was excited by the microwave source and the nitrogen fed in by the probe downstream. The current-voltage curves for this arrangement are presented in Figure 36. Significant deviations from theory are evident, as N<sub>2</sub> should have little effect on the pure He drift velocity. When N<sub>2</sub> was excited by the microwave source and He added by the probe downstream, good agreement with theory (within experimental error) was obtained as shown in Figures 30 through 35.

It was determined that, when helium was excited, \*He<sup>3</sup>S metastables were created on the order of  $10^{11} \text{ cm}^{-3}$ .

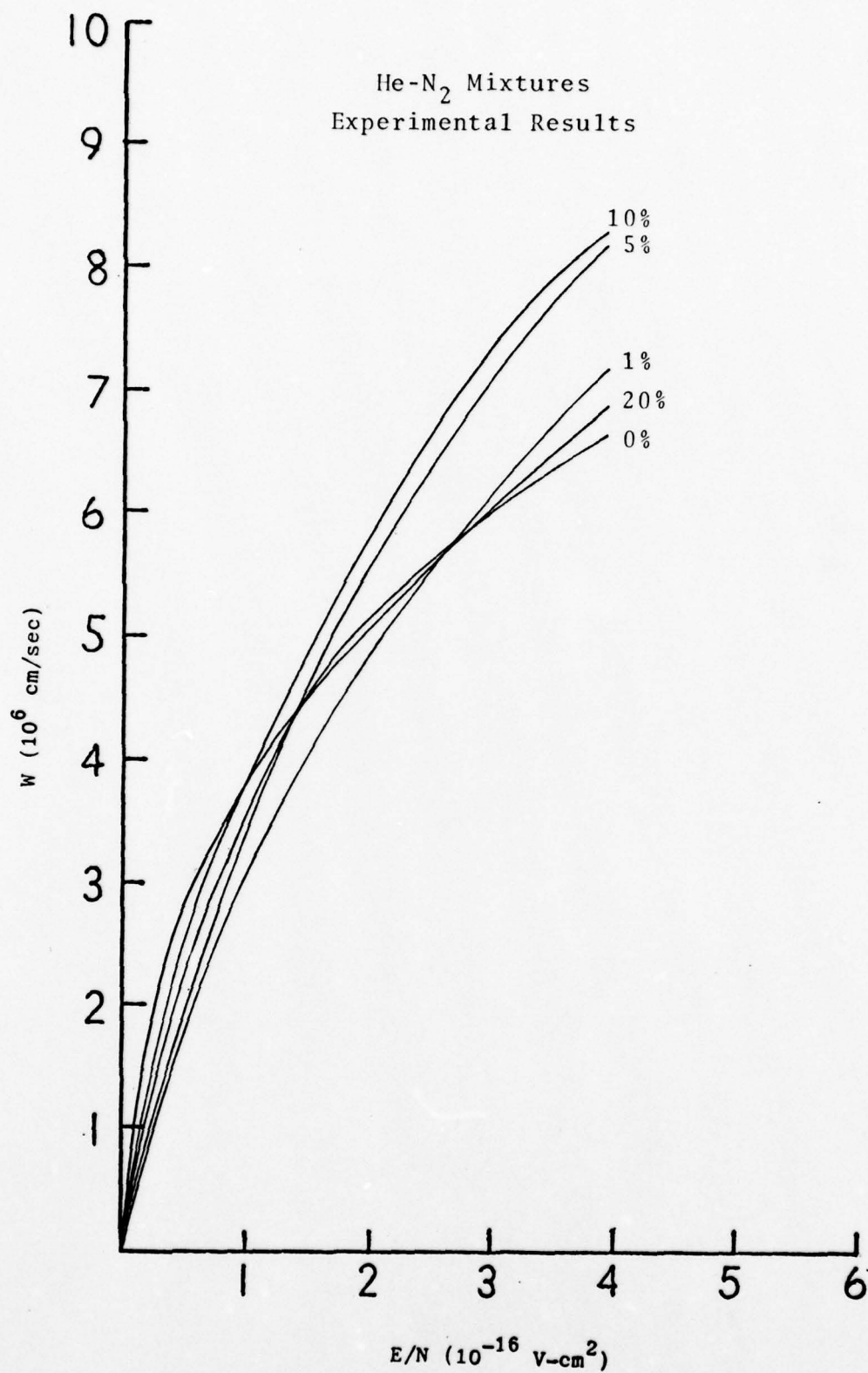


Figure 30. Experimental Results for Electron Drift Velocities in He with 0%, 1%, 5%, 10%, and 20% Added N<sub>2</sub>.



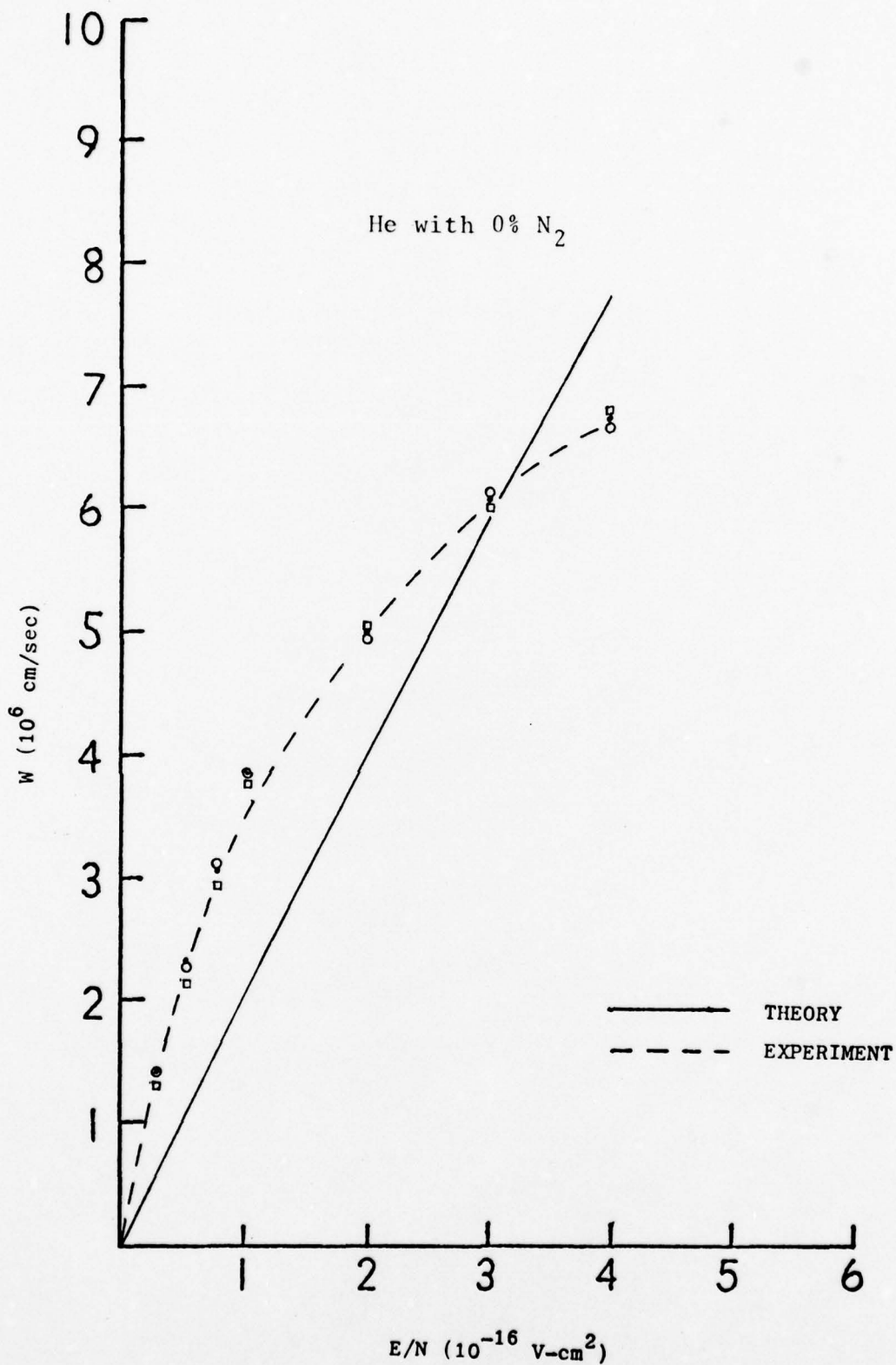


Figure 31. Electron Drift Velocity in He with 0% Added N<sub>2</sub>. Comparison of Theory with Experiment.

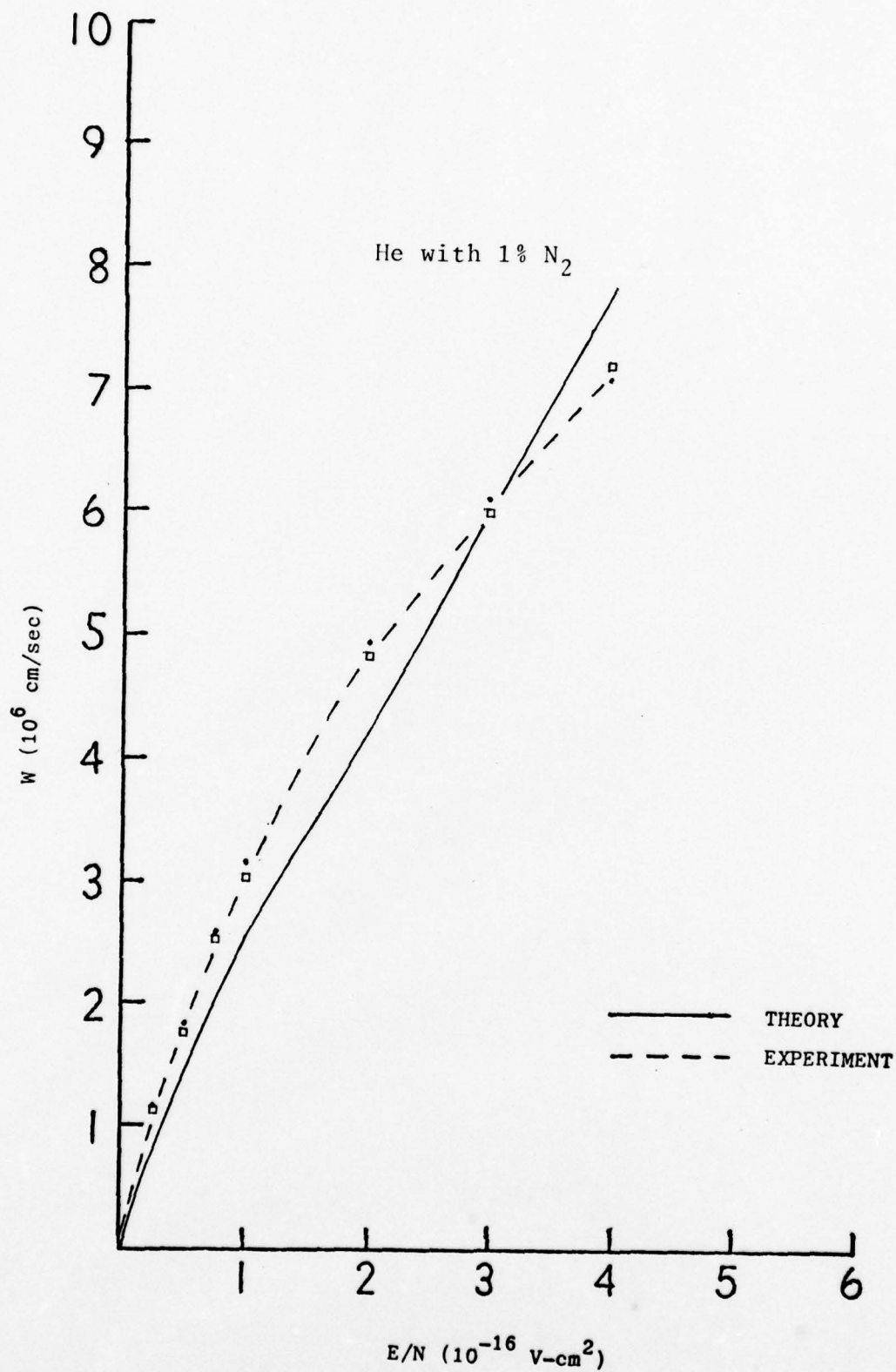


Figure 32. Electron Drift Velocity in He with 1% Added N<sub>2</sub>. Comparison of Theory with Experiment.

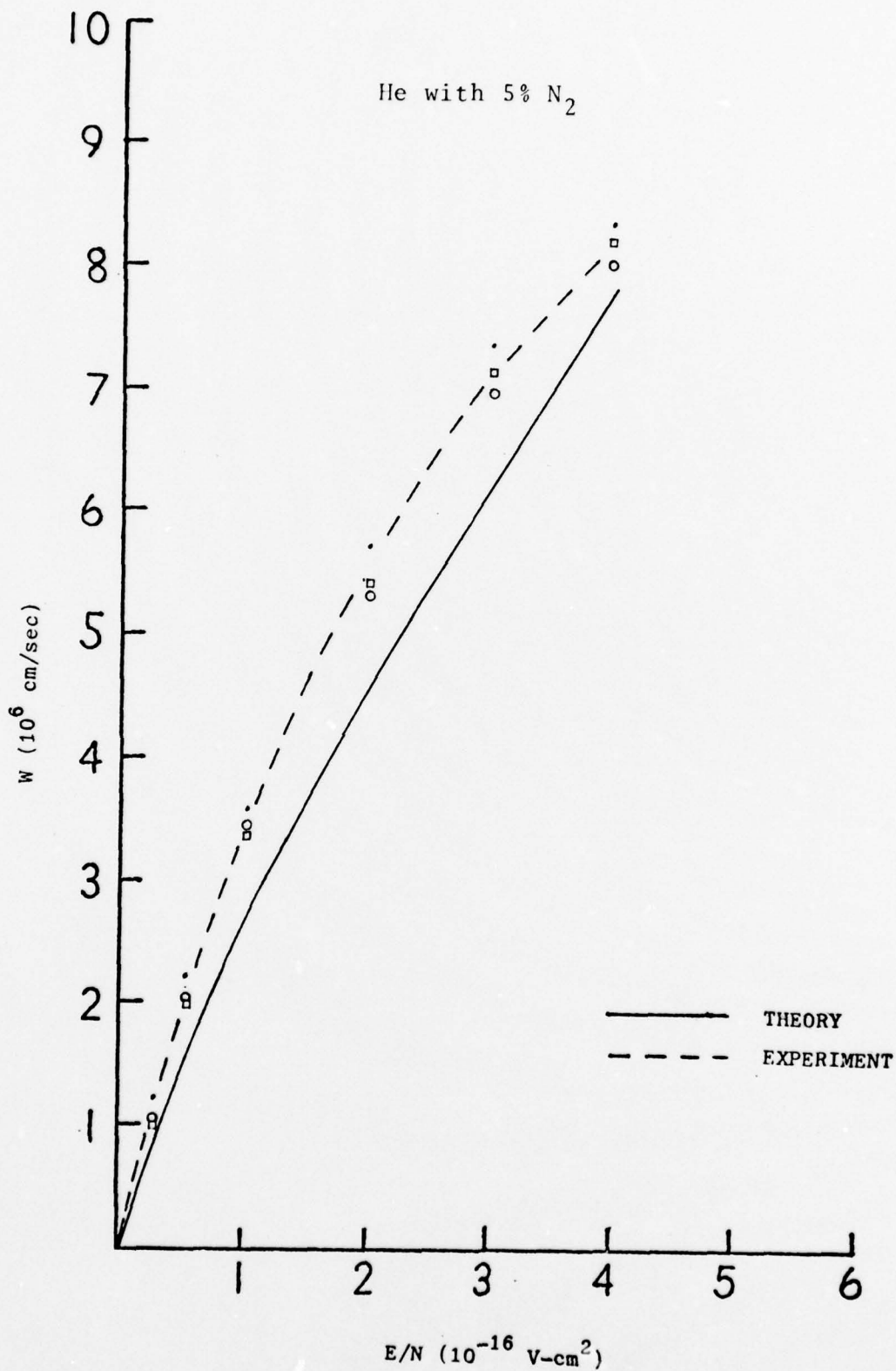


Figure 33. Electron Drift Velocity in He with 5% Added N<sub>2</sub>. Comparison of Theory with Experiment.

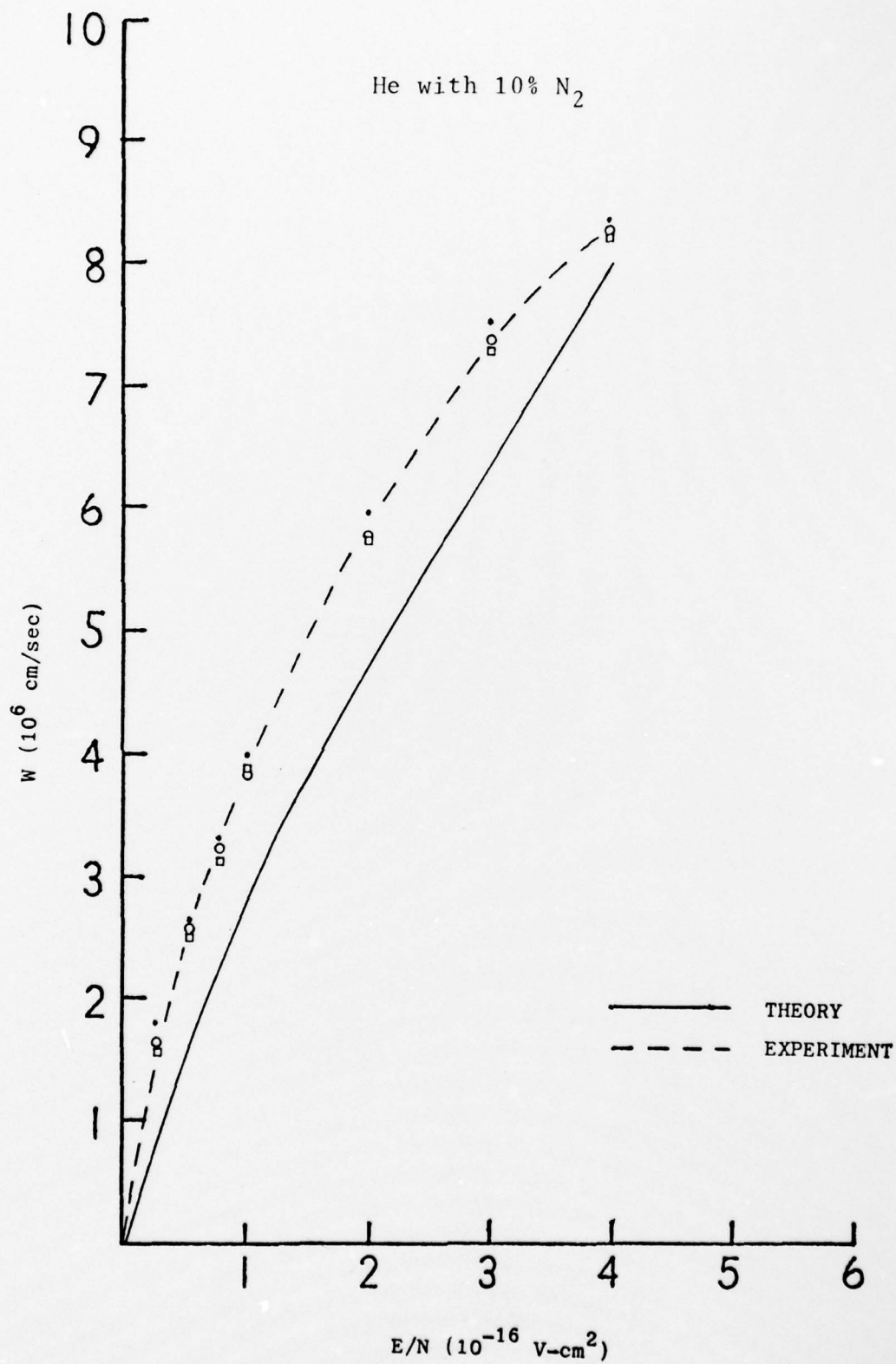


Figure 34. Electron Drift Velocity in He with 10% Added N<sub>2</sub>. Comparison of Theory with Experiment.



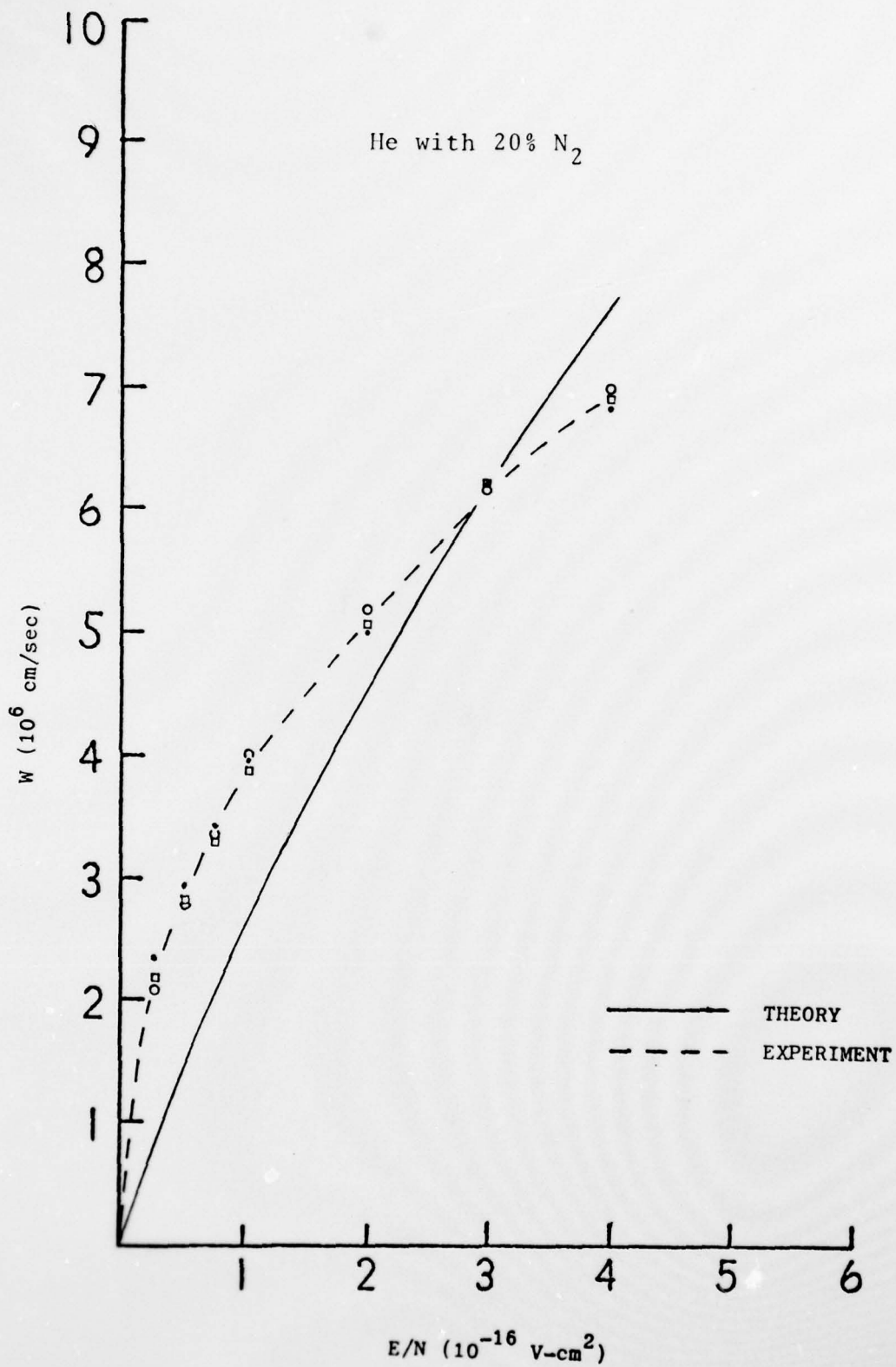


Figure 35. Electron Drift Velocities in He with 20% Added N<sub>2</sub>. Comparison of Theory with Experiment.

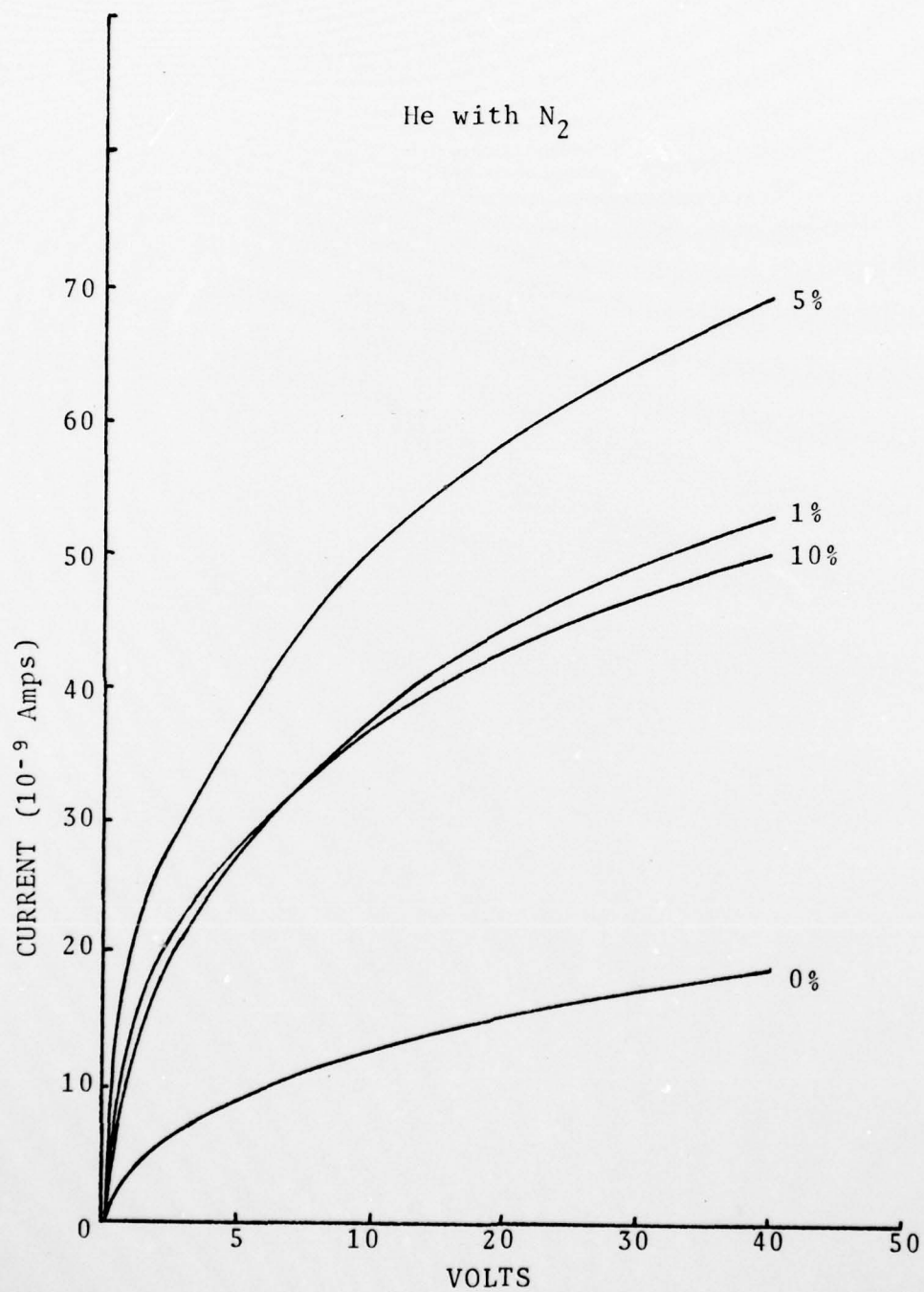
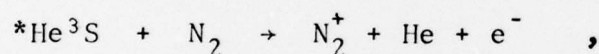


Figure 36. Current-Voltage Curves for He-N<sub>2</sub> Mixtures Where Helium Was the Gas Excited.

This metastable energy level is 19.8 eV, and the ionization threshold of  $N_2$  is 15.5 eV. When these metastables collide with the  $N_2$  molecules, energy is transferred to the nitrogen, creating a nitrogen ion and an electron. The cross section of  $^*He\ S$  is large ( $145 \times 10^{-16}$  cm<sup>2</sup> at 0° C, Ref 33), so that there is a high collision probability with  $N_2$ . The lifetime of the metastable is sufficient to exist until reaching the probe where  $N_2$  was added (Ref 16). Through Penning ionization (resonant energy transfer) between metastable helium and nitrogen, electrons were released from the nitrogen molecule. The equation for this reaction is



where the asterisk indicates the excited state. What was observed in Fig. 36 was not changes in drift velocity, but changes in electron density. Nitrogen does not have a metastable energy state in resonance with helium; therefore, the effect is not seen when  $N_2$  was excited by the microwaves and He added by the probe as was done later. Figures 30 through 35 represent true drift velocity curves.

## Concluding Remarks and Recommendations

Concluding Remarks. The electron drift velocity curves obtained by the flowing afterglow technique show good agreement with the effects predicted by theory. This suggests that experimental data obtained by other techniques, such as time-of-flight, can be applied to situations where there is an active plasma. It was suggested by Long et al. (Ref 1) that optimum power loading in gas discharge lasers can be obtained by a judicious choice of gas mixtures. In addition, an even more dramatic effect in power loading can occur if the gas being excited is capable of Penning ionization. The increase in electron density can significantly increase pumping efficiency in gas lasers if the primary pumping mechanism is by electron impact excitation.

Recommendations. The computer code used to generate the theoretical drift velocity curves should be updated with the latest electron impact cross sections to provide a better basis for experimental comparison. Inclusion of metastable cross sections would be valuable to predict the flowing afterglow. One might consider expanding the computer program to include a small fixed amount of impurity to test if this would have a masking effect on differential negative conductivity. For example, variable mixture ratios of Ar-CO with a fixed .5% of nitrogen.



If this experiment is repeated, care should be taken to ensure a high vacuum if argon, krypton, or xenon is used as the rare gas diluent. The system described in Chapter III used rubber vacuum hose to connect component parts. Welded stainless steel would provide a better vacuum base pressure.

In all, the effects on electron drift velocity predicted by theory when a molecular gas is added to a rare gas can be demonstrated in the flowing afterglow plasma when care is taken to account for effects due to impurities and variations in electron density.

## VI. Drift Tube Design

### Introduction

In past years, there have been many drift tubes designed and built, each succeeding tube usually having improvements on previous designs. For years drift tubes employed a "gauze" (electronic gate system) to determine the path length and time-of-flight of an electron swarm in a uniform electric field.<sup>1</sup> The "gauze" system created many problems in drift tube designs as the gauze adversely affected the uniformity of the electric field in the drift region. With the development of fast rise time particle multipliers, one can now measure the time-of-flight by direct-detection time delay. The "gauze" system can be eliminated and drift tubes much simplified.

This chapter proposes a drift tube design based on the time-of-flight principle and the photoelectric effect. The best aspects of previous drift tubes have been merged, along with the latest electronic devices. Where the design concepts of others have been used, the appropriate credit and reference is given.

---

<sup>1</sup>Ref 2 has several designs of this type along with the theory of operation. The reader is referred to this text for background information.

The concept of time-of-flight is discussed, followed by a detailed explanation concerning the design of the drift tube. Finally, a proposal for alignment of the guard ring structure is presented. A basic mechanical drawing and parts list is given in Appendix C.

#### Drift Tube Concept

To find the velocity of any non-relativistic particle, all that is needed is a distance of travel and the time it takes to traverse that distance. Mathematically, this is the familiar rate-time-distance equation,

$$W = d/t , \quad (28)$$

where the rate of travel is now the electron drift velocity,  $W$ . The problem now is to accurately determine the two parameters,  $d$  and  $t$ .

An ultraviolet laser is used to create an electron swarm at a photocathode by the photoelectric effect (Ref 9) as in Fig. 37. The electrons are then drawn toward the anode by a uniform DC electric field. The anode has an aperture at its center which allows the central axis electrons to pass on to the electron multiplier. The distance of travel is known by direct measurement. The time-of-flight is determined from when the UV laser pulse hits the photocathode to when it is detected by the electron

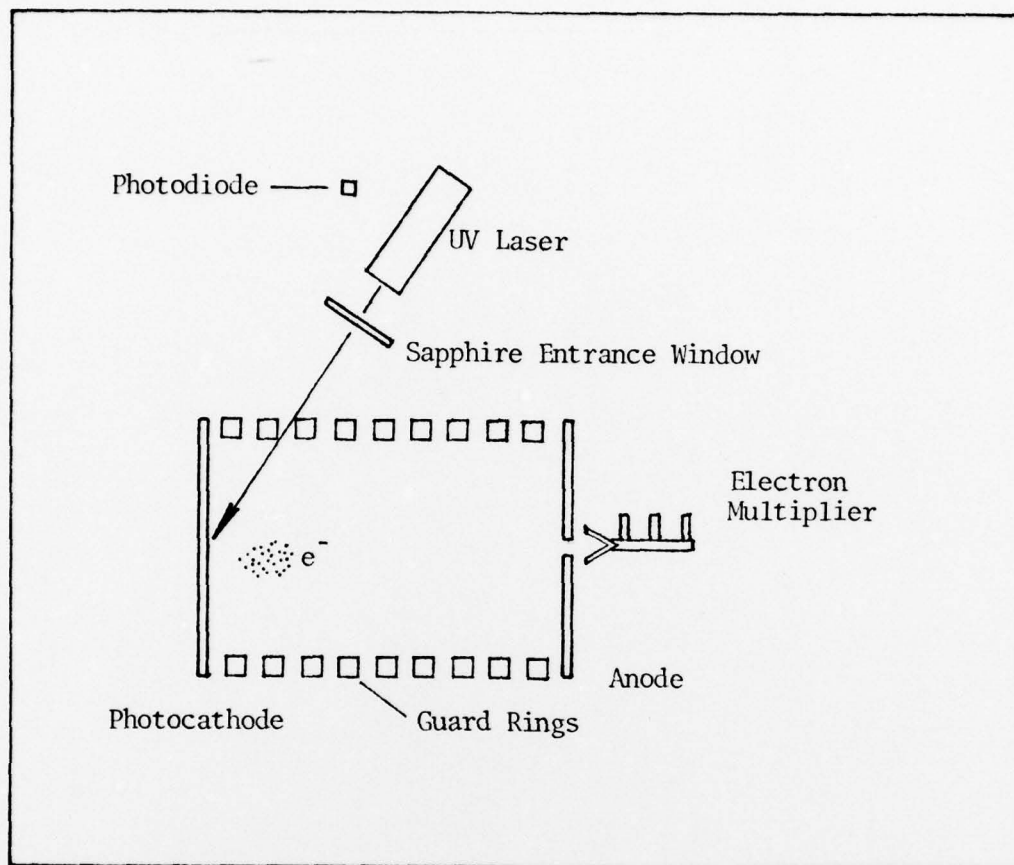


Figure 37. Light from a UV Laser Produces an Electron Swarm at a Photocathode. The UV Light is Detected by a Photodiode and the Electrons by an Electron Multiplier.

multiplier. A photodiode external to the drift tube determines when the electrons are released from the photocathode by detecting the UV light reflected from the entrance window. The output of the photodiode and the electron multiplier are fed into a time delay analyzer, and the output plotted on an X-Y recorder (see Fig. 38).



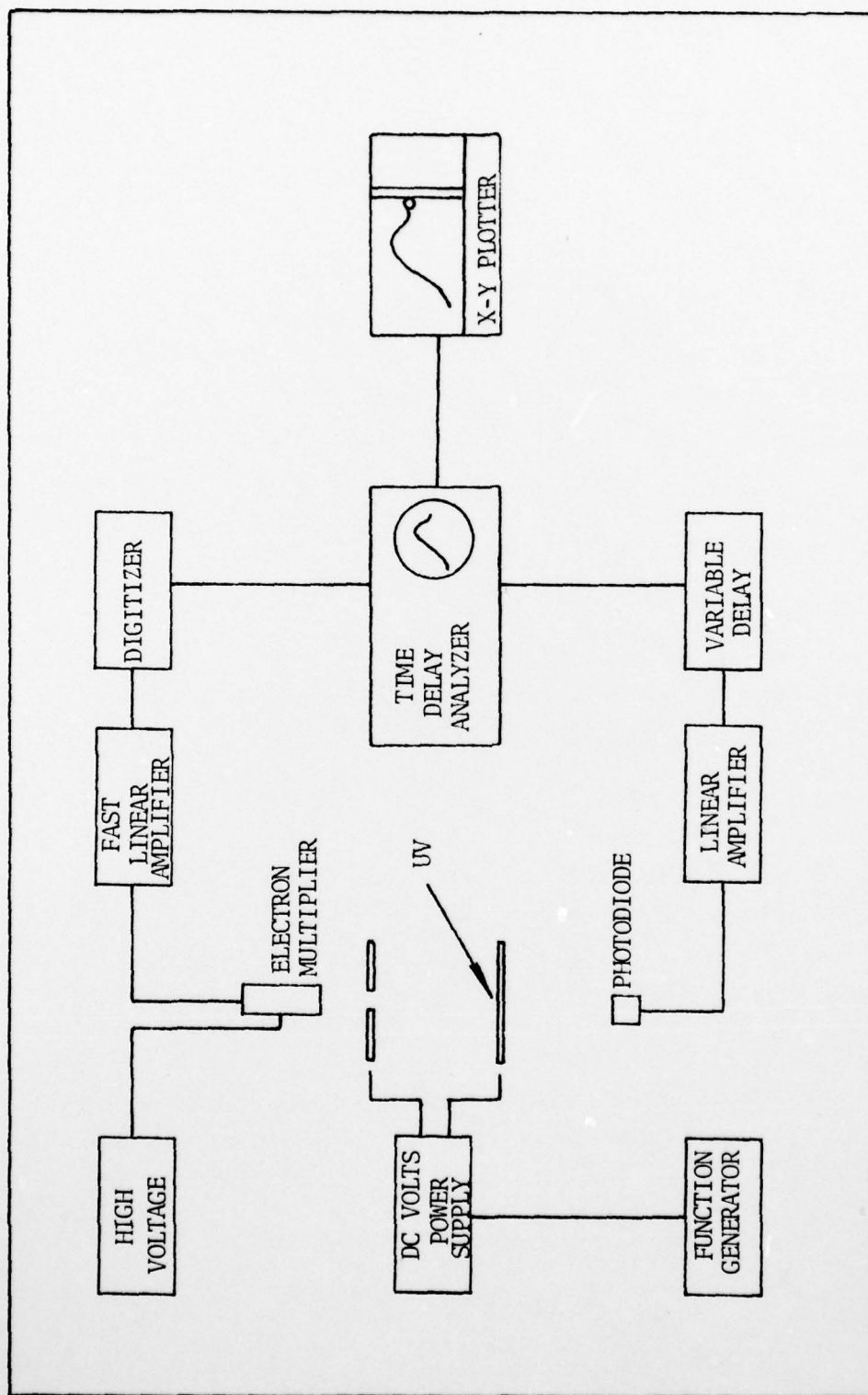


Figure 38. Drift Tube Diagnostics (Ref 2)

A function generator is used to vary the voltage between the anode and cathode to obtain a continuous sweep of E/N values. The variable delay is used to calibrate the system.

### Drift Tube Design

A simplified sketch of the drift tube is presented in Fig. 39 for reference. The tube was designed around standard parts and flanges so that production costs and complicated milling could be held to a minimum. The entire system is to be constructed to ultra-high vacuum standards to obtain a desired base pressure of  $10^{-9}$  torr. The design is presented in three parts: the drift region, detection system and electronics, and vacuum system. Each will be discussed in detail in the following sub-sections. Other parts not discussed are assumed to be self-evident.

Drift Region. The drift region consists of a photocathode, an anode, and the guard ring structure. The guard ring design is that of Crompton (Ref 4).

The photocathode is separated from the anode by 10 cm to provide a drift time for typical E/N values that is much greater than the pulse width of the laser used to create the electron swarm. For drift velocities of interest, approximately  $4 \times 10^6$  cm/sec, the electrons would take  $2.5 \times 10^{-6}$  sec to traverse the drift region. The laser suggested for use with this system (see Appendix C) has

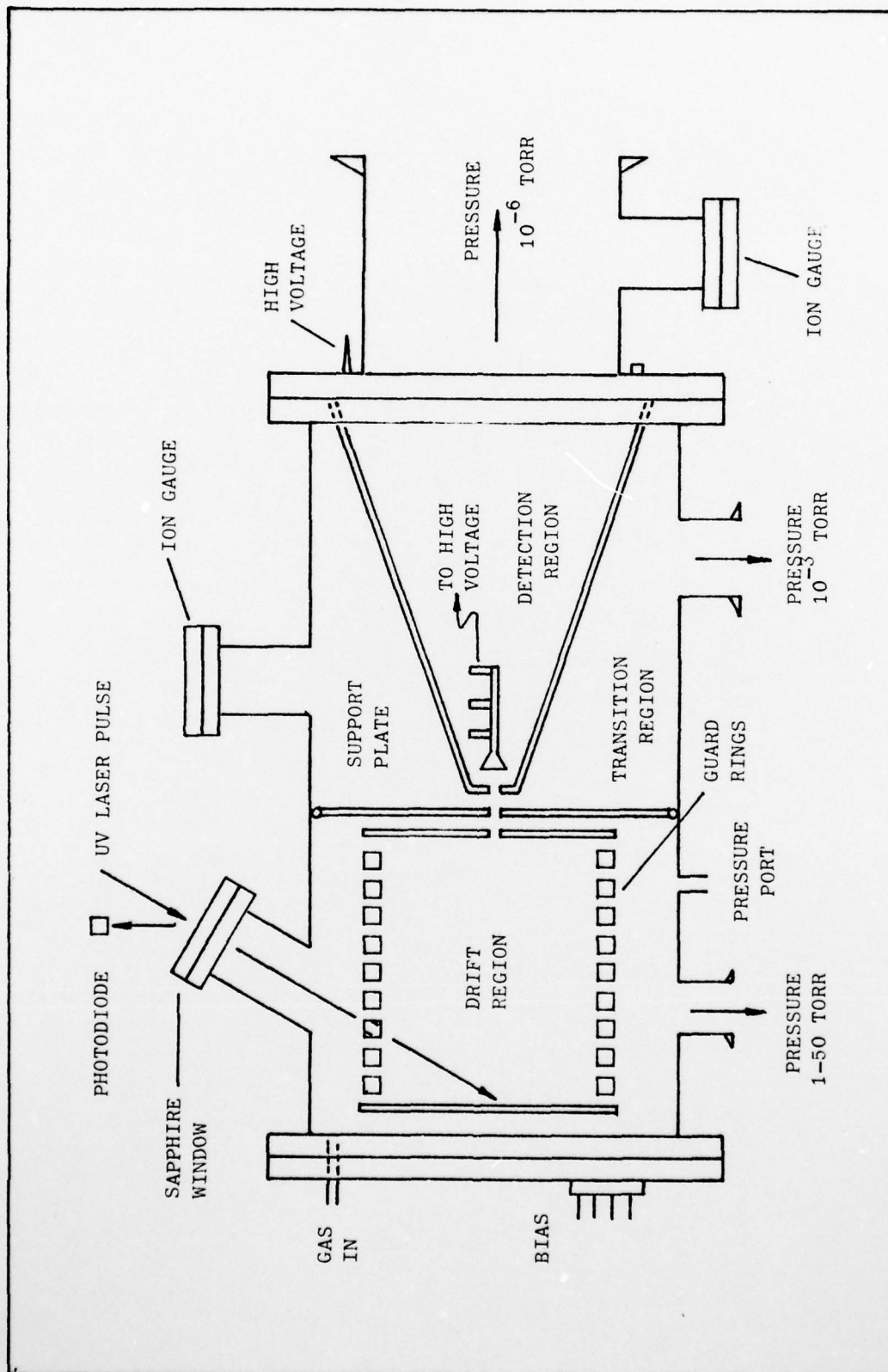


Fig. 39. Conceptual Sketch of drift tube.

a pulse width of  $1.4 \times 10^{-8}$  sec, or roughly 100 times shorter than the electron transient time. This is more than adequate to give good temporal resolution to the electron swarm.

The guard ring structure consists of nine thick copper electrodes of 8 cm inside diameter and 10 cm outside diameter and 1 cm thick. They are supported by four stainless steel rods tapped directly into the blank end flange. Electrical insulation from the guard rings is provided by alumina jackets. The guard rings are separated by .5 mm alumina spacers. A 4 mm aperture is drilled in one of the guard rings to allow the laser pulse to reach the photocathode.

There are four distinct advantages (Ref 4) to using thick guard rings as opposed to a thin ring structure. First, thick electrodes provide greater mechanical stability. Thin electrodes tend to warp under pressure and heat caused by periodic bake-outs. These warps severely affect the uniformity of the electric field in the drift region. Second, because very thin spacers are used between the thick electrodes (.5 mm), dielectric soakage is greatly reduced. Third, the thick electrodes shield the drift region more effectively from stray electric fields that might be produced by the chamber housing. Fourth, they provide a high degree of E-field uniformity on the axis of the drift region, as shown by the solution of Laplace's



equation for the thick electrodes (Ref 4). (The solution of the equation is presented in Appendix D.) The field becomes non-uniform close to the electrodes, but this is acceptable as only the center axis electrons, where the field is highly uniform, are to be measured.

The anode end of the guard ring structure is supported by a 4 mm thick stainless steel plate. A rubber gasket about its circumference provides a vacuum-tight seal and yet allows adjustment of the guard rings if necessary. There is a 1.2 mm aperture in the anode and a 2 mm aperture in the guard ring support to allow passage of the electrons to the electron multiplier. Glass encased resistors are used to establish the appropriate potentials on the guard rings.

Detection System and Electrical Wiring. The initial laser pulse is detected by a pin photodiode positioned as previously shown in Fig. 39. The EG&G pin photodiode has a rise time of 3 nsec, providing a start pulse which is  $10^3$  times faster than the electron swarm transient time. The stop pulse is triggered by a Channeltron electron multiplier having a 20 nsec response time and a gain of  $10^6$  when biased at 2 kV. Electrical feed throughs are positioned as shown in Appendix C to provide electrical power for the guard ring structure, electron multiplier, and ionization pressure gauges. Internal wires are non-insulated. Where necessary, ceramic jackets are used for insulation.

Vacuum System. The drift tube is divided into three regions connected only by small apertures (see Fig. 39), following the design of Wagner et al. (Ref 2). This arrangement allows pressures of 1-50 torr to be maintained in the drift region while pressures of  $10^{-6}$  torr can exist in the detection chamber to allow use of the electron multiplier as the detector. Ionization pressure gauges are used in the detection and transition region while a simple pressure port is employed in the drift region for use with an aneroid pressure gauge.

#### Proposed Alignment of the Electrodes

An "X" is scribed dead center on the inside of the blank end flange that supports the guard ring structure. Clamp the flange on a table "X" side up, with a "C" clamp and a block of wood. Vertically mount a 5 mW HeNe laser and reflect its beam back on itself directly over the "X" (see Fig. 40). This ensures the laser beam is perpendicular to the flange. Mount the four guard ring support posts securely on the flange. Add the appropriate spacers and photocathode. Adjust the photocathode to reflect the laser beam back on itself by slightly trimming the spacers. Assemble the guard rings and spacers. Put the anode in place and secure it with spacers and nuts as shown in Fig. 41. Tighten the nuts lightly. The anode should be adjusted to reflect the laser beam back on

AD-A080 178

AIR FORCE INST OF TECH WRIGHT-PATTERSON AFB OH SCH00--ETC F/G 20/9  
ANALYSIS OF ELECTRON DRIFT VELOCITIES IN MOLECULAR GAS-RARE GAS--ETC(U)  
DEC 79 R F WITTLER

UNCLASSIFIED

AFIT/0EP/PH/79D-13

NL

2 OF 2

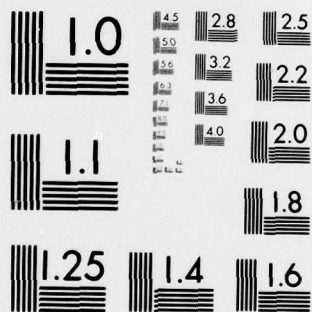
AD  
A080178



END  
DATE  
FILMED

3 - 80

DDC



MICROCOPY RESOLUTION TEST CHART  
NATIONAL BUREAU OF STANDARDS-1963-A



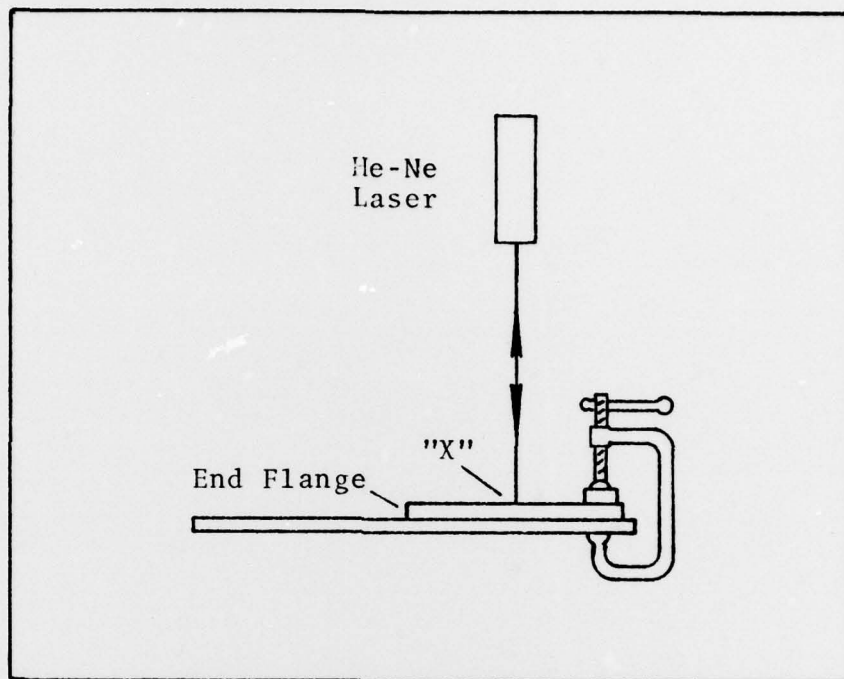


Figure 40. Alignment of Laser Over Center of End Flange.

itself by tightening the nuts or trimming the spacers if necessary. The nuts should all be tightened firmly. Place the support plate and spacers over the anode nuts and secure it in place with nuts. The laser beam should now be reflected from the cathode back through the anode and support plate aperture for perfect alignment.

#### Recommendations

This drift tube has not been constructed; it is only a proposal to simplify previous designs using the latest

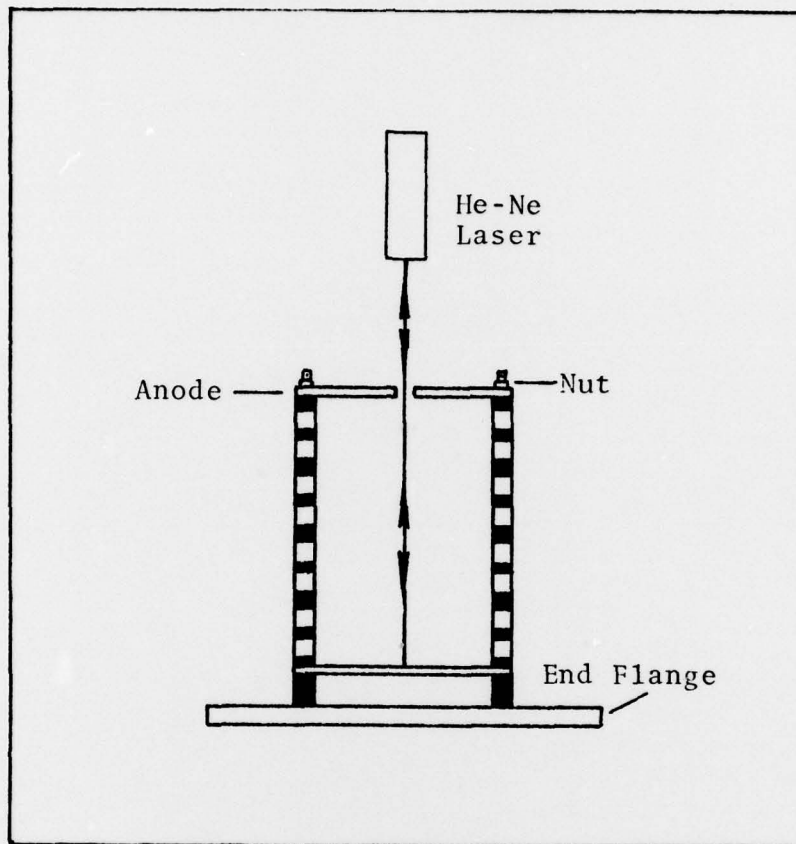


Figure 41. Alignment of Anode and Cathode

electronic devices and time-proven concepts. Any modification of this drift tube or improvements is encouraged prior to actual construction.

### Bibliography

1. W.H. Long, W.F. Bailey, A. Garscadden, Phys. Rev., 13: 471 (1976).
2. L.G.H. Huxley, R.W. Crompton, The Diffusion and Drift of Electrons in Gases, J. Wiley and Sons, New York, 1974.
3. R.W. Crompton, H.B. Milloy, Aust. J. Phys., 30: 51 (1977).
4. R.W. Crompton, M.T. Elford, J. Gascoigne, Aust. J. Phys., 18: 409 (1965).
5. T. Nagy, L. Nagy, S. Dési, Nuclear Instruments and Methods, 8: 327 (1960).
6. J.M. Kushner, D.S. Toffolo, J. of Appl. Phys., 23: 594 (1952).
7. H.B. Milloy, Aust. J. Phys., 30: 61 (1977).
8. J.L. Francey, D.A. Jones, Aust. J. Phys., 30: 302 (1977).
9. K.J. Nygaard, Office of Naval Research, TR-2-1-79, Jan 1979.
10. L.T. Specht, S.A. Lawton, T.A. DeTemple, Electron Ionization and Excitation Coefficients for Argon, Krypton and Xenon in Low E/N Regions.
11. M.R. Stamm, Air Force Institute of Technology, Private Communication.
12. L. Frommhold, Annal of Phys., 48: 408 (1968).
13. E.D. Klema, J.S. Allen, Phys. Rev., 77: 661 (1950).
14. A.G. Robertson, Aust. J. Phys., 30: 39 (1977)
15. E.W. McDaniel, Collision Phenomena in Ionized Gases, Wiley and Sons, New York, 1964.
16. A. Garscadden, Wright Aeronautical Laboratory, Private Communication.
17. A. vonEngel, Ionized Gases, (2d Ed.), Oxford University Press, 1965.

18. T. Holstein, Phys. Rev., 70: 367 (1946).
19. S.R. Seshadri, Fundamentals of Plasma Physics, Elsevier Press, 1973.
20. J.C. Bowe, Phys. Rev., 117: 1411 (1960)
21. J.W. Dettmer, "Discharge Processes in the Oxygen Plasma," Unpublished PhD Dissertation, Air Force Institute of Technology, Wright-Patterson AFB OH, 1978.
22. R.S. Harp, Office of Naval Research, Project 7073, Oct 1973.
23. F.F. Chen, Introduction to Plasma Physics, Plenum Press, New York, 1974.
24. S.C. Brown, Basic Data of Plasma Physics, MIT Press, Cambridge MA, 1967.
25. S.C. Brown, Introduction to Electrical Discharges in Gases, John Wiley and Sons, New York, 1966.
26. E. Kreyszig, Advanced Engineering Mathematics (3d Ed.), John Wiley and Sons, New York, 1972.
27. M.A. Heald, C.B. Whorton, Plasma Diagnostics with Microwaves, John Wiley and Sons, New York, 1965.
28. T.A. Moreno, Microwave Transmission Design Data, Dover Publications, Inc., New York, 1948.
29. G. Janzen, Aust. J. Phys., 29: 389 (1976).
30. M.L. Andrews, Private Communication.
31. J.E. Land, JILA Report, 1977.
32. M.J.R. Schwar, Electrical Probes for Plasma Diagnostics, American Elsevier, New York, 1970.
33. Ya.B. Zel'dovich, Yu.P. Raizer, Physics of Shock Waves and High-Temperature Hydrodynamic Phenomena, Vol. I, Academic Press, New York, 1966.

#### Additional References

- G.L. Broglia, V. Dallacasa, Phys. Rev. A, 18: 711 (1978).
- M.T. Elford, A.G. Robertson, Aust. J. Phys., 26: 685 (1973).
- E.B. Wagner, F.J. Davis, G.S. Hurst, J. Chem. Phys., 47: 3138 (1967).



## Appendix A

The resonant frequency of a microwave cavity can be altered by inserting a plasma in the cavity. The electron density of the plasma determines its permittivity which affects the resonant frequency (Ref 27). By measuring the change in resonant frequency from the discharge off condition to the discharge on conditions, the electron density can be determined.

The cavity used in this experiment was of cylindrical geometry. It could use either transmitted or reflected microwave power; however, only the transmitted power was measured in this case. The cavity dimensions are given in Fig. A-1 and the circuit diagnostics in Fig. A-2. The microwave power was supplied by an Alfred sweep generator capable of sweeping a frequency range of 2-4 GHz.

A 50  $\Omega$  isolator was used in series with the resonant cavity to prevent damage to the sweep generator. The wave meter was used to measure the resonant frequency of the microwave cavity. The oscilloscope provides a visual display of resonant peaks.

The resonant frequency of the cavity with the discharge off is obtained experimentally, with the cavity in place, so as to take account of the quartz flow tube. A "ball-park" frequency can be obtained by using the equation

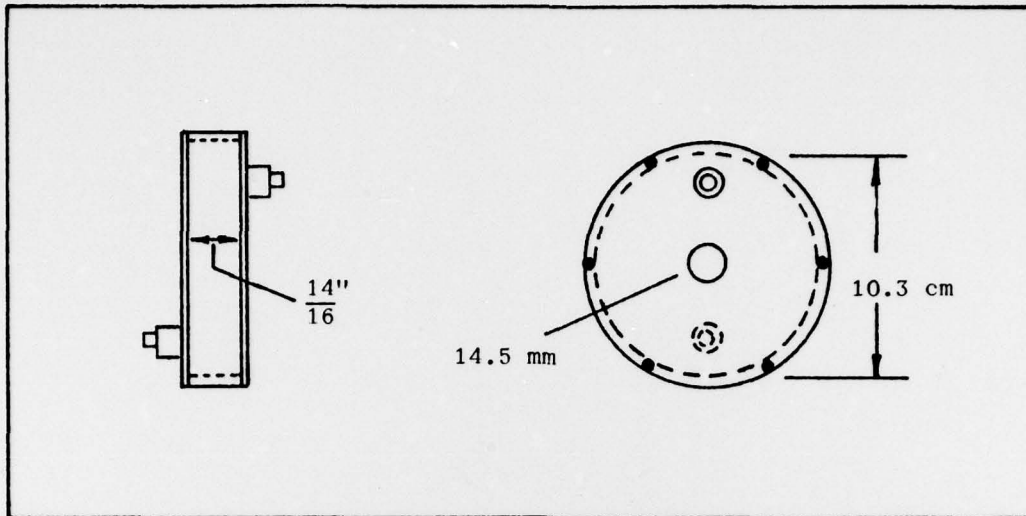


Figure A-1. Microwave Resonant Cavity

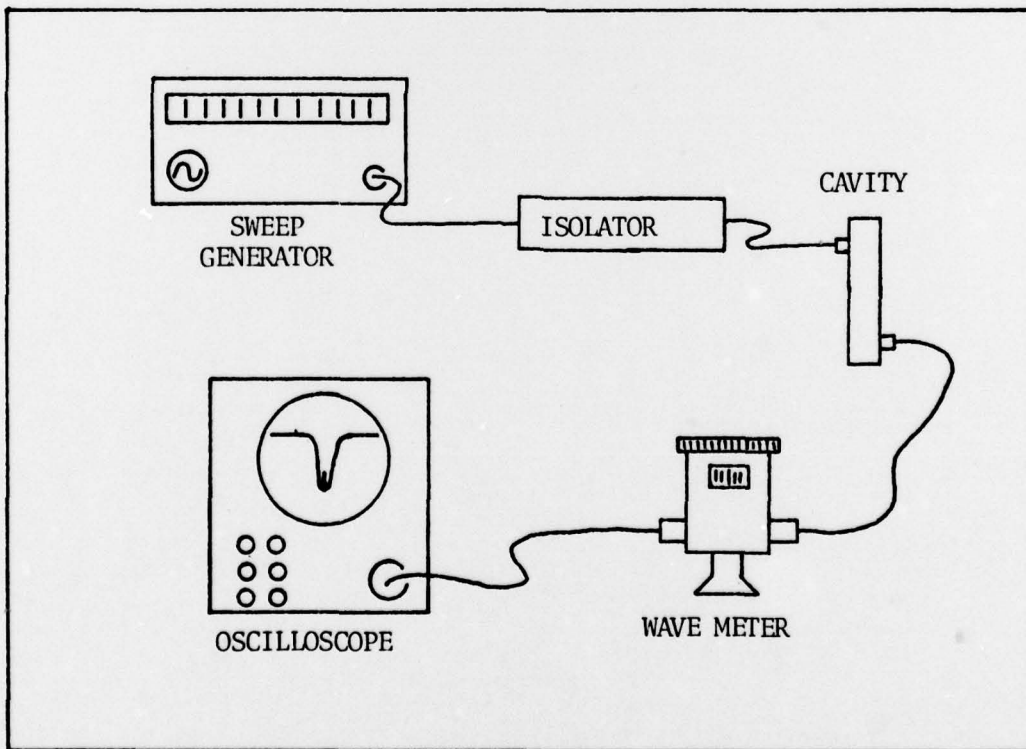


Figure A-2. Resonant Cavity Diagnostics

for the resonant wavelength of a cylindrical cavity in the  $TM_{lmn}$  mode (Ref 28)

$$\lambda_o = \frac{4}{\left\{ \left( \frac{l}{z_o} \right)^2 + \left( \frac{u_{m,n}}{\pi a} \right)^2 \right\}^{1/2}} \quad , \quad (A-1)$$

where

$$u_{mn} = n^{\text{th}} \text{ root of } J_o$$

$$a = \text{interior radius of the cavity} \quad ,$$

The cavity used was  $TM_{010}$ , therefore  $l = 0$  and Equation (A-1) reduces to

$$\lambda_o = \frac{2\pi a}{u_{mn}} \quad . \quad (A-2)$$

Values for  $u_{mn}$  can be found in Table 13-1 of Ref. 28.

When the sweep generator scans the frequency range, a prominent dip will appear on the oscilloscope corresponding to the resonant frequency of the cavity. A small peak will also appear corresponding to the resonant frequency of the wave meter. One simply adjusts the wave meter until the dip and peak coincide. The resonant frequency of the cavity and wave meter are then identical and can be read directly from the wave meter gauge.



When the plasma is created (discharge on condition), the resonant frequency of the cavity will shift. The wave meter is then readjusted to the new frequency. The resonant frequency shift can be related to the electron density by

$$\frac{\Delta f}{f_o} = - \frac{1}{2} \frac{\omega_{p_o}^2}{\omega^2 + \nu_m^2} \eta \quad , \quad (A-3)$$

where

- $f_o$  = unperturbed resonant frequency
- $\omega_{p_o}$  = unperturbed plasma frequency
- $\omega$  = perturbed resonant angular frequency
- $\nu_m$  = momentum transfer collision frequency
- $f'$  = perturbed resonant frequency.

The term  $\eta$  corresponds to a geometrical form factor and its value found in Ref. 29, page 11, for several TM modes. Making appropriate substitutions and rearranging results in an equation for the electron number density:

$$n_e = \frac{2(f_o - f')}{f_o} \frac{[(2\pi f')^2 + (\sigma_{mt} \langle \bar{v} \rangle n_a)^2]}{(2\pi \cdot 8973)^2 \eta} \quad . \quad (A-4)$$

It should be noted that frequency coupling of the microwave excitation cavity and resonant cavity is possible



if the excitation and resonant frequencies are close together (Ref 30). In this experiment, the frequencies were sufficiently separated so that no coupling was expected or observed.

## Appendix B

This appendix gives a list of equipment and electronic devices used in the experiment. The dimensions of the flow tube are given in Fig. B-1.

### Basic Equipment

Hastings flow meters, 100 and 500 SCCM  
D30A Leybold-Hereaus vacuum pump  
Systems Research Laboratories 2.45 GHz magnetron  
Microwave junction circulator  
Wallace-Tiernan pressure guage  
Variac voltage supply  
NRC thermocouple pressure gauge

### Diagnostics

H-P 410C Voltmeter  
H-P 6824A DC power supply  
H-P 425A Micro Volt-ammeter  
H-P 7004B X-Y Recorder

### Resonant Cavity

Alfred 650 sweep oscillator  
Sperry 50  $\Omega$  isolator  
Tektronix 547 oscilloscope  
General Microwave N604 wave meter

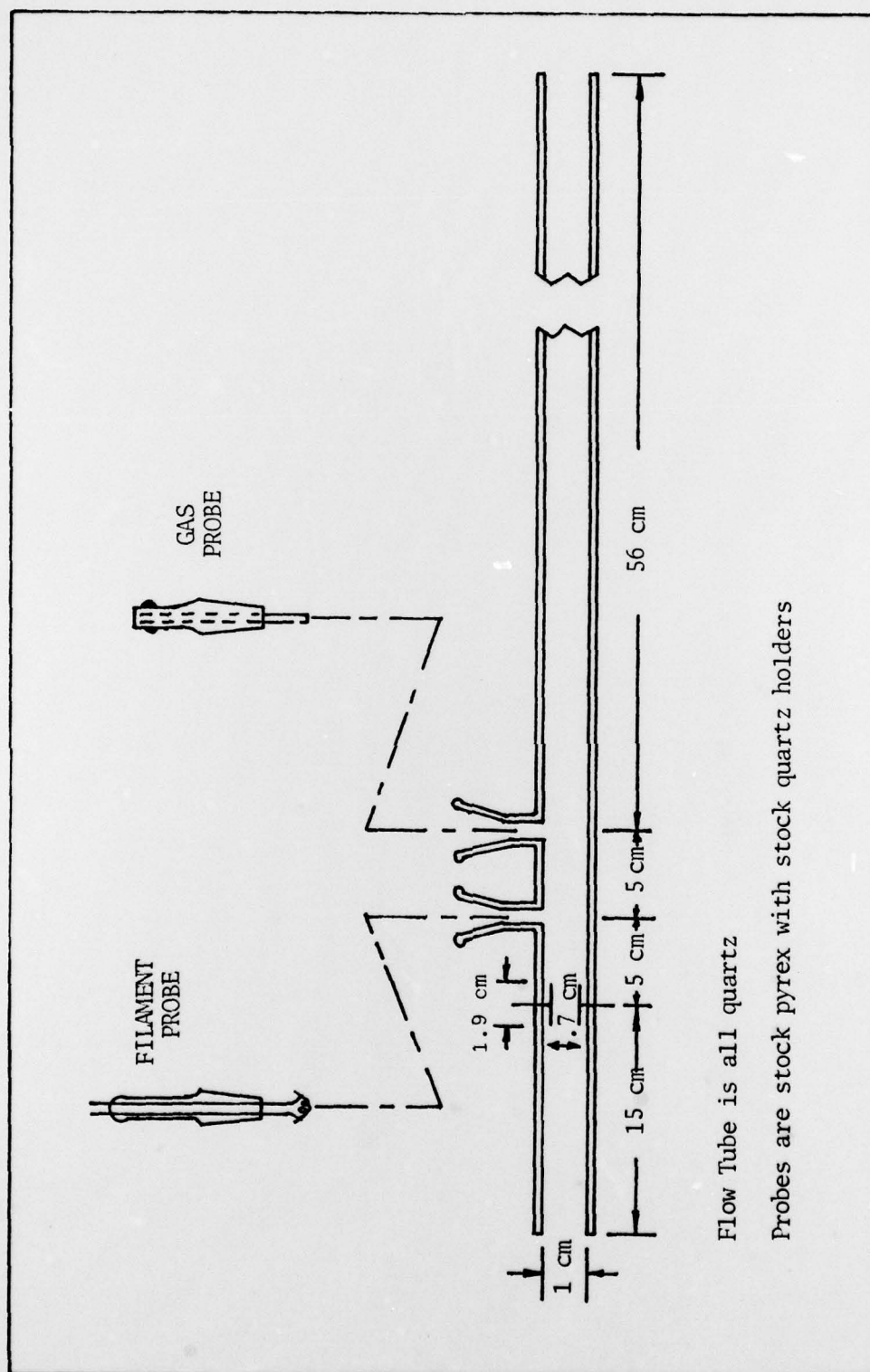
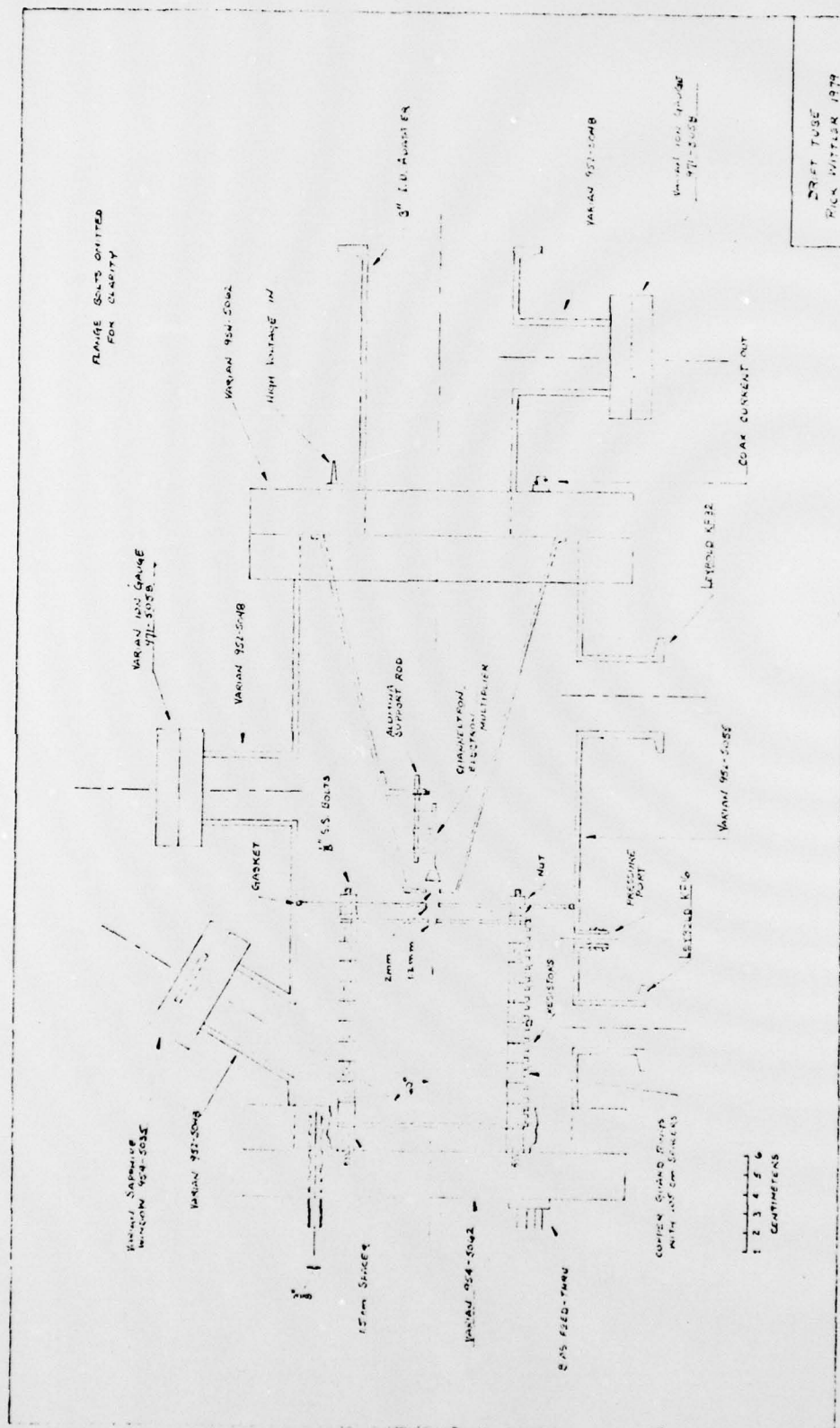


Figure B-1. Flow Tube Dimensions





## Appendix D

The solution to the Laplace equation for thick guard rings is presented in brief to show that the field near the axis is highly uniform. The geometry is shown in Fig. D-1.

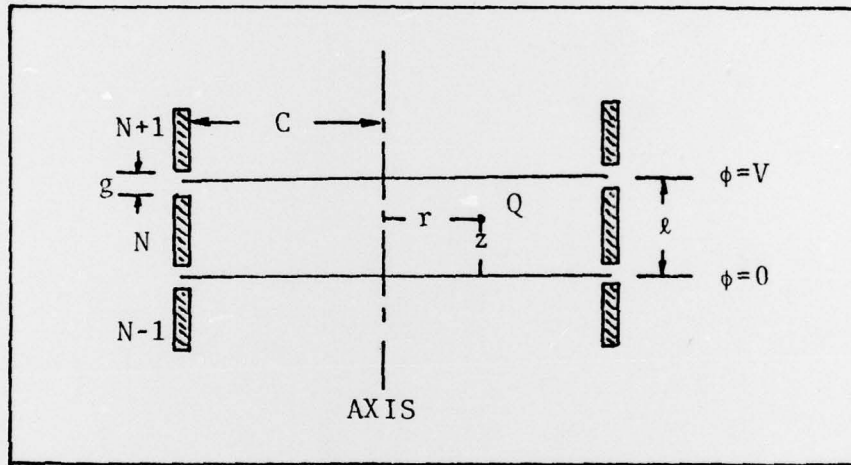


Figure D-1. Guard Ring Geometry  
for Drift Region (Ref 4).

The solution for the above geometry was obtained by Crompton (Ref 4);

$$\phi = \frac{Vz}{l} + \sum_N \frac{2V}{N\pi} \frac{I_0(N\pi r/l)}{I_0(N\pi C/l)} \sin(N\pi z/l) \frac{\sin(N\pi g/2l)}{N\pi g/l} \quad (D-1)$$

where

$g$  = gap between the electrodes

$r$  = radial distance from the axis

$\phi$  = potential at point  $Q$

$I_0$  = modified Bessel function of order zero

$N$  = summation index for all even  $N$  .

For the guard ring structure described in Chapter V,  
 $c = 4$  cm ,  $\ell = 1.05$  cm , Equation (D-1) shows the  
potential at a point 2.0 cm from the axis agrees with the  
potential of a uniform field within .035%.

## Appendix E

This appendix presents an analysis of errors for the experimental portion of this paper.

The equation for calculation of the electron drift velocity is

$$W = \frac{i}{e n_e A} \cdot$$

The values of  $e$  and  $A$  are constant throughout the experiment. A constant error in determining the area,  $A$ , of the electrodes was  $\pm 5\%$ . The value of  $n_e$  was held constant for each mixture ratio, and was determined accurate to within 15% because of the method used to calculate  $n_e$ . Also, it was impossible to detect slight changes in electron density once a run was started. The current,  $i$ , was taken directly from the X-Y recorder and, considering roundoff error, was accurate to  $\pm 4\%$ .

Flow meter readings were used to calculate the gas mixture ratio. The meters were  $\pm 2\%$  accurate for the pressure ranges considered. They could be read to  $\pm .15$  SCCM. This gives a possible  $\pm 40\%$  error for the 1% mixture ratio to  $\pm 5\%$  error for the 20% mixture ratio.

Random errors were limited to a certain extent by taking numerous runs at each mixture ratio to obtain a statistical average of data.

Systematic errors in calculating  $n_e$  arise from additional electron losses in the flow tube after the gas probe and filament ports were installed. This was accounted for, in part, by mathematical calculation of diffusion losses due to smaller diffusion lengths. This was compared to electron density curves before and after the ports were installed and agreed with calculated losses to within 11%.



## Appendix F

This appendix gives a sample calculation used to determine the electron number density between the measuring electrodes. The basic formula used is that found in Chapter IV in the alternate method section; i.e.,

$$n_{e_f} = \frac{(n_{e_o})(i_f)}{i_o}, \quad (F-1)$$

where the terms were defined in that section. An additional diffusion loss mechanism due to the smaller diffusion lengths around the two probes that were added had to be considered.

As an example, consider the electron loss curves for argon. The electron loss curves before and after the probes were installed are shown as curves A and B, respectively, in Fig. F-1. There is a transition from curve A to curve B (due to the probes) represented by curve C in Fig. F-1. The adjustment factor needed in the calculation for  $n_{e_f}$  to account for the loss is just the ratio of the final currents before and after the probes were installed;

$$\frac{i_{\text{after}}}{i_{\text{before}}} = .31$$

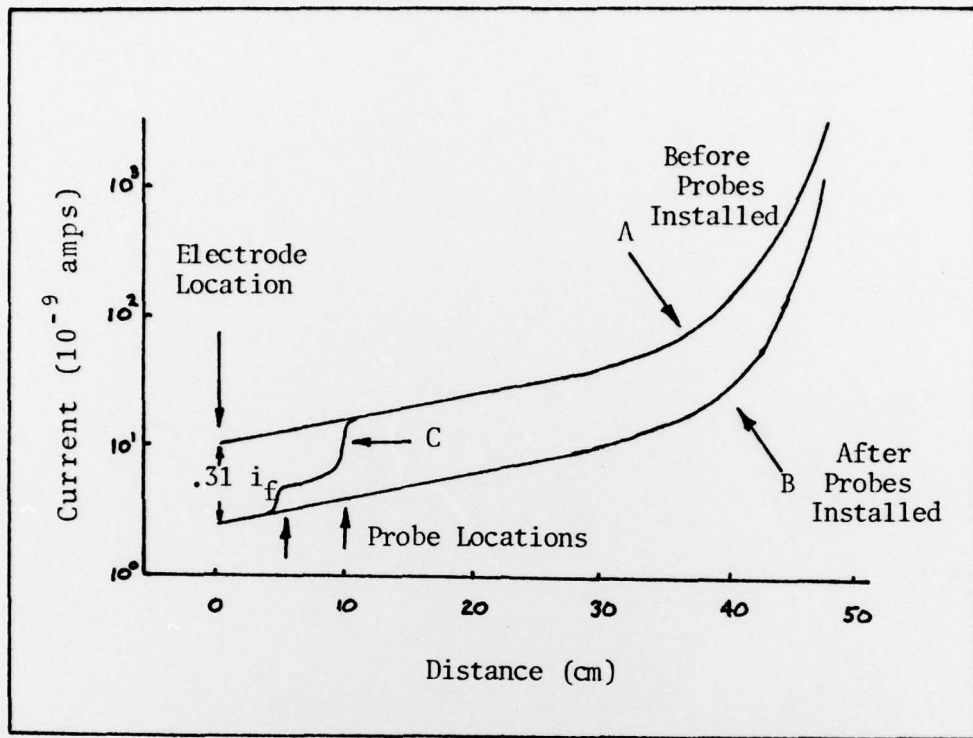


Figure F-1. Electron Loss Curves for Argon.

Equation (F-1) becomes

$$n_{e_f} = \frac{(n_{e_o})(i_f)(.31)}{i_o}$$

For

$$\begin{aligned} n_{e_o} &= 2.3 \times 10^7 \text{ cm}^{-3} \\ i_o &= 750 \times 10^{-9} \text{ amperes} \\ i_f &= 6.5 \times 10^{-9} \text{ amperes,} \\ n_{e_f} &= 6.18 \times 10^4 \text{ cm}^{-3} \end{aligned}$$

This value was substituted in the equation

$$W = \frac{i}{e n_e A} ,$$

that was used to generate the experimental drift velocity curves. For example, for a measured current between the electrodes of  $i = 37.7 \times 10^{-9}$  amps and

$$e = 1.602 \times 10^{-19} \text{ Coulombs}$$

$$A = 1.9 \text{ cm}^2 ,$$

the drift velocity is

$$W = 2 \times 10^6 \text{ cm/sec} .$$

### Vita

Richard F. Wittler was born on 5 September 1949 in New York City, New York. He is the son of Mr. and Mrs. George H. Wittler, Jr. of East Patchogue, New York. In June of 1967 he graduated from Bellport Senior High School, Brookhaven, New York and then received a B.A. degree in physics from Otterbein College, Westerville, Ohio in 1971. He was commissioned through the ROTC program and subsequently entered pilot training in 1971. He served the Air Force as a B-52 Aircraft Commander in the 441st Bombardment Squadron, Mather Air Force Base, California until entering the Air Force Institute of Technology in June of 1978.

Permanent Address: 16 Colonial Drive  
East Patchogue, New York 11772



| REPORT DOCUMENTATION PAGE  |                       | READ INSTRUCTIONS<br>BEFORE COMPLETING FORM                    |
|--|-----------------------|--|
| 1. REPORT NUMBER<br>AFIT/GEP/PH/79D-13   | 2. GOVT ACCESSION NO. | 3. RECIPIENT'S CATALOG NUMBER                                  |
| 4. TITLE (and Subtitle)<br>ANALYSIS OF ELECTRON DRIFT VELOCITIES IN<br>MOLECULAR GAS-RARE GAS MIXTURES USING A<br>FLOWING AFTERGLOW PLASMA   |                       | 5. TYPE OF REPORT & PERIOD COVERED<br>M.S. Thesis              |
| 7. AUTHOR(s)<br>Richard F. Wittler<br>Capt USAF  |                       | 6. PERFORMING ORG. REPORT NUMBER                               |
| 9. PERFORMING ORGANIZATION NAME AND ADDRESS<br>Air Force Institute of Technology (AFIT-EN)<br>Wright-Patterson Air Force Base OH   |                       | 8. CONTRACT OR GRANT NUMBER(s)                                 |
| 11. CONTROLLING OFFICE NAME AND ADDRESS<br>Air Force Aero Propulsion Laboratory<br>Wright-Patterson Air Force Base OH  |                       | 10. PROGRAM ELEMENT, PROJECT, TASK<br>AREA & WORK UNIT NUMBERS |
| 14. MONITORING AGENCY NAME & ADDRESS (if different from Controlling Office)  |                       | 12. REPORT DATE<br>December 1979                               |
|  |                       | 13. NUMBER OF PAGES<br>115                                     |
|  |                       | 15. SECURITY CLASS. (of this report)<br><br>UNCLASSIFIED       |
|  |                       | 15a. DECLASSIFICATION/DOWNGRADING<br>SCHEDULE                  |
| 16. DISTRIBUTION STATEMENT (of this Report)<br><br>Approved for Public Release; Distribution Unlimited.  |                       |  |
| 17. DISTRIBUTION STATEMENT (of the abstract entered in Block 20, if different from Report)   |                       |  |
| 18. SUPPLEMENTARY NOTES<br>Approved for Public Release; IAW AFR 190-17<br><br>JOSEPH P. HIPPS, Major, USAF<br>Director of Public Affairs   |                       |  |
| 19. KEY WORDS (Continue on reverse side if necessary and identify by block number)<br>Electron Drift Velocity      Argon<br>Rare Gas Mixtures      Helium<br>Flowing Afterglow      Plasma<br>Nitrogen   |                       |  |
| 20. ABSTRACT (Continue on reverse side if necessary and identify by block number)<br>Electron drift velocities are obtained in mixtures of Ar-N <sub>2</sub> , Ar-CO, and He-N <sub>2</sub> using a flowing afterglow. Theoretical development of drift velocities in the molecular gas-rare gas mixture is discussed. Two factors are discussed which determine the electron collision frequency; (1) the shape and magnitude of the electron elastic cross section of the buffer gas, and (2) the threshold energy and magnitude of the inelastic processes. Drift velocity enhancement and differential negative conductivity caused by the presence of small amounts<br>(Continued on Reverse) |                       |  |

UNCLASSIFIED

SECURITY CLASSIFICATION OF THIS PAGE(When Data Entered)

Item 20 (Continued):

of molecular gas are discussed. Experimental drift velocity curves show good agreement with theoretical curves obtained by a numerical solution to the Boltzmann equation. Minor deviations indicate that metastable ionization should be included in the computer analog to better model electron density in the flowing afterglow. A drift tube design using up-to-date electronics is proposed.

UNCLASSIFIED

SECURITY CLASSIFICATION OF THIS PAGE(When Data Entered)